HARVARD UNIVERSITY
Graduate School of Arts and Sciences

DISSERTATION ACCEPTANCE CERTIFICATE

The undersigned, appointed by the

School of Engineering and Applied Sciences

have examined a dissertation entitled

"Chemical Vapor Deposition of Cobalt-based Thin Films for Microelectronics"

presented by : Jing Yang

candidate for the degree of Doctor of Philosophy and here by certify that it is worthy of acceptance.

Signature _____

Typed name: Prof. R. Gordon

Signature _____

Typed name: Prof. F. Spaepen

Signature _____

Typed name: Prof. M. Aziz

Signature _____

Typed name: Prof. T. Betley

Date: December 16, 2013

Chemical Vapor Deposition of Cobalt-based Thin Films for Microelectronics

A dissertation presented

by

Jing Yang

to

The School of Engineering and Applied Sciences

in partial fulfillment of the requirements

for the degree of

Doctor of Philosophy

in the subject of

Applied Physics

Harvard University

Cambridge, Massachusetts

December, 2013

Dissertation Adviser
Professor Roy G. Gordon

Author
Jing Yang

Chemical Vapor Deposition of Cobalt-based Thin Films for Microelectronics

Abstract

In microelectronics, the device size continues to shrink to improve the performance and functionality, which sets technical challenges for the integrated circuit (IC) fabrication. Novel materials and processing techniques are developed to maintain excellent device performances and structural reliability. Cobalt-based thin films possess numerous applications in microelectronics with the potential to enhance the device performance and reliability. This thesis explores the fabrication, characterization and application of cobalt-based thin films for microelectronics. Chemical vapor deposition (CVD) technique has been applied for depositing cobalt-based thin films, because CVD can produce high quality thin films with excellent conformality in complex 3D architectures required for future microelectronics.

Cobalt nitride (Co_xN) is a promising candidate for adhesion-enhancing layer for advanced copper interconnects. Chapter 2 investigated the CVD process conditions for preparing face-centered-cubic (fcc) cobalt nitride films. The as-deposited Co_xN films demonstrated significant improvements in adhesion between the copper and the diffusion barrier.

Cobalt disilicide ($CoSi_2$) is considered as an attractive contact material for source, drain and gate electrodes in transistors. The fabrication of $CoSi_2$ from CVD Co_xN films is discussed in Chapter 3. The formation of smooth, conformal $CoSi_2$ without facets or voids is critical for microelectronic device reliability. A novel approach of backside sample preparation was developed for quantitatively evaluation of the $CoSi_2$/Si interfacial roughness. This method offers analytical support for advanced fabrication process development.

Chapter 4 highlights direct-liquid-evaporation (DLE) CVD of Co, Co_xN films. This DLE process avoids creating unwanted particles that are made when droplets from a nebulizer evaporate in a conventional direct liquid (DLI) process. DLE-CVD proves to be a high-throughput process for high-quality Co, Co_xN films with excellent step coverage.

Chapter 5 proves atom probe microscopy (APM) as an effective method for understanding the atomic-scale microstructure and compositional properties in thin films. 3D compositional information of DLE-CVD Co_xN thin films has been investigated using APM. The characterization using APM provides a unique tool that can be applied both to the design of nanostructured microelectronic applications and to the further understanding of the fundamental physical properties on which their operation relies.

Table of Contents

Acknowledgments

I would like to express my sincere gratitude to the countless people who are an indispensable part of my PhD life for making this challenging job enjoyable.

I first and foremost would like to thank my advisor Professor Roy G. Gordon for his support and guidance throughout my graduate career. Roy is not only a great scientist with broad knowledge in chemistry, but also a great mentor with patience and self-discipline. His words of "There are no failed experiments. You will only fail if you fail to learn." encouraged me to keep calm and carry on through the toughest times during my graduate school. I am deeply grateful for his generous contributions of time, ideas and funding that make my research productive and stimulating. In particular, I greatly appreciate that Roy offered his time to discuss recent research articles weekly besides the weekly group meetings. As the main contributor of the weekly journal club, I always felt inspired from Roy's insights in different research areas. Moreover, I felt fortunate to work with Roy and appreciate the industrial collaboration opportunities he provided. I learnt a lot from the visit to Applied Materials headquarter with Roy after the MRS spring 2012. Roy has motivated me to grow and become the best of myself.

I would also like to thank the other members of my thesis committee, Professor Michael J. Aziz, Professor Frans Spaepen and Professor Theodore Betley. Mike has guided me from the beginning to the end of my PhD career. I was fortunate to start my first research project in grad school with Mike in 2008 fall. And it is in Mike's class – ES 231 Energy Technology, where I first met my future supervisor, Dr. Robert L. Kleinberg from Schlumberger Doll Research (SDR) center. I am grateful to have Mike witnessed my growth over the past five years and half. Thanks Mike for serving both on my qualifying committee and thesis committee, and leading the graduate consortium on energy and environment which inspired me to pursue my passion in the energy sector. Frans is a great teacher. His course "Solids: Structure and Defects" helped me build a solid foundation for my graduate research. I am also thankful for his student - Professor Li-Chyong Chen for the outstanding example she has provided as a successful woman material scientist. I want to thank Ted for his willingness to serve on my thesis committee without any hesitation.

Besides my thesis committee, I need to extend my gratitude and thank many other great mentors who supported me along the way. Thank Professor Shriram Ramanathan and Professor David R. Clarke for serving on my qualifying committee. I am grateful for my undergrad advisor, Professor Shangjr Gwo from National Tsing-Hua University, who played an important role on my choice of grad schools. He always had faith in me and cheered me up when I was at my lowest point. I feel lucky to know such a caring advisor, and blessed for the long-lasting friendship and mentorship. I also want to thank Professor Pengfei Zhang from University of Science and Technology of China (USTC) and Professor Xi Yin, my college – USTC alumni, a genius string theorist and a passionate marathon runner, for being great friends.

I am indebted to my colleagues from Gordon Group. The members of the Gordon group have contributed immensely to my personal and professional life at Harvard. I enjoyed my days in Gordon group and I had great fun working with them. I deeply treasure the great friendship built over the years and believe some will last lifelong. I would like to first acknowledge Dr. Yeung (Billy) Au for introducing me to the Gordon group. I owe a big thanks to him for the insightful discussions in the lab and the joyful escapes away from lab. I also want to thank my mentor, Dr. Harish Bhandari, for teaching me the basics of CVD reactor design and construction, and working with me closely on my first project on CVD cobalt nitride. And I am grateful for many people who I worked with and shared ups and downs together: Leizhi Sun, my great deskmate, Kecheng Li, Dr. Xinwei Wang, Dr. Zhefeng Li, Dr. Yiqun Liu, Xiabing Lou, Danny Chua, Jun Feng, Chuanxi Yang, Dr. Dawen Pang, Dr. Bin Xi, Prof. Qiang Chen, Dr. Xudong Chen, Dr. Tamara Powers. I want to thank Kecheng Li in particular for introducing me to the research position in SDR. I had great fun mentoring Jun Feng and Yunfei Xu in the last year of my graduate career. Both of them happened to be my college alumni, and we shared similar enthusiasm in research and traveling. I also need to thank Teri Howard and Marie Purcell, my lab admins, for making my life easier.

I need to extend my warm gratitude to my friends. My time at Harvard was made enjoyable in large part due to my friends. I met most of my friends at Harvard in the residential halls or the Dudley house. So I need to first thank Garth McCavana and Ellen Fox for providing me the opportunity to serve the graduate community as the resident advisor (RA). The 2-year experience is definitely the highlight of my graduate life. I cannot thank my best friends Dr. Yue Liang and Xu Zhang enough. I feel fortunate to grow side-by-side with Yue since our first days in 2008. She is like my sister, whom I shared similar values and felt strong bond with. Thanks for all the emotional support, camaraderie, entertainment, and caring she provided. Meanwhile, we shared many important, happy moments together. I feel blessed to have witnessed those moments when she received the dream job offer, defended and got engaged with Billy in Hawaii. Xu, my dear, sweet hallmate, have put up with my loud laughs and cheered me up when I am down. Thank Dr. Luhan Yang, my close friend and current roommate, who has been a source of inspiration and shared the same passion for traveling and life. Thank Yu Lei for being a great friend and my RA cohort. He is one of the most energetic, hard-working and caring people I have ever met. Sometimes I wondered how he managed so many tasks at the same time. Thank Xue Rui for hosting the Chinese “Tea Party” seminar series with me. There are too many friends in a long list to thank: Chongyi Chen, who calmed me down when I felt frustrated; Jingyi Yu, my “only” guest student and talented magician, Lue Fang, Zhen Shi, Ruichao Ma, Dr. Irene Bredberg, Yin Chen, Xiaofei Ying, Zhuoyan Zhang, Molly Kwan, Seung-Yeon (Sally) Kang for making my life colorful.

I also need to thank many friends who are far away in other parts of the world, but shared my tears and joy. I am grateful for the long-lasting friendship starting from my college days with Sheng Jiang, Lei Wang, Min Huang, Yue Tan, Chunjing Jia, Kai Pan and Dr. Jingke Xu. I am thankful for the friendship I built on my road-trips, Min Ding, Fan Yang, Wentao Xiong, Di Chen and Xiaole Shen.

Lastly, I would like to thank my parents, Xiaoqin Chao and Guohua Yang, for their unconditional love and encouragement. Without their understanding and support, I cannot imagine going this far and completing this challenging PhD. I feel blessed with their love, while I feel guilty of not being able to be with them during the loss of my grandparents. I sincerely appreciate their trust in me that they give me the freedom to pursue my own dream.

Jing Yang

Cambridge, Massachusetts

December 27 2013

Page intentionally left blank

To my parents

for their love and support

獻給我的父親母親

感謝父母的愛與支持

Page intentionally left blank

Chapter 1 Introduction

1.1 Cobalt-Based Thin Films in Microelectronics

1.1.1 Overview of Cobalt-Based Thin Films

Thin films are widely used in microelectronics. In microelectronics, the device size continues to shrink to improve the performance, which sets challenging requirements for the integrated circuit (IC) fabrication. Novel materials and techniques are developed to maintain excellent device performances and structural reliability. For example, the development of complex 3D architectures requires the thin film materials must be grown conformally. Therefore, chemical vapor deposition (CVD) technique is favored over physical vapor deposition (PVD) because CVD method can produce high quality thin films with excellent conformality. CVD has been used as a tool in microelectronics for the growth of high permittivity (high-k) films, barrier materials, conductors such as metal gates.

In this thesis, we focus on the fabrication and characterization of cobalt-based thin films that have numerous applications in microelectronics industry.

Cobalt

Co[1] has proven to be an effective liner in copper interconnect. It has been shown that introduction of a thin Co interlayer between Cu and barriers such as TaN, WN or TiN increased adhesion at the interface, presumably thereby increasing the lifetime of the copper wires[2].

Co has also been used as a wetting layer to induce void-free filling of narrow copper lines by reflow of non-conformal PVD copper for sub-20nm nanostructures[3].

Cobalt is also a leading candidate for capping copper lines to improve the interconnect reliability against failure by electromigration[4].

Other applications of Co films include magnetic devices[5] and nano-catalysts for carbon nanotube synthesis[6].

Cobalt Nitride (Co_xN)

Co_xN[7] also can serve as an effective adhesion layer in the copper interconnect as it improve the adhesion between copper and the barrier layers.

Cobalt Silicide ($CoSi_2$)

$CoSi_2$, fabricated by the reaction of Co with silicon, is a useful contact material for source, drain and gate electrodes for CMOS structures[8] [9]. Among various metal silicides, $CoSi_2$ is considered as an attractive contact material because of its low resisitivity (10-20 μΩ·cm), no line-width dependence on the narrow Si line, and its superior chemical and thermal stability[10]. Although NiSi offers lower resistivity[11], the greater thermodynamic stability of $CoSi_2$ makes it more suitable for DRAM structures where high processing temperatures are required.

1.1.2 Precursor Chemistry in CVD/ALD of Cobalt-Based Thin Films

For Co CVD/ALD processes, the choice of suitable cobalt precursor is crucial to obtain high-quality cobalt or cobalt nitride films. Inorganic cobalt precursors, such as cobalt halides, have high decomposition temperature and low volatility, which renders them poorly suited

for CVD. Thus cobalt thin films deposition is typically carried out using various metalorganic precursors.

Most of the Co precursors can be classified into 4 kinds (as shown in Figure 1.1):

1. cobalt carbonyl ($Co_2(CO)_8$[8] [12] and derivatives thereof [8] [13] [14]),
2. cobaltocene (cyclopentadienyl)cobalt $Co(C_5H_5)_2$=$CoCp_2$ [8] [15] [16] [17])
3. cobalt acetylacetonates ($Co(acac)_2$ [18] [9] and derivatives thereof [17] [19])
4. cobalt amidinates (bis(N,N'-diisopropylacetamidinato)cobalt(II), $Co(^{i}Pr\text{-}MeAMD)_2$ [1] [2] [20] [21] [22]; bis(N-tert-butyl-N'-ethyl-propionamidinato)cobalt(II) [23] [7]).

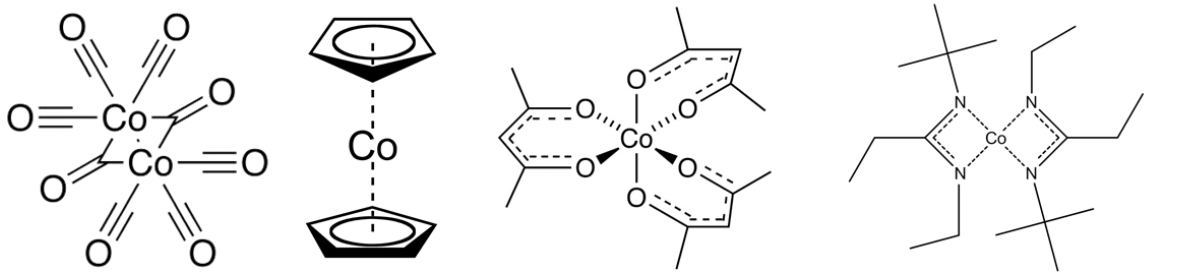

Figure 1.1. Examples of precursor types applied in the CVD of cobalt-based thin films.

Co can be deposited from thermal decomposition of $Co_2(CO)_8$ at substrate temperature ranging from 50°C to 200°C. Nevertheless, there are undesirable but thermodynamically favorable reaction pathways that compete with the deposition of pure Co, including precursor polymerization and formation of unstable $HCo(CO)_4$[12]. Co deposition from $CoCp_2$ [8] [15] [16] [17]or $Co(acac)_2$ [9] [18]typically requires reaction temperature above 250°C using H_2 or alcohol as reducing agent, and has shown conformal coating in trenches with 11:1 aspect ratio. Co grown by thermal ALD using $Co(^{i}Pr\text{-}MeAMD)_2$ and H_2 has demonstrated excellent

step coverage[1], coating holes with 40:1 aspect ratio conformally. In this thesis, we chose to study cobalt amidinates as CVD precursors as they have the potential of forming highly conformal cobalt and cobalt nitride film.

1.1.3 Cobalt Amidinates

In this thesis, we mainly studied chemical vapor deposition of cobalt-based thin films using cobalt amidinates. The synthesis of the cobalt amidinate precursors have been described elsewhere[11, 24].

The application of transitional metal amidinates as CVD precursors has several advantages.

1. The thermal stability of the precursor is enhanced due to the bidentate chelating effect.
2. Its reactivity and volatility can be tuned by changing the ligand.
3. The films deposited using amidinates tend to have little or no carbon contamination.
4. CVD using amidinates is capable of forming metal nitrides.
5. It does not produce any corrosive byproducts.

We have used two cobalt amidinate precursors:
Bis(n-tert-butyl-N'-ethyl-propionamidinato)cobalt(II) (or Co(^{t}Bu-Et-Et-amd)$_2$) and bis(N,N'-diisopropylacetamidinato)cobalt(II) (or Co(^{i}Pr-^{i}Pr-Me-amd)$_2$) (Dow Chemical Company). The formula of the two precursors is shown in Figure. 1.2. Table 1.1 listed the physical properties of the two. Both amidinates are good candidates as CVD precursors for cobalt-based thin films.

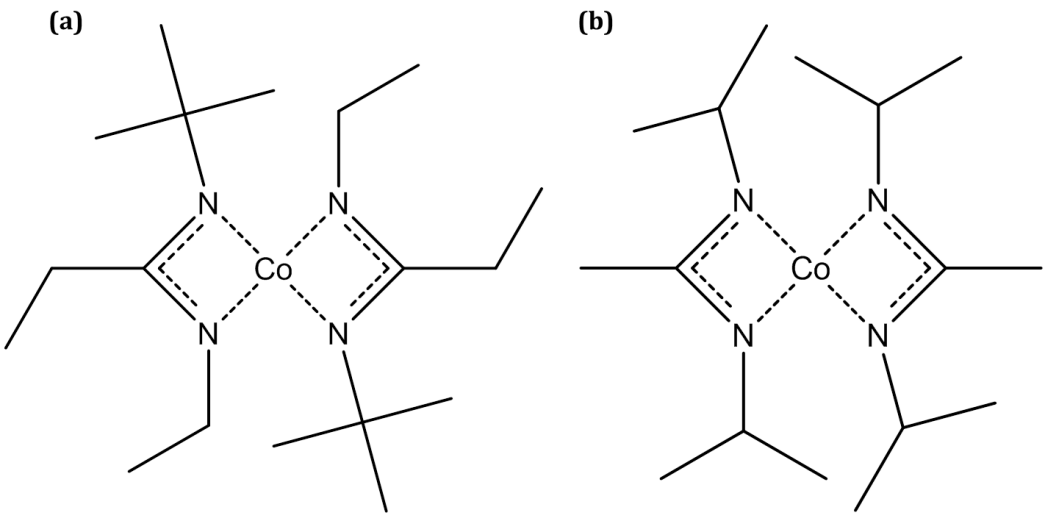

Figure 1.2. Formula of Co(^{t}Bu-Et-Et-amd)$_2$ and Co(^{i}Pr-^{i}Pr-Me-amd)$_2$ precursors.

Table 1.1. Comparison of Physical Properties of the Co(^{t}Bu-Et-Et-amd)$_2$ and Co(^{i}Pr-^{i}Pr-Me-amd)$_2$ precursors

Name	Co(^{t}Bu-Et-Et-amd)$_2$	Co(^{i}Pr-^{i}Pr-Me-amd)$_2$
Melting Point (°C)	-17 (liquid at room temp.)	84 (solid at room temp.)
Vapor Pressure	262 mTorr at 85°C 60 mTorr at 50°C	30 mTorr at 40°C
Thermal Stability	Relatively less stable	Relatively more stable (longer half-life in benzene)
Vaporization Rate at 80°C	50 nmol· min^{-1}·cm^{-2}	116 nmol· min^{-1}·cm^{-2}

Co(^{i}Pr-^{i}Pr-Me-amd)$_2$ has low volatility, and requires high evaporation temperature to provide sufficient vapor pressure for deposition. And the precursor cannot withstand heating for long periods. Direct-liquid-evaporation (DLE) CVD is introduced to avoid premature thermal decomposition of precursors. DLE-CVD is discussed in details in the next section.

1.2 Direct-Liquid-Evaporation (DLE) CVD

1.2.1 Benefits of DLE-CVD Method

Organometallic precursors generally have very low pressures (<<1 Torr at room temperature) and consequently require high evaporation temperature, often >100°C for efficient thin film depositions. However, the majority of precursors cannot withstand heating for long periods. The insufficient thermal stability of precursors leads to thermal decomposition in the heated container ("bubbler") or the heated pipelines in conventional CVD reactor. The decomposition of precursors could cause poor deposition uniformity, undesirable impurities in the film or reactor blockages.

This challenge of premature thermal decomposition associated with low-volatility precursors can be largely overcome by the use of DLE- CVD. DLE-CVD effectively prevents early thermal decomposition of precursors because precursor solution is typically stored at room temperature. The precursor is dissolved in an inert solvent, usually an ether (e.g. tetrahydrofuran (C_4H_8O or THF)[25] or a hydrocarbon (e.g. heptane, nonane, tetradecane etc.). The precursor solution is then delivered at a precisely controlled rate into a heated evaporator or vaporizer and transported by a carrier gas into the reactor zone along with other co-reactant vapors as shown in Figure 1.3 below.

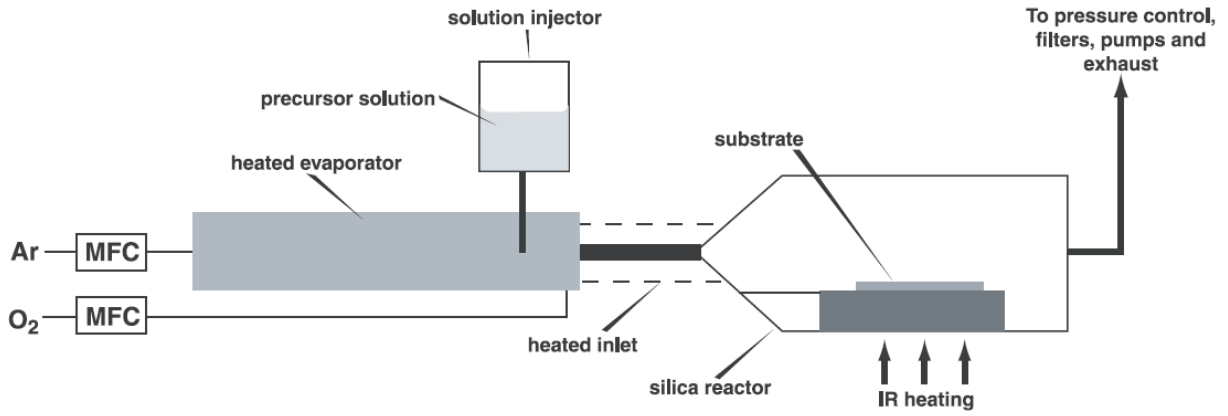

Figure 1.3. Schematic diagram of direct-liquid-evaporation CVD reactor[25].

1.2.2 Choice of Solvents

There are several requirements for choosing the solvent:

1. The solvent should be inert. The precursors must be soluble and stable for long periods in the specific solvent, and must not react with the solvent. For example, the ethanol solutions of iron, cobalt, nickel acetylacetonates precursors were stable after weeks in the open air, while copper acetylacetonates formed a precipitate in ethanol[26]. Therefore, ethanol cannot be used to prepare copper precursor solutions. Methanol was used instead to dissolve copper acetylacetonates.
2. The solvent should have a vapor pressure similar to the precursor.
3. In the case of ternary oxides, as multiple precursors co-exist in the solvent, they should not react with each other. And co-precursors should evaporate at similar temperatures otherwise it will be difficult to control the composition of complex oxides. Ideally, various precursors deposit oxides in a similar temperature regime.

DLE-CVD is now widely used for the deposition of electroceramic oxides[25], metal oxides (high-k) [27], and metals including Ag[26 28], Co[26 18], Cu[26 29], Ni[30 31 26], and Ru[32].

Here listed a number of literature examples of precursor solutions used in DLE-CVD of various metals.

Table 1.2. Literature Examples of Precursor Solutions used in DLE-CVD of various metals.

Material	Precursor	Solvent	Year	Reference
Ag	Silver(I)-2,2-dimethyl-6,6,7,7,8,8,8-heptafluoro-3,5-octanedionatotriethylphosphine [Ag(fod)(PEt_3)], liquid at 30°C	-	2004	[28]
Ag	Silver nitrate	Ethanol	2007	[26]
Co	Cobalt acetylacetonates	Ethanol	2007	[26]
Co, Co_2C	Cobalt (II) acetylacetonate ($Co(acac)_2$)	Alcohol	2007	[18]
Co	bis(N,N'-diisopropylacetamidinato)cobalt(II)	Tetradecane	2014	this chapter
Co_3O_4	Cobalt (II) acetylacetonate ($Co(acac)_2$)	Toluene	2006	[33]
Cu	Copper acetylacetonates	Methanol	2007	[26]
Cu	(hfac)-Cu(TMVS), ((hexafluoroacetylacetonate) Cu (trimethylvinylsilane))	-	1997	[29]
Fe	Iron acetylacetonates were used as precursors for iron, cobalt, nickel,	Ethanol	2007	[26]
HfO_2	$Hf(O^tBu)_4$, $Hf(O^tBu)_2(dmae)_2$ and $Hf(O^tBu)_2(mmp)_2$ (dmae = dimethylaminoethoxide, $OCH_2CH_2N(CH_3)_2$))	*n*-hexane or with octane	2005	[27]
Ni	Nickel acetylacetonates	Ethanol	2007	[26]
Ni	Bis(N,N'-di-tert-butylacetamidinato)nickel(II), $Ni(MeC(NtBu)_2)_2$.	Tetrahydrofuran (THF), or tetrahydronaphthalene (tetralin)	2010	[30],[31]
Ru	Bis(2,2,6,6-tetramethyl-3,5-Heptanedionato)(1,5-cyclooctadiene)ruthenium, solid	Tetrahydrofuran (C_4H_8O or THF)	2003	[32]
$SrTiO_3$	$Sr(tmhd)_2$ and $Ti(tmhd)_2(O^iPr)_2$ or a single heterometallic precursor $Sr_2Ti_2(tmhd)_4(O^iPr)_8$	Octane	2005	[27]

1.2.3 Design of Liquid Delivery System

The flow rate of precursor solution is precisely controlled in small amounts before entering the vaporizer. Several designs have been used for liquid source delivery control and evaporation system.

Several designs were applied to precisely control the speed of precursor solution: such as precision micropump (MKS Instruments, Inc) [32], syringe pumps[30-31], liquid mass flow controller (Horiba-Stec liquid flow controller, Brooks Instrument's Quantim QMBC Coriolis flow controllers) [28,30, 31], microvalve[27], 4-pinholes injector with diameters of 0.1 mm (Bosch) [26]. These precursor solutions first vaporized, then entered the reaction zone together with other co-reactants. In our home-built DLE-CVD Co reactor system, we used a coriolis flow controller to inject the liquid precursor solution at a controlled speed. The detailed description will be discussed in the next section.

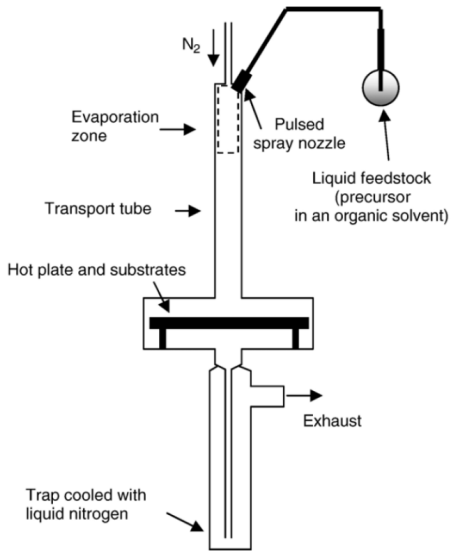

Figure 1.4. Schematic presentation of the pulsed-spray evaporation CVD reactor for transition metals deposition[26]. [The inlet tube is 25 cm long and has an inner diameter of 2.5 cm.]

Nebulization method[28] has been used to generate the vapor, however it also generates small particles made up of any non-volatile residue in the precursor. The non-volatile residue can easily block the liquid flow in the nebulizer and cause the instrument breakdown. This method is also known as aerosol-assisted MOCVD because it uses a nebulizer (for example, spray nozzle[26] as shown in Figure 1.4 above) to break up the liquid or solution into tiny droplets, typically a few microns in diameter. These are then heated rapidly by a hot carrier gas because of their high surface to volume ratio. We have used Brooks Instrument atomizer, similar to a nebulizer, to assist the vaporization process by breaking up the fluid into small micron size droplets before contacting hot carrier gas. However, the atomizer was susceptible to slight contamination and easily got clogged as it used a 0.02" diameter tubing to break up the fluid. Therefore, nebulization method is not recommended for vapor generation.

A better method, which avoids particle generation and demonstrates a steadier performance, flows the liquid along the heated tubing coil inside the oven. A similar vaporizer design has been described elsewhere[34]. The temperature of the tubing is kept high enough to vaporize the liquid completely without causing it to boil and produce bubbles or particles, or to decompose in the short period before it vaporizes. This method takes advantage of a faster heat transfer from a solid to a liquid than from a gas to a liquid. Thus, the vaporization by this method can be faster than the nebulization method. At the same time, any non-volatile residue left by this evaporation method tends to adhere to the bottom of the tube. Before the residue builds up for a long period of time and starts to contaminate the vapor stream, the inexpensive tubing can be cleaned or replaced. Some precursors might decompose quickly when in contact with stainless steel. The inside of the

tubing can be coated with pure silica glass to prevent precursor decomposition. As a result, this method of using heated stainless steel tubing coil was chosen over the nebulization method for DLE-CVD processes [30, 31].

The liquid delivery has been applied both in pulsed mode[27 33] or continuous mode[30-31]. For pulse mode, many parameters will influence the amount of the injected liquid: the injection opening time, the injection frequency, the solution viscosity and the differential pressure between the liquid reservoir and the evaporator[27]. The pulse mode is relatively more complex. We studied the cobalt, cobalt nitride deposition by DLE-CVD using a continuous flow of precursor solution before vaporization.

DLE-CVD enables production of a higher partial pressure of precursor vapor in the deposition region. High vapor pressure is obtained because of suddenly heating the precursor from its stable state at room temperature to a high temperature, well above the bubbler maximum operation temperature. The precursor will not decompose significantly since it is heated briefly.

Higher partial pressure provides many benefits:

1. Higher growth rate, enabling higher throughput and less expensive production of films.
2. More uniform thickness of films along the direction of the gas flow over the substrate surface, because of the saturation of the growth rate at higher partial pressure.
3. Higher step coverage inside narrow holes and trenches, because of saturation of growth rate at higher partial pressure.

4. More complete coverage for thinner films, because of denser nucleation.
5. Smoother films, because of denser nucleation and less agglomeration during the shorter growth time enabled by higher growth rates.

This technique can be applied to a wide range of precursors, especially for those having low vapor pressure.

1.2.4 Design of Home-Built DLE-CVD Reactor

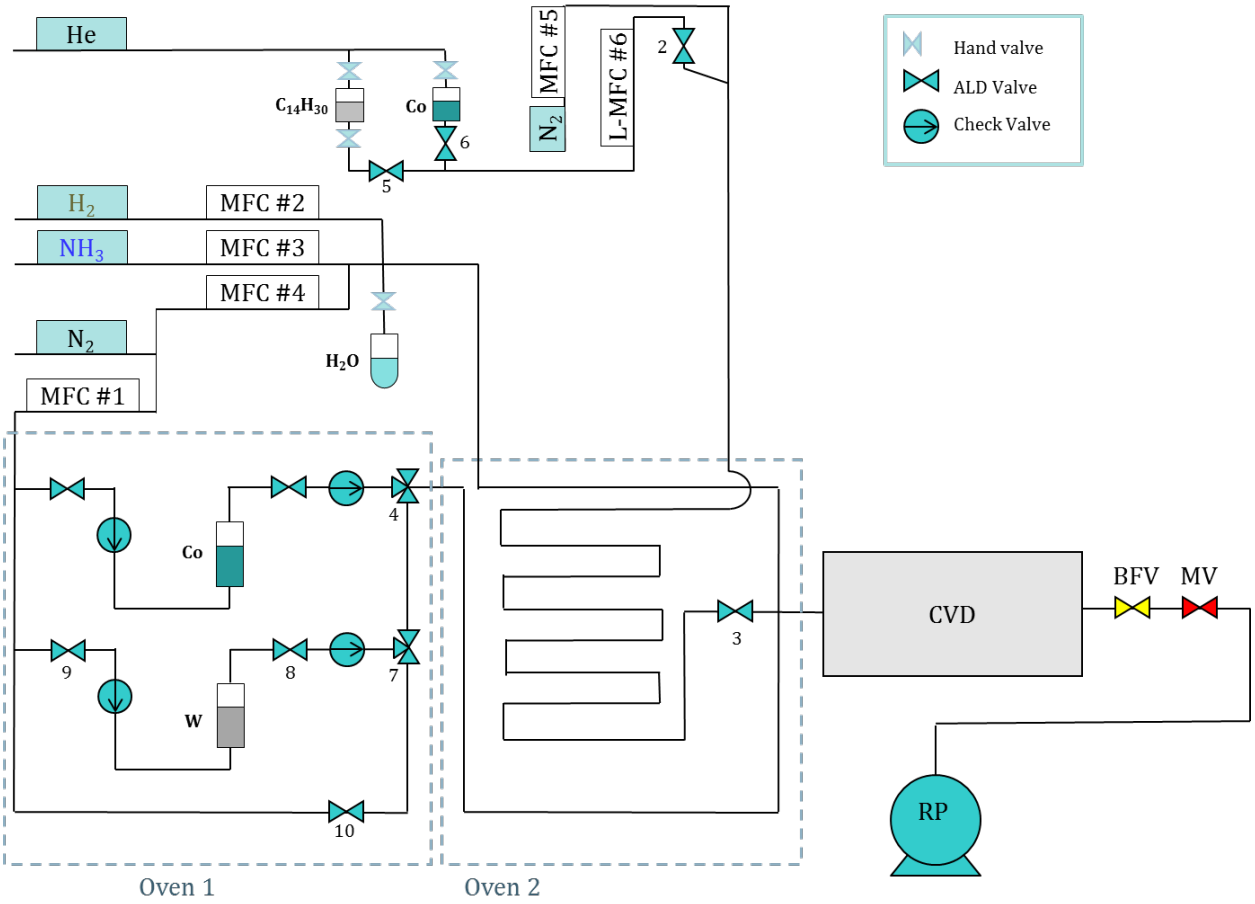

Figure 1.5. The schematic diagram of the DLE-CVD cobalt reactor

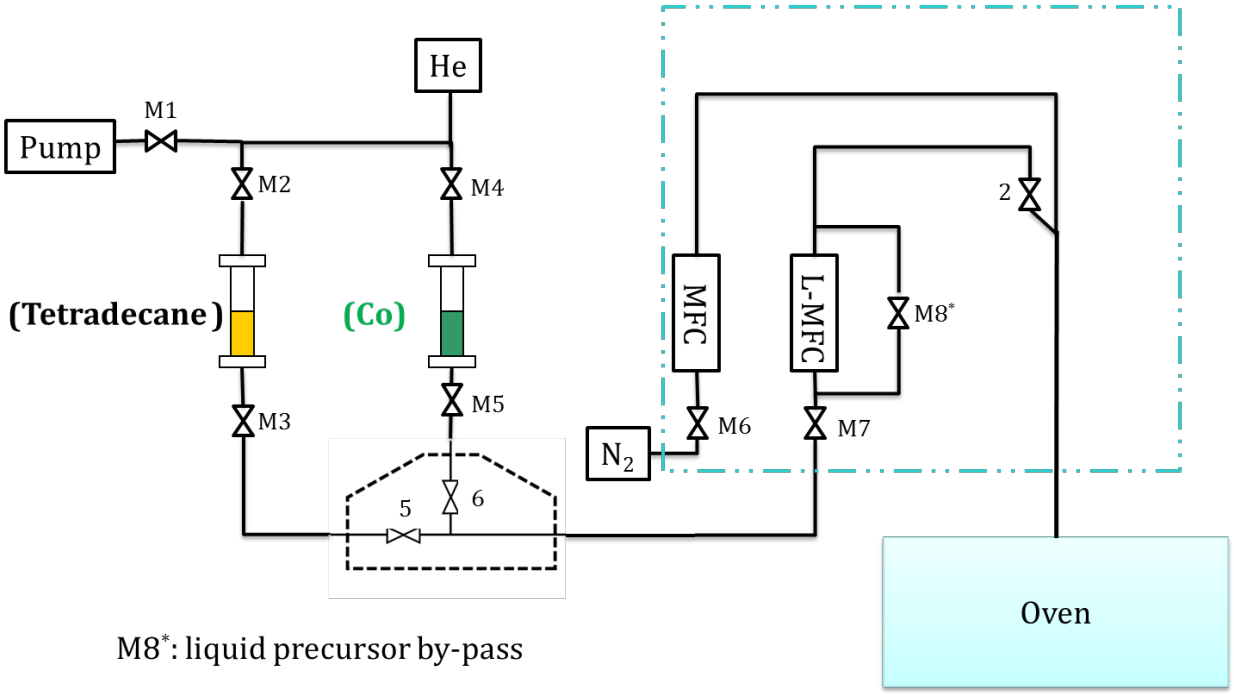

Figure 1.6. Schematic Diagram of the DLE-CVD Co Precursor Solution Delivery System

Figure 1.5 and Figure 1.6 show the schematic diagram of the DLE-CVD Co reactor and its precursor solution delivery system respectively. Helium (He) gas is used as the push gas to push the cobalt precursor solution to the liquid MFC (mass flow controller). Then the MFC can control the delivery rate according to the deposition needs. Then the precursor solution is mixed with N_2 carrier gas before entering the heated stainless steel coil in the oven. The precursor solution becomes vaporized and reacts with co-reactant gases NH_3 and/or H_2 to deposit cobalt-based thin films.

1.3 Overview of Thin Film Characterization Techniques

Characterizations of thin film materials are critical to tailor the materials for specific applications. In this thesis, we applied various characterization techniques to study different aspect of material properties. Those characterization tools can be categorized into

three major fields of applications – physical/ structural analyses, chemical/elemental analyses and electrical analyses[35]. Additionally, there are a host of analyses which are tailored to understand specific properties (e.g. adhesion, stress, hardness, etc.). For example, the adhesion energy between thin films can be estimated by four point bending (FPB) [36] [37]. These analyses are crucial to the design and development of functional materials with optimized mechanical, electrical, optoelectronic, magnetic or superconducting properties for applications in nanoelectronics, energy generation and beyond.

Physical/ structural analysis can be performed by scanning electron microscopy (SEM), (scanning) transmission electron microscopy ((S)TEM), focused ion beam (FIB) microscopy, atomic force microscopy (AFM), and X-ray diffraction (XRD). These tools aim to understand the fundamental physical and structural properties of thin films, including film thickness, morphology and structure.

Chemical/elemental analyses can be evaluated by Auger electron spectroscopy (AES), energy dispersive spectroscopy (EDS), time-of-flight secondary ion mass spectroscopy (tof-SIMS), X-ray photoelectron spectroscopy (XPS), electron energy loss spectroscopy (EELS), Rutherford backscattering spectroscopy (RBS) and atom probe tomography / microscopy (APT/ APM). These tools can identify surface, near-surface or bulk elements and compounds, as well as their lateral and depth spatial distributions. These tools are limited by spatial resolution and detection sensitivity. Generally, probe size/ analytical volume is always a trade-off with detection limits[38].

Here we summarize the capabilities and limitations of each chemical analytical methods in Table 1.3. Figure 1.7 shows the comparative strengths and weaknesses for particular analytical applications in terms of detection sensitivity and spatial resolution.

Table 1.3. Summary of Major Chemical Characterization Techniques

Method	Primary Beam	Detected Signals	Elemental Sensitivity	Detection Limit	Lateral Resolution	Effective Probe Depth
APT/APM	-	Ions	H - U	~ few ppm	0.3 – 0.5nm	~ 1 - 3 Å
AES	Electron	Auger electron	Li- U	~ 0.1~1%	~500 Å	~ 15 Å
EDS	Electron	Characteristic X-ray	Na- U	~0.1%	~ 1 μm	~ 1 μm
RBS	He+ ions	Backscattered ions	He-U	~ 0.1%	~ 1 mm	~ 4 μm
SIMS	Cs^+, O_2^- ions	Secondary ions	H-U	> 0.1 ppm	~ 1 μm	~ 15 Å
XPS	X-ray or ultraviolet	Photoelectrons	Li-U	~ 0.1-1%	~ 100 μm	5-15 Å
XRD	X-ray	Diffracted X-ray	Crystalline Material	5%	> 1 μm	> 1 μm

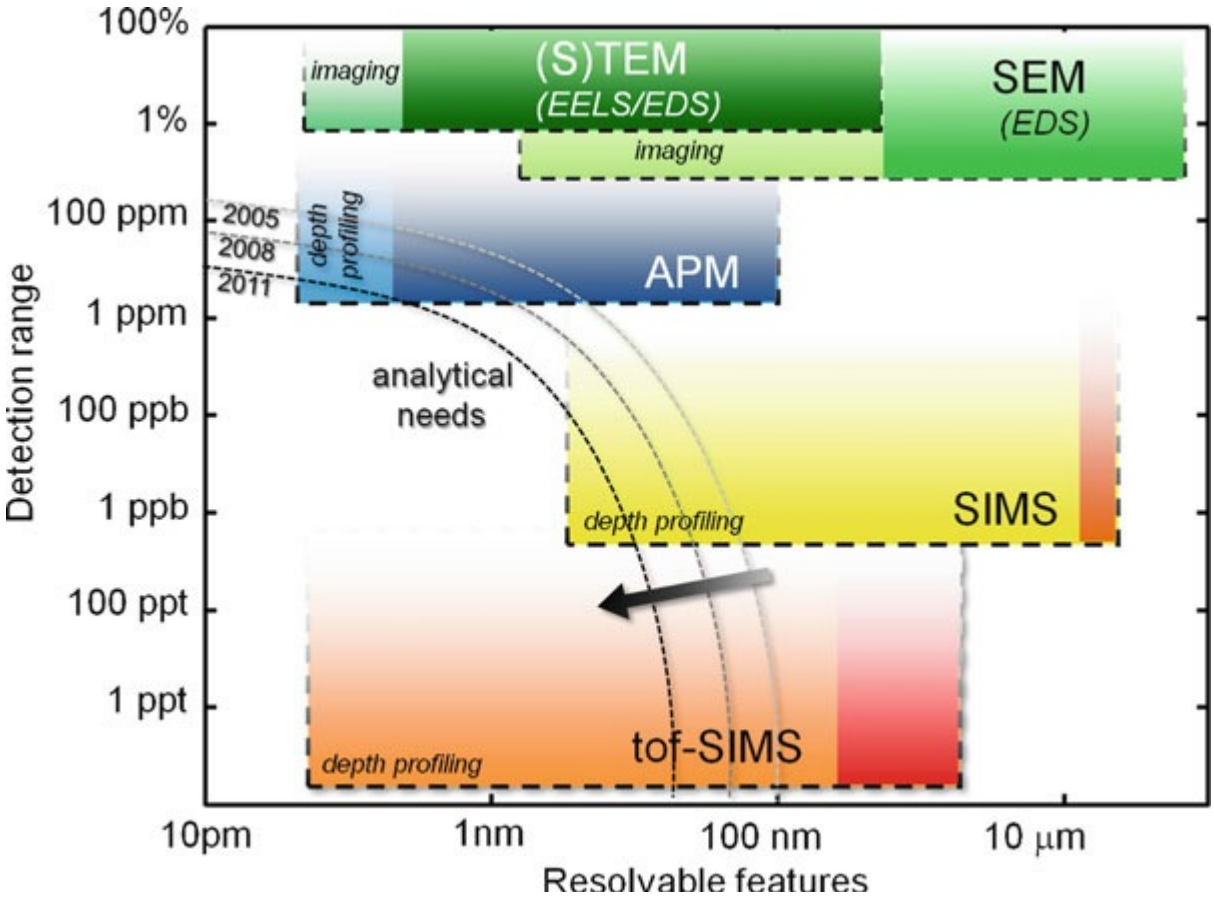

Figure 1.7. Typical detection range (i.e. elemental sensitivity) and spatial resolution of some common microscopy and microanalysis techniques. The area delineated with dashed lines corresponds to the specific case of imaging ((S)TEM, SEM) or depth profiling (SIMS, APM). (Source: Atom probe microscopy (APM) book[39].)

Electrical analyses can be carried out by four point probe (sheet resistance), I-V measurements. These tools are useful for measuring the electrical properties of thin films.

These characterization techniques have been reviewed elsewhere[35 38]. In the next section, I would like to highlight the technique of atom probe microscopy (APM) that enables three-dimensional compositional and structural analysis at the atomic and near-atomic scales.

1.4 Atom Probe Microscopy (APM)

1.4.1 Features of Atom Probe Microscopy

Atom Probe Microscopy (APM) is an effective material characterization technique, complementary to electron microscopy, which offers unique insights into both the chemical composition and the atomic structure of matter. APM produces three-dimensional compositional images at the atomic scale (high spatial resolution of sub-0.3 nm in 3 dimensions) with high analytical sensitivity (10 ppm). Due to its capability of three-dimensional analysis, APM excels at an investigation of subsurface or buried features in specimens, including one-dimensional features such as dislocations, two-dimensional features such as layers and interfaces, and three-dimensional features such as precipitates.

APM is unique among analytical instruments. Several features coupled make it stand out[40]:

1. *Unmatched spatial resolution in three dimensions (~ 0.2 nm achievable).*
   In comparison, the highest spatial resolution technique among the rest microscopy technique is the scanning transmission electron microscopy (STEM) which can provide 1 nm resolution laterally from x-ray emissions and 0.2 nm resolution laterally from electron energy loss events. However, these images are integrated through the specimen thickness which is about 10 nm.
2. *High analytical sensitivity (10 appm).*
3. *High detection efficiency (>50%).*
4. *Abilities to detect all elements with equal efficiency.* This is because the time-of-flight (TOF) mass spectrometer is equally sensitive to all elements and the microchannel

plates (MCPs) that are used as the detector has no selectivity towards different elements.

5. *No prior knowledge of the composition is needed.*

APM offers an unparalleled combination of compositional imaging at the atomic scale of multidimensional objects with high analytical sensitivity. All these qualities make APM a powerful tool for accelerating the development of new materials, in particular, materials for the microelectronics industries[40]. In this thesis, we applied APM to reveal the 3D atomic architecture of the cobalt-based thin films.

1.4.2 Fundamentals of Atom Probe Microscopy

APM exploits the effect of field evaporation to successively remove the atoms at the apex of a needle-shaped specimen.

Field evaporation is the field-induced removal of an atom from a surface that is subject to a very intense electric field, on the order of tens of $V \cdot nm^{-1}$. Even now the exact mechanism underpinnings of this process are yet to be totally unraveled. The atoms close to the apex of the specimen are progressively ionized with single or multiple charges and desorbed from the surface. This ionization is induced by a combined effect of a standing (DC) electrostatic field and either high voltage (HV) or laser pulses transmitted to the surface atoms. The ions generated are pulled away from the surface and moved towards a position-sensitive detector along trajectories that are initially curved and gradually become almost linear (the reflectron compensator configuration). The detector collects the ions and records their impact location. The application of voltage-pulsing or laser-pulsing permits the measurements of the TOF of each individual ion. The TOF can determine the mass-to-

charge ratio, which enables the elemental identification of each detected ion. This process is shown schematically in Figure 1.8.

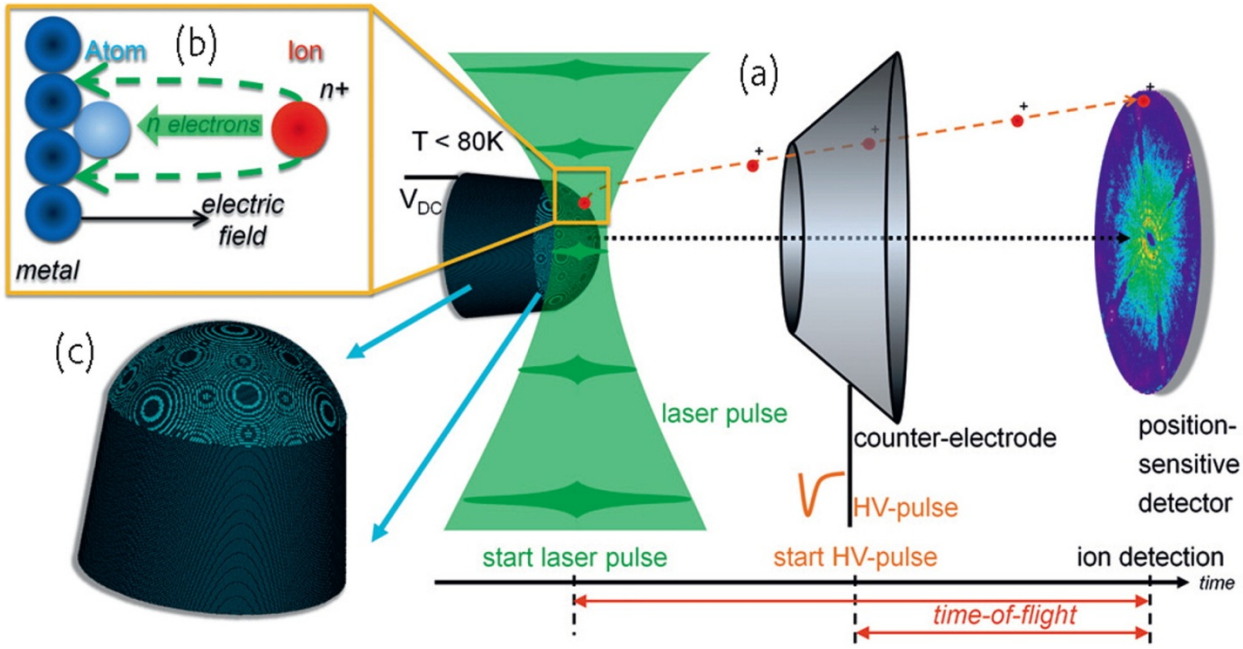

Figure 1.8. (a) Schematic view of the atom probe microscope. (b) The field evaporation process. (c) Close-up representation of the specimen, here a simple stack of hard spheres on a body-centered cubic lattice. The most protruding atoms at the surface are shown in light blue and form a pattern related to the specimen's crystal structure. (Source: Atom probe crystallography review[41], 2012)

The electric field required for field evaporation of an atom is generally called the *evaporation field* and is specific to each element and phase in the material. Besides the application of the high voltage in the range of a few kilovolts, the specimen needs to be sharpened into the form of a tip with a radius of curvature in the range of 50 to 150 nm and a sharp shank angle (typically less than 20°) to reach the required evaporation field. The electric field at the surface can be estimated by the formula below:

$$F = \frac{V}{k_f R}$$

where F is the electric field induced at the apex of this tip with the radius of curvature R. The shape of the tip here is modeled as a truncated cone with hemispherical cap. k_f is the *field factor* or referred as the *field reduction factor*, which is the constant that accounts for the tip shape and its electrostatic environment.

This specimen geometry generates a highly divergent electric field that can be used advantageously to provide a projection with a magnification of the order of 10^6. This implies atoms separated by less than 0.2 nm at the surface of the specimen will strike the detector at locations separated by 0.2 mm, a distance that is easily differentiable. The specimen is cooled down to cryogenic temperatures to reduce surface diffusion, thereby to improve the spatial resolution. The impact position on the detector can be used to recalculate, with a simple reverse-projection algorithm, the original position of the atom on the specimen within the lateral (x-y) plane. Then, by a sequential increment of the depth coordinate, a 3D atomically resolved tomographic reconstruction of the analyzed volume can be progressively built.

The APM can operate in both HV-pulsing and laser-pulsing mode.

In the HV-pulsing mode, the specimen must have electrical conductivity greater than 10^2 S/cm[42]. This has limited the application of the voltage-pulsed atom probe primarily to metals. The evaporation field is induced by standing (DC) voltage and HV pulse combined. The DC voltage typically generates around 80% of the evaporation field. The negative HV pulses (generally 15∼20% of the standing voltage) are then superimposed by using a counter-electrode placed in front of the specimen. The *pulse fraction* is defined as the ratio between the amplitude of the HV pulses and the DC standing voltage. The pulse fraction,

the standing voltage, and the specimen temperature need to be optimized in the experiment so that there is no preferential evaporation of the elements with the lowest evaporation field, and effectively no atoms field evaporated by the standing voltage alone. The number of atoms field evaporated in any pulse from the specimen apex region can be readily adjusted by tuning the standing voltage. Typically, one or fewer atoms are evaporated per pulse to ensure the detector can correctly encode each ion. As the radius of the specimen increases throughout the atom probe experiment, the required evaporation field increases as indicated by the formula. To maintain a constant detection rate, the amplitude of the standing voltage must continually increase, and the amplitude of the HV pulses must increase in proportion to the DC voltage to keep a constant pulse fraction.

In the laser-pulsing mode, the ultra-short-duration laser pulses, such as picosecond and femtosecond laser pulses, are focused onto the apex of the specimen to induce the field evaporation at the standing voltage on the specimen. The mechanism is due to thermally assisted field evaporation. The pulsed-laser atom probe permits the analysis of high-resistivity materials, including semiconductors, ceramics, biominerals, and organic materials, without excessive specimen failures. During operation, the energy of laser pulses is generally kept constant throughout the experiment, which means the pulse fraction varies as the DC voltage evolves, unlike in HV-pulsing mode.

The pulsed field evaporation is precisely controlled by HV or laser pulses. This allows precise control over the instant in time of departure of the ion from the tip's the surface. The *TOF (time-of-flight)*, t, of an ion is defined as the time between the application of the pulse that triggers the ion evaporated from the surface and the moment that the ion

reached the detector. In the field evaporation process, the potential energy of the atom on the surface due to the electric field, neV, is converted into kinetic energy $\frac{1}{2}mv^2$, assuming the ion leaves the specimen with no initial velocity. Here, ne is the charge of the ion, e is the charge on an electron, V is the total voltage applied on the specimen, m is the mass of the atom, and $v = d/t$ is the speed of the atom, d is the distance between the specimen and the detector, and t is the time of flight. Therefore, the mass-to-charge ratio m/n of the ion is directly related with the TOF:

$$\frac{m}{n} = \frac{2eV}{v^2} = \frac{2eV}{d^2}t^2$$

Measuring the TOF enables the elemental identification of each detected ion. Along with the measurement of the each ion's location, the APM provides 3D compositional mapping of materials with atomic-scale resolution.

1.4.3 Historical Background of Atom Probe Microscopy

Atom Probe Microscopy has evolved from its genesis - field ion microscopy (FIM), the first technique to enable imaging of individual atoms in direct space back in 1950s. Erwin W. Müller invented the field electron emission microscope in 1935, which was further adapted into the field ion microscope (FIM) in 1955. The FIM provides atomic-resolution imaging of the surface of a sharp needle-shaped specimen. Müller and his coworkers invented FIM that resolved individual tungsten (W) atoms on the surface of a sharply pointed W tip by cooling it down to 78K and employing helium imaging gas. By 1968, Müller introduced the atom-probe field-ion microscope (APFIM), which consists of a FIM and a time of flight (TOF) (TOF) mass spectrometer. The APFIM utilizes controlled pulsed field evaporation by a high

voltage pulse to determine the TOF of individual ions, thereby determining chemical identities from their the mass-to-charge ratios (m/n). Since the invention of APM, there have been numerous major improvements towards hardware configurations, including the pulsed-laser atom probe in the late 1970s, the position-sensitive atom probe or 3D atom probe in 1980s and local electrode atom probe in 1990s.

The detailed historical developments of the instrumentation can be found in review articles by Kelly, Larson, Miller, and Seidman[39-45]. The timeline of the instrumentation development is summarized in the table below (Table 1.4). The evolution of the atom probe from the field ion microscope in terms of its hardware is shown in Figure 1.9.

Table 1.4. The historical temporal evolution of an atom probe microscopy (APM).

Müller	Müller	Müller	Kellogg and Tsong	Multiple groups	Kelly
1935	1955	1968	Late 1970s	1980s	1990s
Field electron emission microscope	Field ion microscope (FIM)	Atom probe field ion microscope (APFIM)	Pulsed-laser atom probe	three-dimensional atom probe (3DAP)	local electrode atom probe (LEAP)

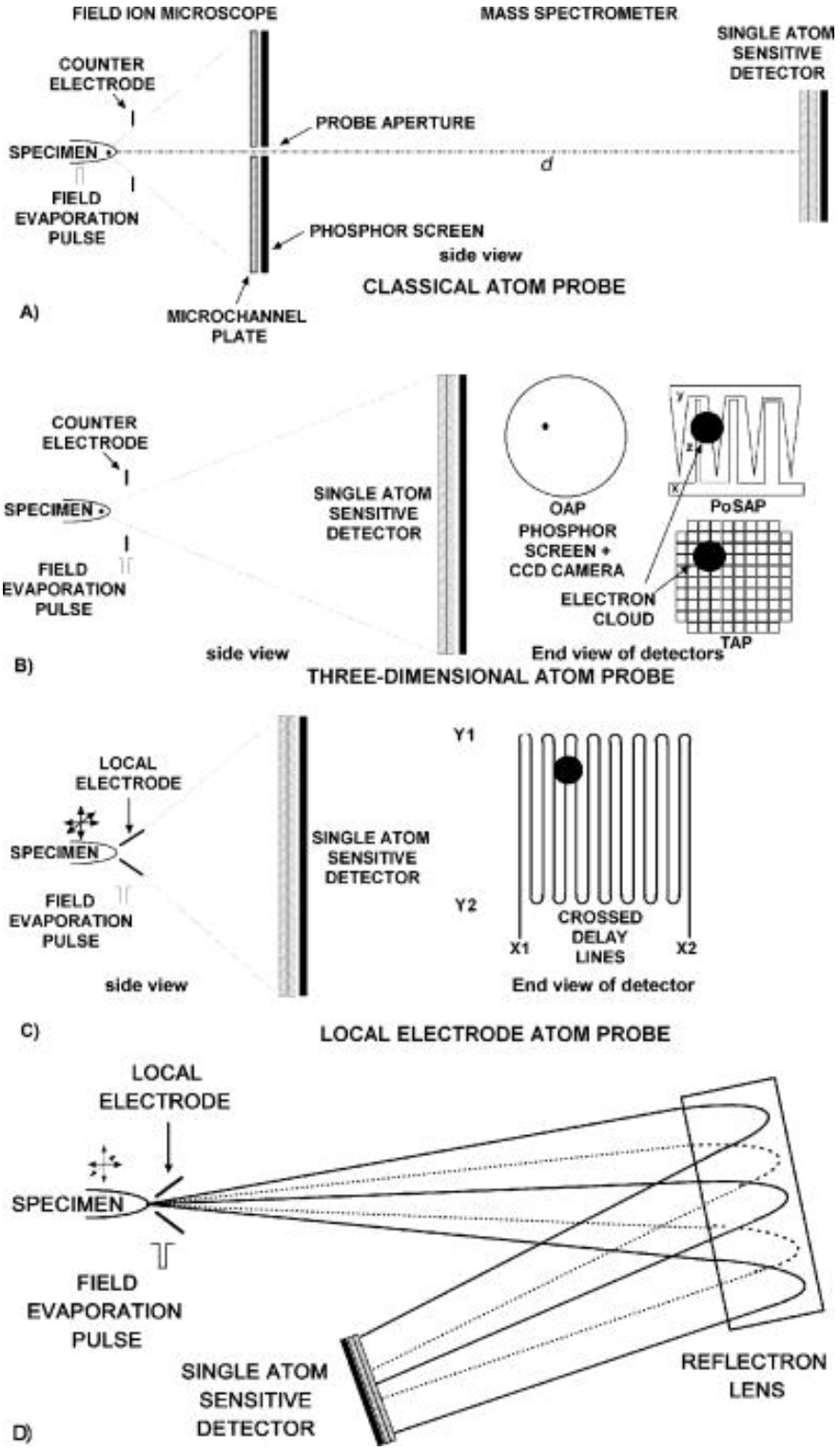

Figure 1.9 (a) Schematic diagrams of the original or "classical" atom probe, (b) three-dimensional atom probe with different detectors, (c) local electrode atom probe, and (d) reflectron-compensated 3DAP (large angle reflectron compensator) (source: APM review by Kelly[42]).

The modern commercial atom probes allowed practical applications for a broad range of potential applications due to several important technological advances in both hardware and software over the past few decades[44]:

1. The implementation of laser-pulsing capabilities enabled application of the technique to non-conductive materials, in additional to metals.
2. The introduction of LEAP (local electrode) and LARC (large angle reflectron compensator) design reduced the TOF noise and increased the flight path of evaporated ions, providing a larger field of view and a higher mass resolution. The field of view increased by two orders of magnitude since 2000 (to 3×10^4 nm^2) [42, 45]. The mass-resolving power (MRP or $m/\Delta m$) improved by an order of magnitude (to >1,500) since 2000[42, 45]. The pulsing rate can go up to 250 kHz, two orders of magnitude faster than previous instruments. Though the maximum pulse repetition rate may have to be limited (<500 kHz) due to the long time of flight.
3. High-gain, low-noise multichannel plates (MCPs) are used to determine the TOF of individual ions.
4. The position-sensitive detector obtained by the combination of a MCP and a delay-line detector in series yields the x-, y-, and z- coordinates of atoms in a 3D specimen in direct space.
5. The implementation of dual-beam focused ion beam (FIB) allowed for increasingly precise site-specific specimen preparation and analysis.
6. Data-collection rates increased by of four orders of magnitude (to 5×10^6 $atoms \cdot min^{-1}$) since 2000[45]. The development of high-speed electronics permits the

collection of large data sets (hundreds of millions of atoms) in relatively short period of time.

7. High-end workstations make it possible to analyze increasing large data sets using sophisticated data analysis programs.

These recent technological improvements provided the modern APM numerous benefits, large field of view with high mass resolution, high data collection rate, and planar microtip capability. These advances have resulted in a considerable interest in APM for the atomic scale investigation of structural and functional materials[41].

1.4.4 Limitations of Atom Probe Microscopy

As with any analytical technique, APM has limitations. Most notably, not all specimens will run successfully. For example, the specimen is prone to fracture when the mechanical stresses in the specimen near the apex approach the cohesive strength of the material. The specimen fracture is common in the atom probe, which makes it challenging to obtain enough data. And for some complex material structures, the reconstruction of the 3D compositional images can suffer from severe distortions. Additionally, the detection efficiency is limited by MCPs' open area, which detects 60% of all the ions hitting them. Furthermore, the analyzed volume is limited by the spatial limitation of the field of view (about 200nm). Common data sets today are 100 nm in diameter by 100 nm in depth (10^6 nm^3) with 10^7-10^8 atoms. Image can potentially contain 10^9 atoms from the specimen, which offers 100 ppb (parts per billion) sensitivity. At today's highest data collection rate of 10^6 atoms/min, it will take 17 hr of data collection[42].

The bases of APM, including FIM, have been in practice for over 60 years, but the technology is just beginning to gain wide acceptance. The technique will continue to develop out of the research labs towards widespread adoption. Ideally, the APM can identify every atom and its position, and then APM may be called ultimate tomography. The technique will continue its evolution towards this goal[46].

1.5 References

1 B. S. Lim, A. Rahtu, and R. G. Gordon, Nat Mater **2**, 749 (2003).

2 Z. Li, R. G. Gordon, D. B. Farmer, Y. Lin, and J. Vlassak, Electrochemical and Solid-State Letters **8**, G182 (2005).

3 Y. Kokaze, S. Kodaira, Y. Endo, J. Hamaguchi, M. Harada, S. Kumamoto, Y. Sakamoto, and Y. Higuchi, Japanese Journal of Applied Physics **52**, 05FA01.

4 H. Nakano, T. Itabashi, and H. Akahoshi, Journal of The Electrochemical Society **152**, C163 (2005).

5 M. Kisielewski, A. Maziewski, M. Tekielak, A. Wawro, and L. T. Baczewski, Physical Review Letters **89**, 087203 (2002).

6 N. Li, X. Wang, S. Derrouiche, G. L. Haller, and L. D. Pfefferle, ACS Nano **4**, 1759 (2010).

7 H. B. Bhandari, J. Yang, H. Kim, Y. Lin, R. G. Gordon, Q. M. Wang, J.-S. M. Lehn, H. Li, and D. Shenai, ECS Journal of Solid State Science and Technology **1**, N79 (2012).

8 G. J. M. Dormans, G. J. B. M. Meekes, and E. G. J. Staring, Journal of Crystal Growth **114**, 364 (1991).

9 P. A. Premkumar, N. Bahlawane, and K. Kohse-Höinghaus, Chemical Vapor Deposition **13**, 219 (2007).

10 K. Maex, Materials Science and Engineering: R: Reports **11**, vii (1993).

11 B. S. Lim, A. Rahtu, J.-S. Park, and R. G. Gordon, Inorganic Chemistry **42**, 7951 (2003).

12 J. Lee, et al., Journal of The Electrochemical Society **153**, G539 (2006).

13 P. A. Lane, P. E.Oliver, P. J. Wright, C. L. Reeves, A. D. Pitt, and B. Cockayne, Chemical Vapor Deposition **4**, 183 (1998).

14 A. R. Ivanova, G. Nuesca, X. Chen, C. Goldberg, A. E. Kaloyeros, B. Arkles, and J. J. Sullivan, Journal of The Electrochemical Society **146**, 2139 (1999).

15 E. T. Hunde and J. J. Watkins, Chemistry of Materials **16**, 498 (2004).

16 H. Shimizu, K. Sakoda, T. Momose, M. Koshi, and Y. Shimogaki, Journal of Vacuum Science & Technology A: Vacuum, Surfaces, and Films **30**, 01A144 (2012).

17 H.-B.-R. Lee and H. Kim, Electrochemical and Solid-State Letters **9**, G323 (2006).

18 P. A. Premkumar, A. Turchanin, and N. Bahlawane, Chemistry of Materials **19**, 6206 (2007).

19 M. F. Chioncel and P. W. Haycock, Chemical Vapor Deposition **11**, 235 (2005).

20 P. de Rouffignac, Z. Li, and R. G. Gordon, Electrochemical and Solid-State Letters **7**, G306 (2004).

21 H.-B.-R. Lee, W.-H. Kim, J. W. Lee, J.-M. Kim, K. Heo, I. C. Hwang, Y. Park, S. Hong, and H. Kim, Journal of The Electrochemical Society **157**, D10 (2010).

22 Y. T. Chong, E. M. Y. Yau, K. Nielsch, and J. Bachmann, Chemistry of Materials **22**, 6506 (2010).

23 H. Shimizu, Y. Suzuki, T. Nogami, N. Tajima, T. Momose, Y. Kobayashi, and Y. Shimogaki, ECS Journal of Solid State Science and Technology **2**, P311 (2013).

24 Z. Li, D. K. Lee, M. Coulter, L. N. J. Rodriguez, and R. G. Gordon, Dalton Transactions **0**, 2592 (2008).

25 C. J. Anthony and R. C. Paul, Journal of Physics D: Applied Physics **36**, R80 (2003).

26 N. Bahlawane, P. Antony Premkumar, K. Onwuka, K. Rott, G. Reiss, and K. Kohse-Höinghaus, Surface and Coatings Technology **201**, 8914 (2007).

27 C. Dubourdieu, et al., Materials Science and Engineering: B **118**, 105 (2005).

28 L. Gao, P. Härter, C. Linsmeier, J. Gstöttner, R. Emling, and D. Schmitt-Landsiedel, Materials Science in Semiconductor Processing **7**, 331 (2004).

29 D. Bollmann, R. Merkel, and A. Klumpp, Microelectronic Engineering **37–38**, 105 (1997).

30 Z. Li, R. G. Gordon, V. Pallem, H. Li, and D. V. Shenai, Chemistry of Materials **22**, 3060 (2010).

31 Z. Li, R. G. Gordon, H. Li, D. V. Shenai, and C. Lavoie, Journal of The Electrochemical Society **157**, H679 (2010).

32 S. K. Dey, J. Goswami, A. Das, W. Cao, M. Floyd, and R. Carpenter, Journal of Applied Physics **94**, 774 (2003).

33 L. M. Apátiga and V. M. Castaño, Thin Solid Films **496**, 576 (2006).

34 Z. G. Xiao, Review of Scientific Instruments **74**, 3879 (2003).

35 M. Ohring, *Materials science of thin films* (Academic press, 2001).

36 R. H. Dauskardt, M. Lane, Q. Ma, and N. Krishna, Engineering Fracture Mechanics **61**, 141 (1998).

37 P. G. Charalambides, H. C. Cao, J. Lund, and A. G. Evans, Mechanics of Materials **8**, 269 (1990).

38 L. J. Chen, *Silicide Technology for Integrated Circuits* (IET (The Institution of Engineering and Technology), 2004).

39 M. P. Moody and J. M. Cairney, *Atom probe microscopy* (Springer, 2012).

40 T. F. Kelly, D. J. Larson, K. Thompson, R. L. Alvis, J. H. Bunton, J. D. Olson, and B. P. Gorman, Annual Review of Materials Research **37**, 681 (2007).

41 B. Gault, M. P. Moody, J. M. Cairney, and S. P. Ringer, Materials Today **15**, 378 (2012).

42 T. F. Kelly and M. K. Miller, Review of Scientific Instruments **78**, 031101 (2007).

43 D. N. Seidman, Annu. Rev. Mater. Res. **37**, 127 (2007).

44 D. N. Seidman and K. Stiller, MRS Bull **34**, 717 (2009).

45 T. F. Kelly and D. J. Larson, Annual Review of Materials Research **42**, 1 (2012).

46 T. F. Kelly, M. K. Miller, K. Rajan, and S. P. Ringer, Microscopy Today **20**, 12 (2012).

Chapter 2 CVD of Cobalt Nitride and its Application as an Adhesion-Enhancing Layer for Advanced Copper Interconnects

Abstract

An interlayer of face centered cubic (fcc) Co_4N has demonstrated significant improvements in adhesion between copper and diffusion barrier layers. This fcc phase of Co_4N was prepared by chemical vapor deposition (CVD) using bis(*N*-*tert*-butyl-*N'*-ethyl-propionamidinato)cobalt(II) and a reactant mixture of NH_3 and H_2 at substrate temperatures from 100 to 180°C. The Co/N atomic ratio and the phase of cobalt nitride film can be modified by adjusting the ratio of NH_3 and H_2 in the gas feedstock. The cobalt nitride films prepared by CVD are smooth, highly conformal, and stable against intermixing with copper up to at least 400°C. This fcc cobalt nitride material has very strong adhesion to copper due to the small lattice mismatch (-1 to 2%) between fcc-Co_4N and fcc Cu. Copper wires should be stabilized against failure by electromigration when fcc cobalt nitride interlayers are placed between the copper and surrounding diffusion barriers.

2.1 Introduction

Cobalt thin films are used widely in the microelectronic industry for numerous applications. applications. Co is used to form $CoSi_2$ by Co/Si interfacial reactions to make source, drain and gate electrodes for complementary metal–oxide–semiconductor (CMOS) structures. Although NiSi offers lower resistivity[1], the greater thermodynamic stability of $CoSi_2$ makes it more suitable for dynamic random-access memory (DRAM) structures where high processing temperatures are required. Cobalt is also a leading candidate for capping copper lines to improve the interconnect reliability against failure by electromigration[2]. It has also been shown that introduction of a thin Co interlayer between Cu and barriers such as TaN,

WN or TiN increased adhesion at the interface, presumably thereby increasing the lifetime of the copper wires.[3] Other applications of Co films include magnetic devices[4] and nano-catalysts for carbon nanotube synthesis[5].

As the feature sizes in integrated circuits shrink to smaller sizes, conventional techniques such as physical vapor deposition (PVD) may not provide adequate step coverage owing to their non-conformal deposition. The problem gets especially challenging for three-dimensional CMOS devices and very narrow copper interconnects. In this chapter, we report the deposition of a novel material, cobalt nitride, using a conformal technique of chemical vapor deposition (CVD). We discuss its potential application as an adhesion-enhancing interlayer for advanced copper interconnects technology.

Copper has successfully replaced aluminum for ultra-large-scale integration (ULSI) because of its low resistivity and superior resistance against electromigration. In the damascene structure, copper is deposited using electroplating due to its low cost, high throughput and via-filling capability. However, the electro-deposition of thick copper is initiated on a pre-existing tri-layer stack which consists of a thin and continuous Cu, an adhesion promoter and a barrier. The current technology utilizes PVD to make Cu (seed)/Ta (adhesion)/TaN (barrier) in the damascene structure. The International Technology Roadmap for Semiconductors (ITRS) projects that as the features shrink, these multilayer stacks have to be thinner and more conformal to maintain effective interconnect resistivity while avoiding any pinholes. It is becoming increasingly challenging for PVD to meet all these requirements and therefore there is a need for a conformal deposition technique such as CVD or atomic layer deposition (ALD). Metal depositions using ALD have slower growth

rates than their CVD counterparts and in most cases, longer deposition leads to rougher morphology due to agglomeration. CVD of Cu has been extensively studied because of its fast deposition rate compared to ALD and its ability to minimize agglomeration in a kinetically driven process[6]. However, CVD Cu is known to exhibit weak adhesion to Ta-based adhesion/barrier layers due to the formation of Ta oxide or Ta fluoride during the CVD process[7]. Ta's high affinity to oxygen and fluorine can extract these elements from a copper precursor during the CVD process. Trace amounts of oxygen or oxygen-containing impurities in the carrier gas can also oxidize the tantalum surface. The presence of an oxide or fluoride layer on Ta facilitates electromigration at the copper/oxide interface, because of the weaker adhesion. Cu can now be deposited by ALD[8] or CVD[9] from precursors that contain neither oxygen nor fluorine, thus providing a possible way to provide strong adhesion of CVD Cu to Ta. However, at present, there is no way to deposit conformal tantalum layers, either by CVD or by ALD. Thus alternative materials for adhesion layers have been sought.

Various studies have been conducted to examine different metals such as Ru[10, 11], Pd[12], Pt[13], Rh[13], Ir[14], Ag[15], Os[16] or Co[17] as possible candidates for an adhesion layer to replace Ta. These more noble metals bind oxygen and fluorine less strongly than Ta does, so they are expected to adhere better to CVD Cu than Ta does. Recently Ru has received much attention and has been widely studied[11]. Ru is a stable metal with low resistivity (7.4 μΩ·cm) and strong adhesion to Cu, but Ru is expensive and in short supply, making it a poor choice for large-scale use.

There are reports suggesting that the adhesion energy at the interface between two metals is larger if their lattices match in size and structure[11, 18, 19]. Hoon *et al.*[18] have demonstrated that a smaller lattice mismatch of Cu with Ru compared to with Ta leads to a lower interface energy and enhanced adhesion of Cu onto Ru. According to this mismatch principle, the strongest adhesion to copper should be found for a metal with the same face-centered cubic (fcc) structure and the same lattice constant as copper. The lattice misfits between Cu and Co, Co_4N and Ru are summarized in Table 2.1, which suggests that Co_4N has cobalt atoms arranged in the same fcc structure as Cu and with almost exactly the same lattice constant (mismatch only -0.8%). Therefore, Co_4N should have a strong adhesion to copper.

Table 2.1. Percentage difference between the lattice constants of copper and of various metals. For the hcp metals, alignment of the hexagonal axis (002) with the Cu(111) axis is assumed. (All the lattice constant values are quoted from Powder Diffraction File (PDF) from ICDD (International Centre for Diffraction Data))

Candidate material	Structure type	Lattice mismatch with Cu	Lattice constant (Å)
Cu	fcc	0 %	a=b=c=3.615
Co_4N	fcc	-0.8 %	a=b=c=3.586
α-Co	fcc	-1.9 %	a=b=c=3.545
ε-Co	hcp	-2.0 %	a=b=2.506, c=4.069
Ru	hcp	+5.9%	a=b=2.706, c=4.282

In this chapter we demonstrate successful CVD of cobalt nitride as an interlayer between CVD WN (barrier) and CVD Cu (seed), all of which is performed in a single CVD reactor without breaking the vacuum. The cobalt nitride exhibits the fcc Co_4N structure that closely matches the Cu lattice and hence demonstrates the expected strong adhesion to CVD copper grown on top of it. Strong adhesion is preserved during CVD also because the

copper precursor contains no oxygen or fluorine that could contaminate the surface of the Co_4N. During the CVD processes of various layers the carbon and hydrogen that accompany the metalorganic precursors are completely removed as vapor byproducts resulting in pure films. The CVD Cu grows epitaxially on all orientations of the polycrystalline Co_4N grains, as shown by high-resolution transmission electron microscopy (TEM). Such a CVD cobalt nitride can also be used to make conformal $CoSi_2$[20].

2.2 Experimental Section – CVD of Cobalt Nitride

The chemical vapor deposition of Co_xN was carried out in a hot wall, tube-furnace reactor. The schematic of the CVD system is as shown in Figure 2.1. The substrate holder is a half cylinder made of aluminum which was inserted into a stainless steel reactor tube. A cartridge heater and a thermocouple (not shown) are embedded in the substrate holder in order to heat the substrate to a temperature higher than the reactor wall by 10-20 °C. This arrangement favors deposition of desired film on the substrate rather than the wall and is suitable for a CVD process with a thermally activated rate. The reactor pressure during deposition was controlled automatically by a throttle valve (MKS Instruments) located downstream to the substrate holder. The metal precursors were loaded in U-shaped bubblers and ultra-high purity N_2 was used as a carrier gas. The bubblers and their associated gas lines were plumbed inside ovens with suitable temperature set points for efficient vaporization and delivery of precursor vapors to the reactor tube. The gas flow rates were established using metal-sealed mass flow controllers (MKS Instruments).

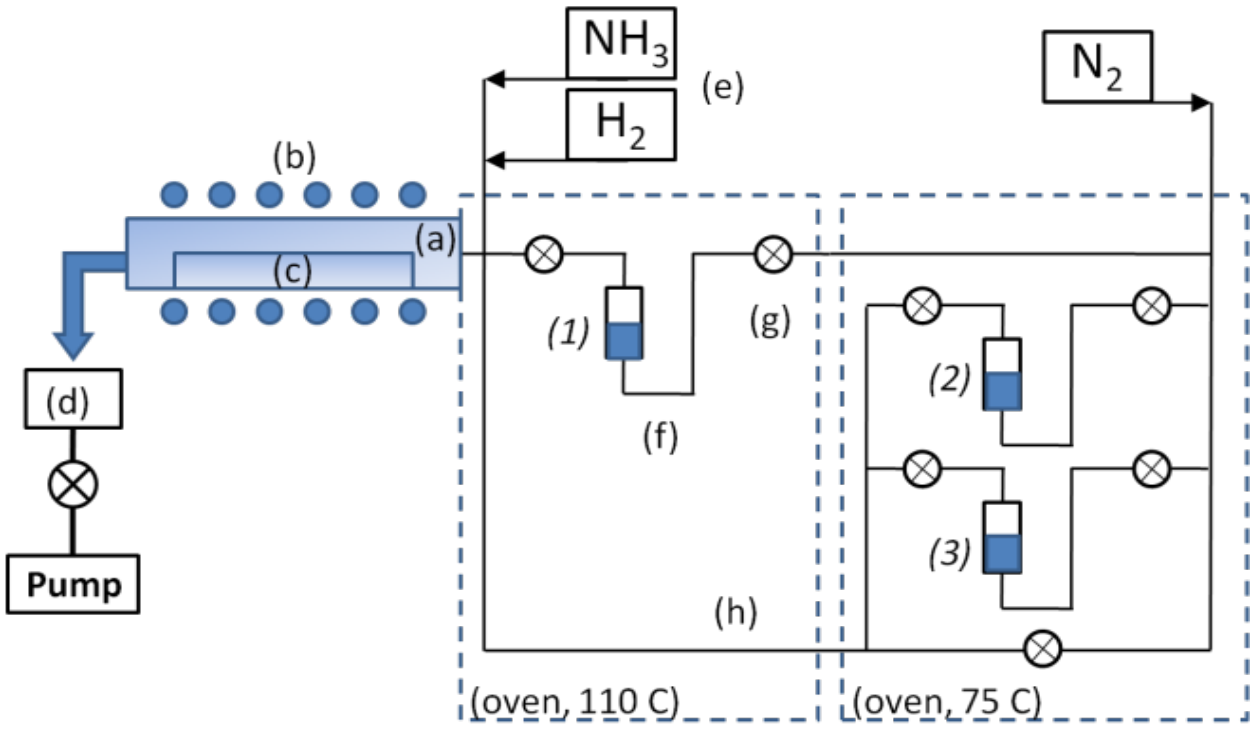

Figure 2.1. Schematic diagram of the CVD system. (a) deposition chamber; (b) furnace; (c) substrate holder; (d) throttle valve; (e) mass flow controllers; (f) bubbler; (g) pneumatically controlled valves; (h) bypass gas line; Precursors: (1) Cu precursor; (2) Co precursor; (3) W precursor.

CVD of Co_xN was carried out from bis(*N-tert*-butyl-*N'*-ethyl-propionamidinato)cobalt(II), $Co[^tBuNC(Et)NEt]_2$, precursor. The synthesis of $Co[^tBuNC(Et)NEt]_2$ has been described elsewhere[21]. This Co precursor is a dark green liquid at room temperature with melting point of -17 °C. The vapor pressure of this precursor may be approximated by $\log_{10}(P, \text{torr}) = 5.424 - 2151/T$, giving 0.14 torr at 70 °C and 0.26 torr at 85°C. Within this temperature range, the evaporation rate is about 0.1 $nmol \cdot min^{-1} \cdot cm^{-2}$ of liquid surface, as measured by isothermal thermogravimetric analysis (TGA). No decomposition was noted when bubblers were used in this temperature range over a period of several months. TGA with a linear temperature ramp of 10 K min^{-1}showed clean evaporation with no residue up to 200 °C, by which temperature the liquid had completely evaporated[21]. This result showed that no

significant decomposition occurs within time periods of minutes even at temperatures as high as 200 °C.

Another test of thermal stability was done by heating the neat liquid in contact with various surfaces: glass (presumably with little or no surface catalytic activity); oxidized stainless steel (to mimic a typical bubbler surface); and stainless steel from which the native oxide had been removed by acid etching. The viscosity of the precursor was also measured with flow tubes inside a glove box, in order to protect it from oxidation. Accelerated rate calorimetry (ARC) testing involves heating a closed sample at a series of increasing temperatures 10 K apart, with a dwell time of 50 minutes at each temperature. During this heating the pressure was measured to see if any gases are being generated by decomposition. If a significant pressure rise is detected, the dwell time is lengthened to see if the pressure rise is transient or if a self-sustained exotherm occurs.

Table 2.2. CVD conditions explored in this work.

CVD Parameters	Cobalt Nitride
Temperature	100-180 °C
Pressure	1-5 torr
Co source temperature	70-85 °C
N_2 carrier gas	60 sccm
Reactant Gas (NH_3+H_2)	60+0, 40+20, 20+40, 10+50, 0+60 sccm

The ranges of CVD conditions in which Co_xN films were deposited are shown in Table 2.2. NH_3 gas was used as the nitrogen source and H_2 as the reducing agent. Although the ratio of NH_3 to H_2 gas flow was varied, the total flow rate of the mixture was always maintained at 60 sccm. 60 sccm of N_2 carrier gas passed through the bubbler to carry the precursor vapor into the deposition chamber. We assumed that an equilibrium vapor pressure of the Co

precursor was achieved while the N_2 bubbled up through about 10 cm of the liquid. A total pressure drop of 6.3 torr was estimated between the bubbler and the reactor tube, most of it arising from the pressures required to open the three spring-loaded check valves installed downstream to the bubbler. The check valves (not shown in Figure 2.1.) were used to separate multiple precursors installed in two ovens and to avoid back flow of vapor to cooler parts of the system. The high total pressure in the bubbler reduces the partial pressure of the precursors in the reactor, thereby limiting the overall growth rate and the step coverage inside features with high-aspect ratios. The estimated partial pressures for the reacting species are presented in Table 2.3.

Table 2.3. The effect of pressure drop in check valves in limiting the partial pressure of the Co precursor in the reactor.

Reactor Design	With 3 check valves	With 1 check valve
Substrate temperature	180 °C	
Reactor wall temperature	160 °C	
Reactor Pressure	1 torr	
Co Precursor bubbler temp. (P = 261 mtorr)	85 °C	
N_2 carrier gas	60 sccm	
Reactant Gas (NH_3+H_2)	20+40 sccm	
Pressure Drop	6.3 torr	2.1 torr
Bubbler Pressure	7.3 torr	3.1 torr
Partial Pressures		
P_{N2}	0.49 torr	0.48 torr
P_{NH3}	0.16 torr	0.16 torr
P_{H2}	0.33 torr	0.32 torr
P_{Co} precursor	0.02 torr	0.04 torr
Step Coverage	<10:1	>30:1
Growth Rate (on SiO_2 and WN)	~0.5 nm/min	~1 nm/min

CVD WN was deposited from bis(*tert*-butylimido)bis(dimethylamido)tungsten(VI) vaporized from a bubbler at 85 °C and NH_3 gas. The deposition conditions for WN were 390 °C substrate temperature and 1 torr total pressure. The N_2 carrier gas and NH_3 flow rates were both set at 20 sccm. Cu metal or CuON was deposited from (*N,N'*-di-*sec*-butylacetamidinato)copper (I). For Cu deposition, 40 sccm of H_2 was used as the reducing agent and 40 sccm of N_2 was bubbled through the molten precursor at 95 °C. The Cu deposition was carried out at 180 °C and 1 torr total pressure. An alternate route adopted to make smoother Cu films was to deposit CuON and reduce it after deposition at room temperature by hydrogen plasma. This process is discussed in detail elsewhere[6]. Multilayer films were deposited without air break in order to prevent any oxidation of the films.

Substrates used in these experiments were 300 nm of thermally oxidized SiO_2 supported on Si wafers. Before deposition, the substrates were exposed to a mercury UV lamp in air for 10 min to remove any organic contamination. The substrates were then dipped briefly in 5% HF solution and rinsed in distilled water to expose fresh oxide surface by etching 20-30 nm of SiO_2.

The surface morphologies of the films were characterized by an atomic force microscope (AFM, Asylum MFP-3D). The thicknesses of smoother films were measured by x-ray reflection (XRR, Scintag XDS 2000). For metals with rough surfaces, the films were patterned into stripes using photolithography and etching techniques, and the resulting thickness profiles were measured using AFM. The film composition and density were measured using 2 MeV He^+ Rutherford backscattering spectroscopy (RBS). The areal density of individual elements was determined by using a reference of Harwell Bi

standard[22] and by using a glassy carbon substrate. The phases of as-deposited films were evaluated by electron diffraction in a transmission electron microscope (JEOL, JEL2010), using as substrates a 50nm thick silicon nitride membrane suspended in a 3mm Si wafer (TEM grid, Ted Pella). Cross-section electron imaging of thin films was carried using TEM (JEOL 2100) and SEM (Zeiss Supra55VP) to study epitaxy and step coverage, respectively, of as-deposited thin films. The sheet resistance was measured by a four point probe station (Miller Design & Equipment, FPP-500). The atomic concentrations of elements were analyzed by x-ray photoelectron spectroscopy (XPS, ESCA SSX-100). The interfacial adhesion energies were evaluated by the four-point bend test, as described elsewhere[23].

2.3 Results and Discussion

2.4 Properties of the Liquid Cobalt Precursor

Some additional properties of the cobalt precursor were measured. The viscosity as a function of temperature is given by ln μ(cP) = 3365.5/T(K) – 8.1694 and plotted in Figure 2.2. Within the range of bubbler temperatures used, 70 to 85 °C, the viscosity is low, just 3 to 5 times that of water. Thus bubbling is not impeded by the viscosity of this precursor.

Heating the neat precursor at 120 °C in contact with glass, etched stainless steel or oxidized stainless steel for 60 hours did not generate any diamagnetic decomposition products in the NMR spectrum, indicating that thermal stability is not compromised by contact with these surfaces. An ARC test of stability was carried out. Slow, non-sustaining, transient exotherms were observed at 180, 210, and 219 °C. This test shows that little or no decomposition takes place at temperatures below 180°C over periods of hours. These thermal stability tests have important implications for the vaporization of this cobalt

precursor in a direct liquid injection (DLI) system[24]. In such a system, vaporization takes place within seconds, so that temperatures up to about 180 °C could be used without significant decomposition of the precursor. Thus much higher vapor pressures can be produced in a DLI system than in a traditional bubbler. Much higher precursor partial pressures translates into the ability to coat much narrower features conformally[25].

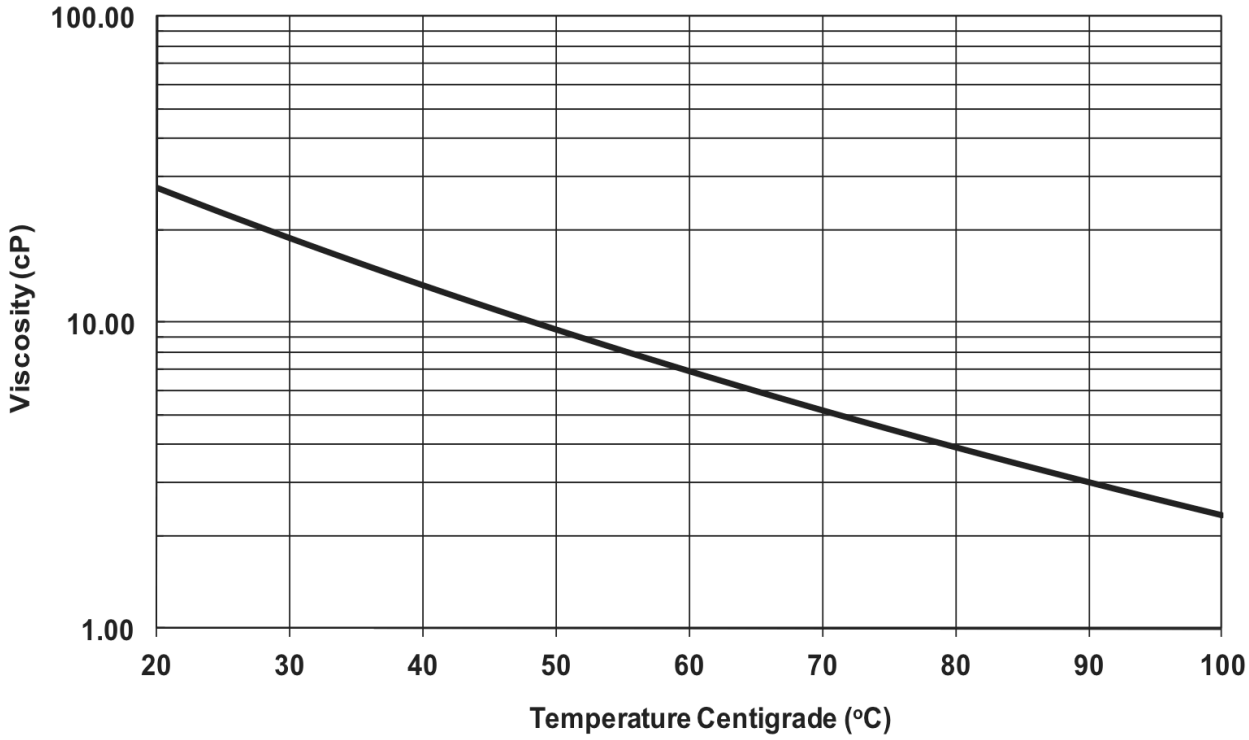

Figure2.2. Viscosity of the cobalt precursor as a function of temperature.

2.4.1 Chemical Vapor Deposition of Co_xN

Co_xN films were deposited without an air-break on freshly-deposited WN in order to increase the adhesion energy of the films to substrates. Table 2.4 shows RBS data for the composition of Co_xN films deposited at 180 °C with various feed rates of NH_3 and H_2. The area density of nitrogen atoms in Co_xN was found by subtracting the area density of N in control samples of WN from the total number of N atoms per unit area detected by RBS in

Co_xN/WN/C. It is clear that N was incorporated into the as-deposited films only when NH_3 was introduced, irrespective of its flow rate. All of the films show metallic conduction, with resistivity increasing with nitrogen content.

Table 2.4. Composition of cobalt nitride films by RBS, the corresponding crystal phase, and the electrical resistivity.

NH_3 (sccm)	H_2(sccm)	Co_xN_y	Phase	Resistivity (μΩ·cm)
60	0	x=2.3, y=1.0	Co_3N, hcp	~180
40	20	x=3.8, y=1.0	Co_4N, fcc	~100
20	40	x=4.4, y=1.0	Co_4N, fcc	~100
10	50	x=6.9, y=1.0	Co_4N, fcc	~100

When Co_xN was deposited with just NH_3 and no H_2 gas, a composition $Co_{2.3}N$ was obtained. Figure 2.3 shows an electron diffraction pattern for a $Co_{2.3}N$ film that corresponds to a Co_3N phase with a hexagonal close packed (hcp) structure. The phase that resulted from NH_3 alone as a co-reactant is the hcp (Co_3N) phase.

When H_2 was introduced along with NH_3 in different proportions, while maintaining the total flow rate of the two gases at 60 sccm, the as-deposited Co_xN films became richer in cobalt (x>2.3). Co precursor and H_2 gas alone (no NH_3) showed no reactivity at 180°C because no film growth was detected at that temperature. Thus H_2 acts as a reducing agent during some stage of the reaction of the Co precursor with NH_3 at 180 ˚C even though it shows no direct reactivity with the Co precursor itself. The Co/N atomic ratio increases as the H_2/NH_3 feed-ratio is increased.

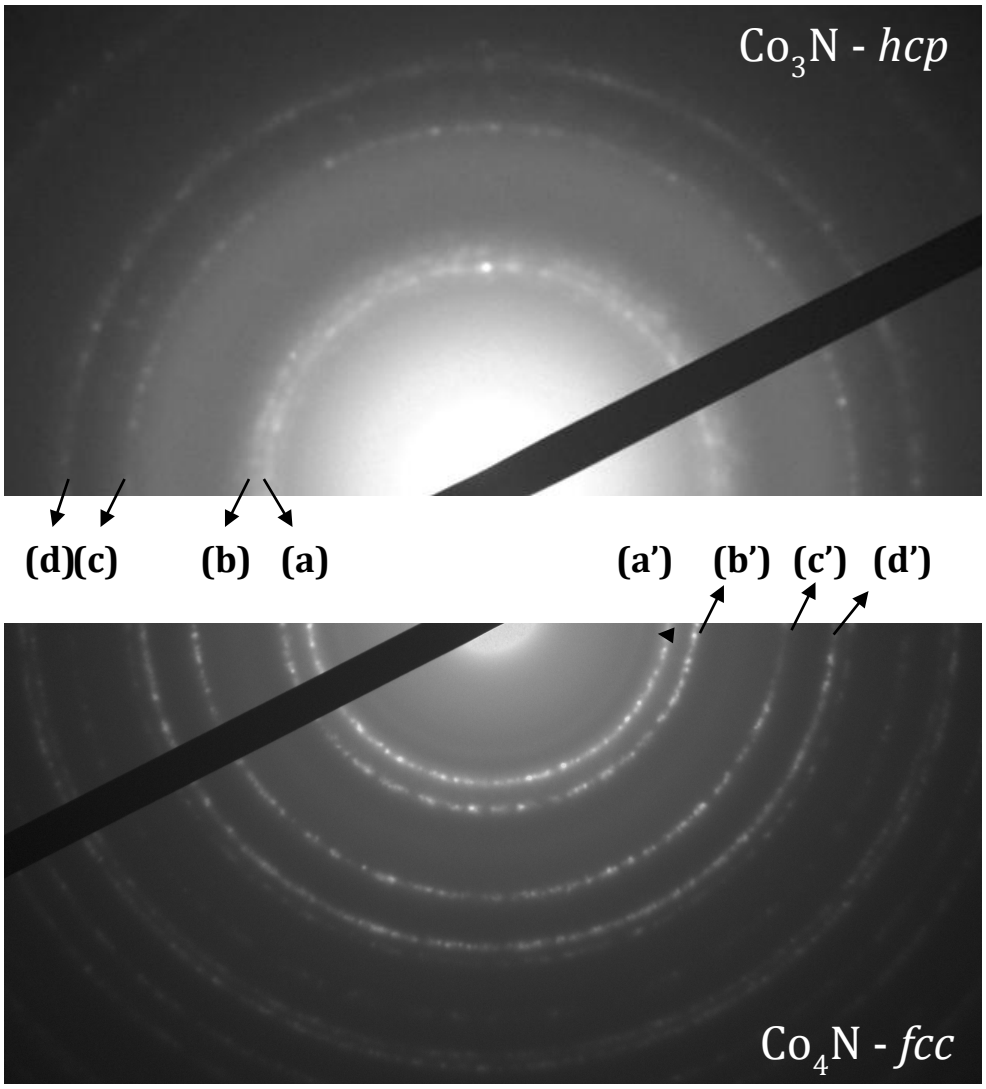

Figure 2.3. Electron diffraction patterns of polycrystalline Co_3N (a) <002>, (b) <101>, (c) <103>, (d) <201> and Co_4N (a') <111>, (b') <200>, (c') <220>, (d') <311>.

These cobalt-rich films exhibit a fcc structure as shown in figure 2.3 for the NH_3/H_2 = 20/40 sccm condition. A fcc Co_4N phase has been reported by other groups [26, 27] using sputtering. This is the first report of Co_4N material with the fcc phase prepared using CVD. The crystal geometry of the Co_4N phase can be considered to be made of Co atoms placed in a fcc lattice and a nitrogen atom trapped interstitially in the center of a unit cell. As a result, the introduction of N atoms should show expansion from the fcc Co lattice (a=3.545Å).

Theoretical studies of the Co_4N phase [27] have shown that lattice expands as a function of interstitial nitrogen trapped per unit cell. Therefore it might be possible to adjust the lattice parameter of Co_4N experimentally by controlling the amount of nitrogen in the film. The polycrystalline Co_4N films have a relatively smooth morphology even when deposited on SiO_2 without WN underneath. The AFM image shown in Figure 2.4 for a 20 nm Co_4N film has a root-mean-square (RMS) surface roughness of 1.3 nm. In comparison, CVD Co films of the same thickness 20nm deposited at a higher temperature (240 °C) with H_2 as the only co-reactant are rougher (RMS roughness = 2.7 nm).

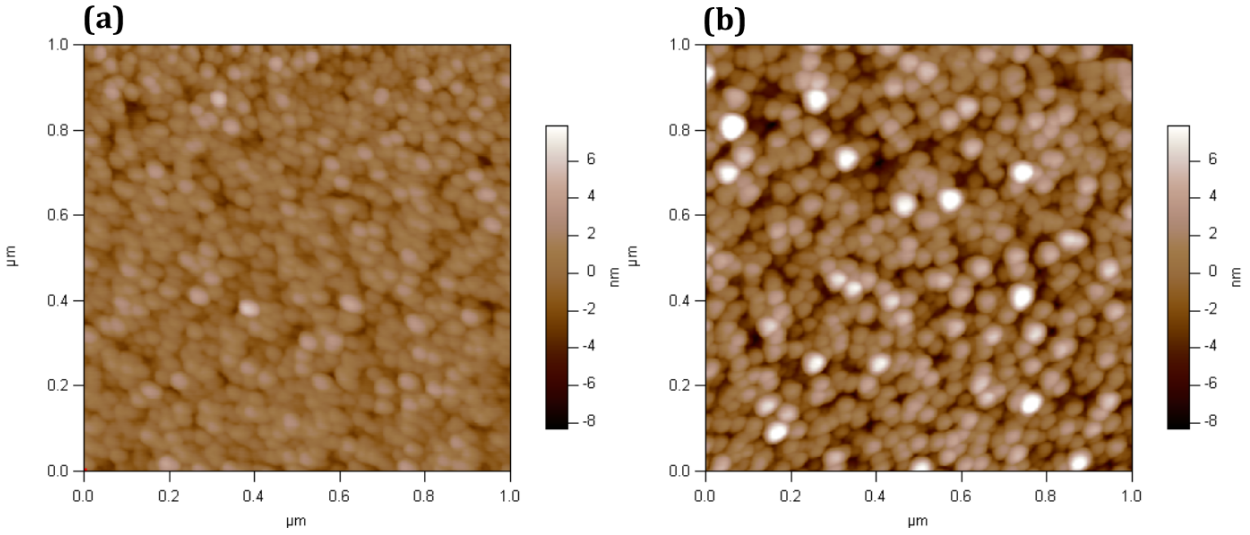

Figure 2.4. AFM images of (a) an Co_4N film 20 nm thick, RMS roughness = 1.3 nm; (b) a Co film 20 nm thick, RMS roughness 2.7 nm.

2.4.2 Hetero-Epitaxial Relation Between Co_4N and Cu

During the processing of copper interconnects, it is critical for Cu to adhere strongly to the underlying barrier material. The minimum adhesion energy recommended between Cu and the barrier material in order to survive the chemical mechanical planarization (CMP) is 5

$J \cdot m^{-2}$ [28]. Amorphous WN is a well-studied barrier material for copper interconnects application but exhibits poor adhesion with CVD copper (< 2 $J \cdot m^{-2}$)[3]. In order to improve adhesion between Cu and WN, an interlayer of Co_4N was tested. A stack of CVD Cu/Co_4N/WN was deposited on SiO_2/Si without breaking the vacuum. Figure 2.5 shows the TEM cross section of the as-deposited film stack with sharp interfaces between the film stacks. The four-point bend test evaluation of the stack revealed adhesion energy of 10-13 $J \cdot m^{-2}$ between Cu and Co_4N, which is stronger than the reported adhesion energy 6$J \cdot m^{-2}$ of Ru glue layer[11] .

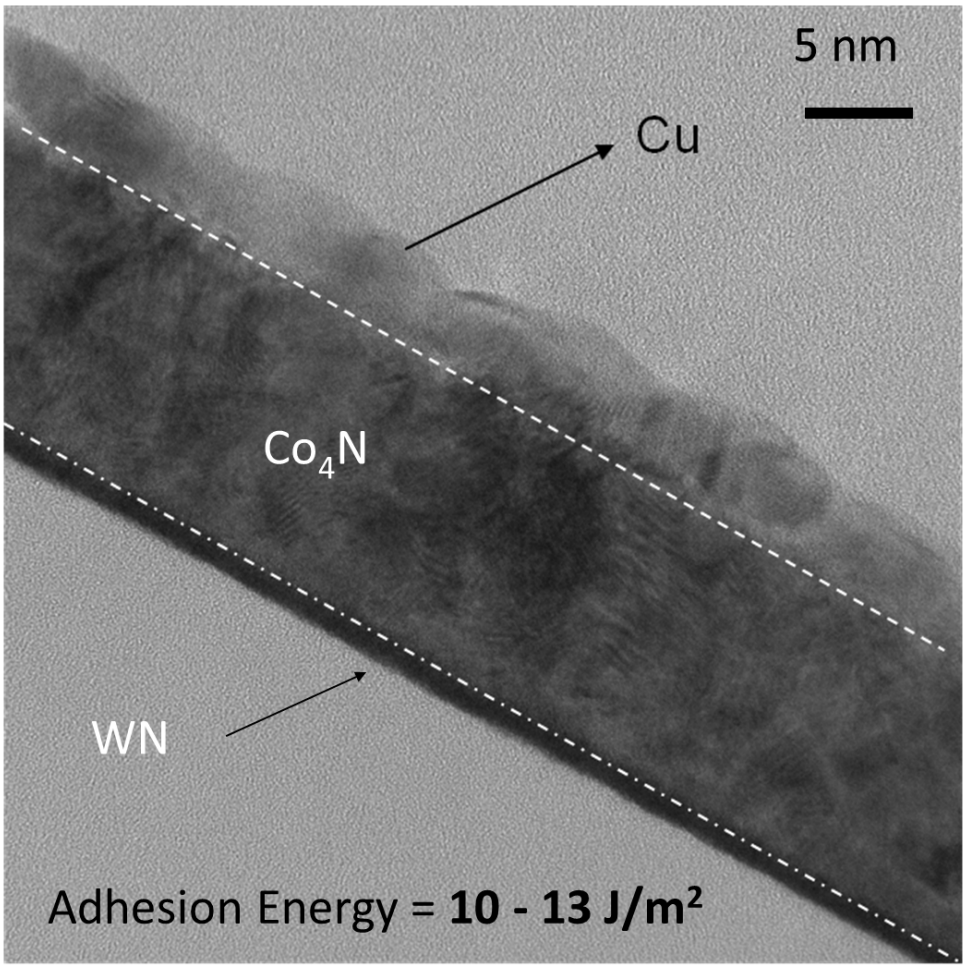

Figure 2.5. Cross-sectional TEM of SiO_2/WN/Co_4N/Cu.

The high resolution TEM image (Figure 2.6) shows that Cu grew epitaxially on the Co_4N. The lattice spacing seen in figure 2.6 matches the <111> planes. The hetero-epitaxial relation between the two poly-crystalline metals was discontinuous along the interface but was sufficient to promote strong adhesion.

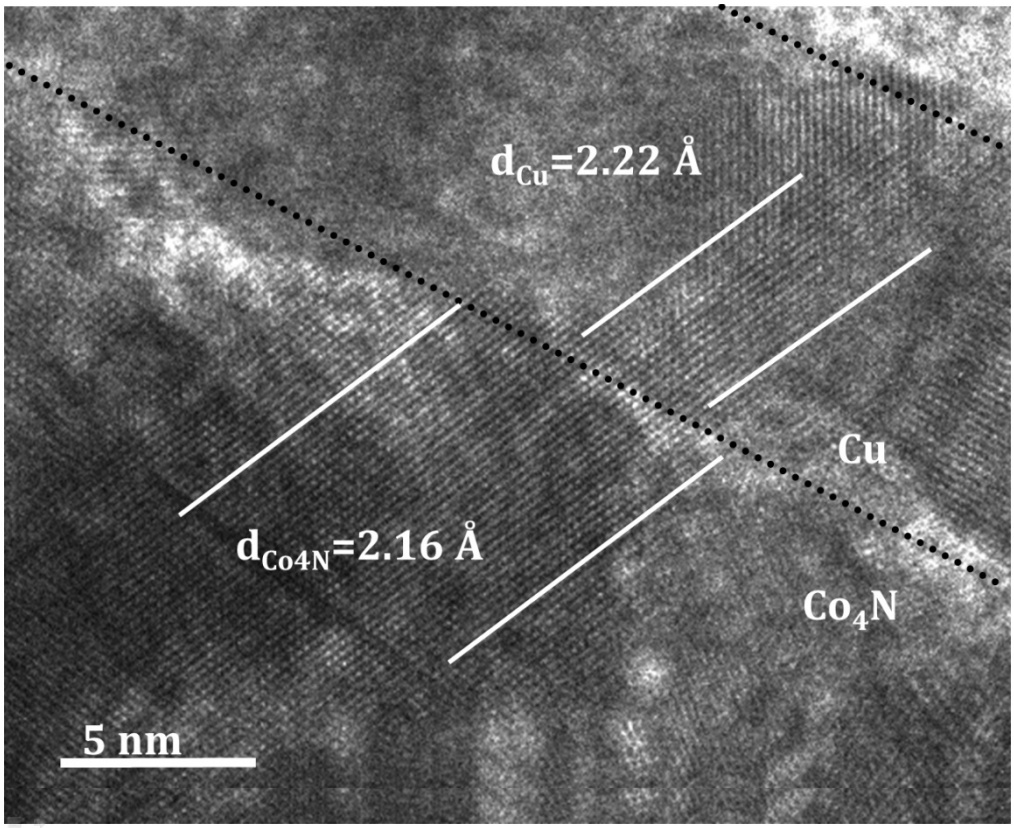

Figure 2.6. High-resolution cross-sectional TEM of the Co_4N/Cu interface showing the epitaxial relation between the materials.

The lattice parameters of Co_4N films with different amounts of nitrogen were evaluated by carrying out selected area electron diffraction (SAD) on thin films deposited on Si_3N_4 TEM grids. Measurement of absolute lattice parameters from SAD diffraction patterns involved careful elimination of the instrumental errors. Cu was deposited on top of Co_4N film to form a Cu/Co_4N stack, where the lattice parameter of Cu (a= 3.615Å) served as an internal

standard. For comparison, copper was also deposited directly on the TEM grids. Figure2.7 shows the comparison of diffraction patterns from Cu/Co_4N stack, Cu and Co_4N on TEM grids. The diffraction pattern on all three samples show three major rings that correspond to the<111>, <200>, <220> and <311> planes of fcc lattice. It is especially convincing that the diffraction signals from the bi-layer stack of Co_4N and Cu closely overlap with each other. This re-confirms the close match between the Cu and Co_4N lattice parameters, because both films are exactly the same distance from the detector. The only diffraction ring that does not show any overlap is that of the Cu_2O along with the Cu sample, resulting from surface oxidation of copper. The diffraction rings from the Cu/Co_4N film stack were carefully resolved to measure the lattice parameter of Co_4N using Cu as the internal standard. The resulting lattice parameters of the Co_4N are 1 to 2 % smaller than Cu, as expected from the literature values of the lattice constants of bulk single crystals. The precision of these values was not high enough to resolve any variation of the lattice constant of Co_4N with variations in the nitrogen content.

Cu/Co_4N bilayers were also deposited on thin Si_3N_4 TEM grids. Plane-view TEM pictures this film stack in Figure2.8 (a) show the grain size and nucleation density of copper on Co_4N. For comparison, Figure 2.8 (b) shows a CVD Cu film grown under the same conditions on a thin Co layer. The Cu grains are larger on the Co_4N substrate than on the Co substrate. Larger grains should translate into higher electrical conductivity.

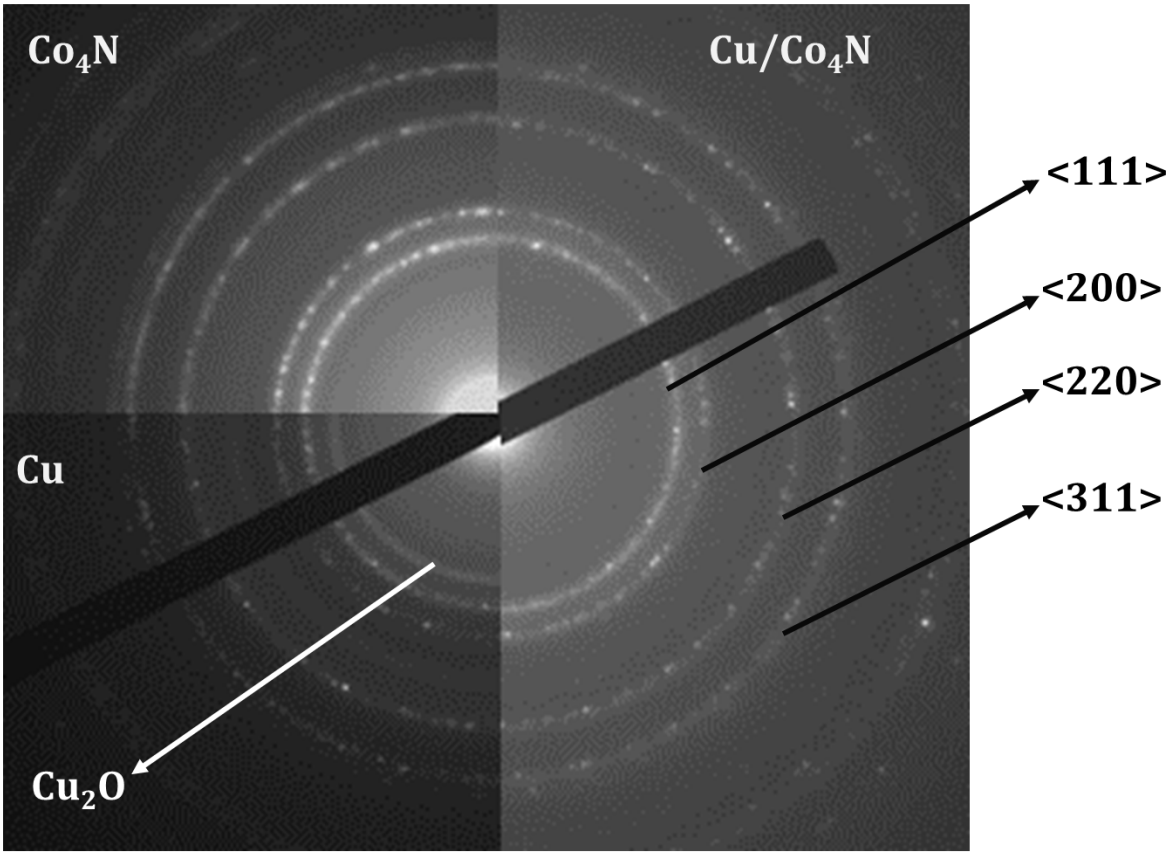

Figure 2.7. Electron diffraction patterns of a single layer of Co_4N (upper left), a bilayer film of Cu/Co_4N (right side), and an oxidized Cu film (lower left).

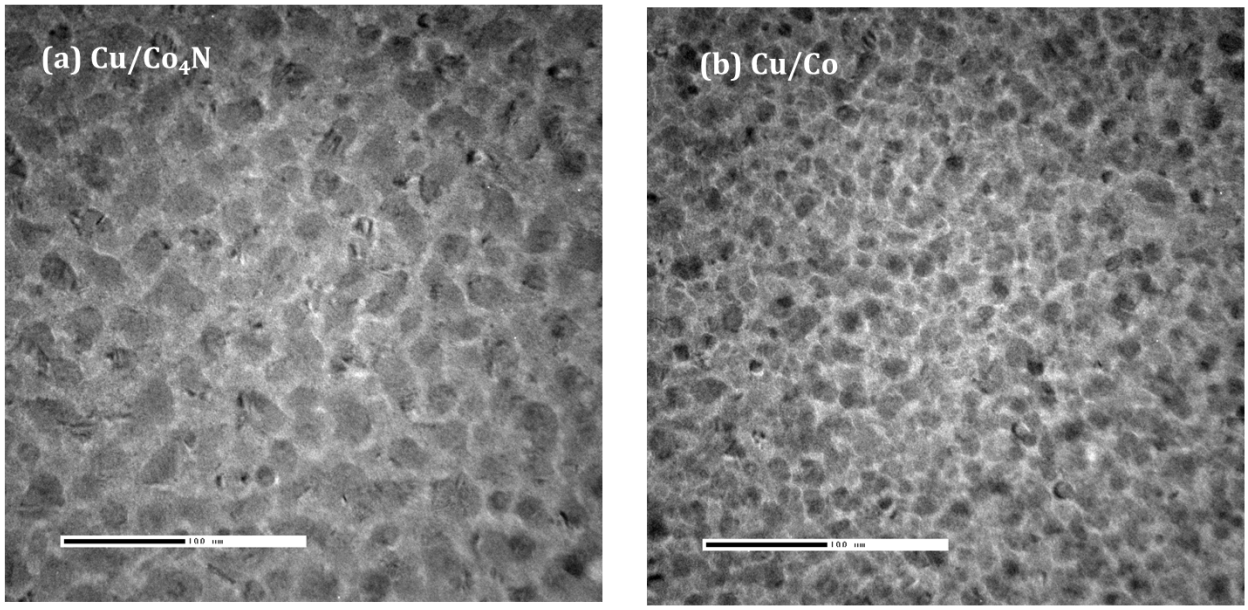

Figure 2.8. Comparison of Cu nucleation on (a) Co_4N and (b) Co (Average copper grain size on cobalt is ~19nm, whereas the grain size on Co_4N is 38nm). The scale bar in the figure corresponds to 100nm.

2.4.3 Thermal Stability of Cu/Co_4N Structure

The thermal stability of the interface between Co_4N and Cu is crucial in keeping the resistivity of the Cu wires low. The thermal stability can be determined by annealing a stack containing the interface. A stack of Cu/Co_4N/WN was deposited on SiO_2/Si using CVD. A 90 nm thick Cu was sputtered on top of the 10 nm Cu to avoid agglomeration of free surface of Cu. The stack was then annealed in forming gas (N_2/H_2: 95/5 vol %) for 30 min at 400 °C. The sheet resistances of the film before and after the annealing step were 0.33 ohm/sq and 0.28 ohm/sq, respectively. Post-annealing of this PVD Cu/ CVD Cu/Co_4N/WN stack in N_2 for 30 min at 400°C showed a decrease in the sheet resistance as well. The sheet resistances of the film stack before and after the annealing were 0.33 ohm/sq and 0.27 ohm/sq. The sheet resistance of the Cu would have increased sharply if there were any migration of Co, N or Co-N species into the bulk of Cu. The lowering of the sheet resistance indicates re-crystallization of Cu, and an overall stability of the Co_4N and Cu interface.

2.4.4 Step Coverage of Co_4N

The step coverage of CVD Co_4N was tested by depositing film on a silicon substrate with holes having an aspect ratio of 30:1 with a diameter 336 nm. The CVD conditions tested are tabulated in Table 2.3. In the initial design of the system, there were 3 check valves between the cobalt bubbler and the reactor tube. The Co_4N deposition with three check valves in the system had low step coverage, less than 10:1. After removal of two check valves, it is found that step coverage of 30:1 is achieved for 20% reduction in film thickness on the bottom of the hole (~23.5 nm) compared with the top of the hole (~30 nm). The step coverage tends to be poor when the CVD reaction is operating in transport-limited conditions of low partial pressure of the precursor inside the reactor and high surface

reaction rate. Table 2.3 presents the partial pressures of different gases before and after removal of check valves. After the removal of two check valves, the partial pressure of cobalt precursor is 0.04 torr compared to 0.02 torr before the system optimization. The growth rate of the cobalt nitride film increased to 1nm/min from 0.5nm/min. Figure 2.9 shows an SEM image of nearly conformal deposition of Co_4N down to an aspect ratio of 30:1 in a hole. The overall step coverage can be improved by eliminating the back pressure from the check valves, increasing the vaporization temperature of the Co bubbler or by using DLI to make higher partial pressures of the precursor vapor[25].

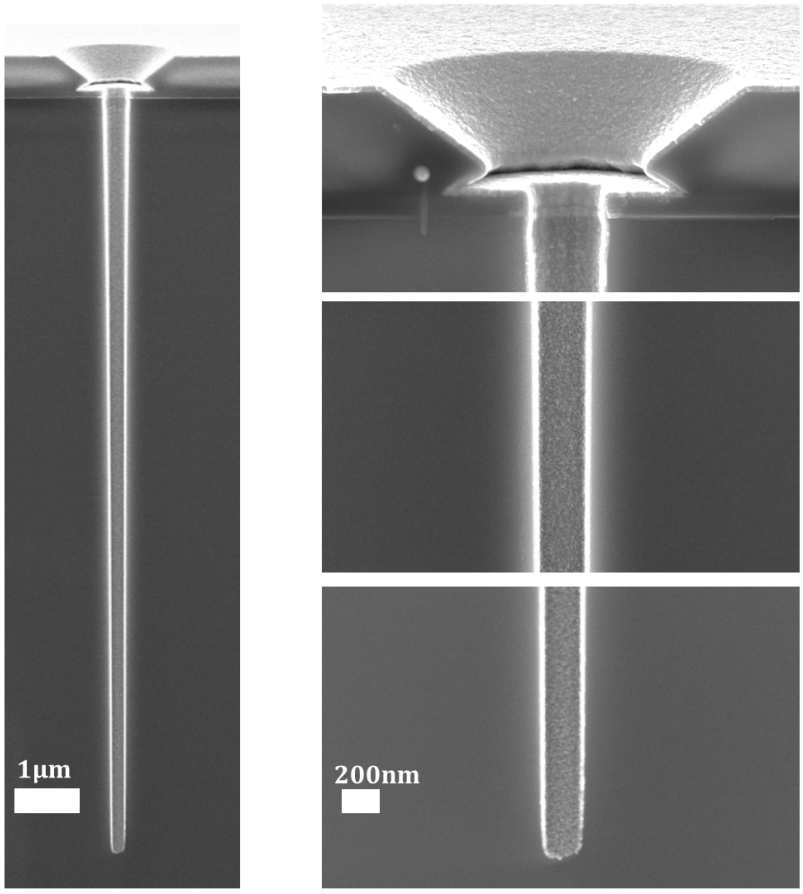

Figure 2.9. Cross-sectional SEM of a Co_4N film inside a narrow hole with an aspect ratio of about 30:1.

2.5 Conclusions

In this chapter we report synthesis of smooth, continuous and conformal Co_4N thin films using a cobalt amidinate, $Co[Bu^tNC(Et)NEt]_2$, as the cobalt source and a combination of NH_3 and H_2 gases. Although H_2 shows no reactivity with the Co precursor at 180 °C, it stabilizes Co_4N into a face centered cubic structure in the presence of NH_3 feed. In the absence of H_2, the reaction between Co precursor and NH_3 yields the Co_3N phase, which has a hexagonal close packed structure. The fcc structure of the Co_4N phase exhibits low (-1%) mismatch with that of Cu and therefore shows a strong bonding (adhesion energy: 10-13 Joules m^{-2}) at the Co_4N/Cu interface. The stability of the interface was tested up to 400 °C with no evidence of intermixing. Thus Co_4N, which has a fcc structure, is a good choice for an adhesion-promoting under-layer for conformal methods of forming the Cu seed layers for advanced copper interconnects.

2.6 References

1 Z. Li, R. G. Gordon, H. Li, D. V. Shenai, and C. Lavoie, Journal of The Electrochemical Society 157, H679 (2010).

2 H. Nakano, T. Itabashi, and H. Akahoshi, Journal of The Electrochemical Society 152, C163 (2005).

3 Z. Li, R. G. Gordon, D. B. Farmer, Y. Lin, and J. Vlassak, Electrochemical and Solid-State Letters 8, G182 (2005).

4 M. Kisielewski, A. Maziewski, M. Tekielak, A. Wawro, and L. T. Baczewski, Physical Review Letters 89, 087203 (2002).

5 N. Li, X. Wang, S. Derrouiche, G. L. Haller, and L. D. Pfefferle, ACS Nano 4, 1759 (2010).

6 H. Kim, H. B. Bhandari, S. Xu, and R. G. Gordon, Journal of The Electrochemical Society 155, H496 (2008).

7 S. Gandikota, S. Voss, R. Tao, A. Duboust, D. Cong, L.-Y. Chen, S. Ramaswami, and D. Carl, Microelectronic Engineering 50, 547 (2000).

8 Z. Li, A. Rahtu, and R. G. Gordon, J. Electrochem. Soc. 153, C787 (2006).

9 Y. Au, Y. Lin, and R. G. Gordon, J. Electrochem. Soc. 158, D248 (2011).

10 O.-K. Kwon, S.-H. Kwon, H.-S. Park, and S.-W. Kang, Journal of The Electrochemical Society 151, C753 (2004).

11 M. Damayanti, T. Sritharan, Z. H. Gan, S. G. Mhaisalkar, N. Jiang, and L. Chan, Journal of The Electrochemical Society 153, J41 (2006).

12 S.-E. Nam and K.-H. Lee, Journal of Membrane Science 192, 177 (2001).

13 M. Lane, C. Murray, F. McFeely, P. Vereecken, and R. Rosenberg, Applied Physics Letters 83, 2330 (2003).

14 D. Josell, J. E. Bonevich, T. P. Moffat, T. Aaltonen, M. Ritala, and M. Leskela, Electrochemical and Solid-State Letters 9, C48 (2006).

15 A. E. Kaloyeros and E. Eisenbraun, Annual Review of Materials Science 30, 363 (2000).

16 D. Josell, C. Witt, and T. P. Moffat, Electrochemical and Solid-State Letters 9, C41 (2006).

17 Z. Li, R. G. Gordon, D. B. Farmer, Y. Lin, and J. Vlassak, Electrochem. Solid-State Lett. 8, G182 (2005).

18 H. Kim, T. Koseki, T. Ohba, T. Ohta, Y. Kojima, H. Sato, and Y. Shimogaki, Journal of The Electrochemical Society 152, G594 (2005).

19 S. Q. Wang and H. Q. Ye, Current Opinion in Solid State and Materials Science 10, 26 (2006).

20 Q. M. Wang, J.-S. Lehn, H. Li, D. Shenai, J. Yang, and R. Gordon, Proc. AVS Atomic Layer Deposition Conference (2011).

21 Z. Li, D. K. Lee, M. Coulter, L. N. J. Rodriguez, and R. G. Gordon, Dalton Trans., 2592 (2008).

22 J. A. Davies, T. E. Jackman, H. L. Eschbach, W. Dobma, U. Wätjen, and D. Chivers, Nuclear Instruments and Methods in Physics Research Section B: Beam Interactions with Materials and Atoms 15, 238 (1986).

23 J. J. V. Y. Lin, T.Y. Tsui, A.J. McKerro, Materials Research Society Symposia Proceedings 795 (2004).

24 Z. G. Xiao, Rev. Sci. Instrum. 74, 3879 (2003).

25 A. Yanguas-Gil, Y. Yang, N. Kumar, and J. R. Abelson, J. Vac. Sci. Technol. A 27, 1235 (2009).

26 H. Jia, X. Wang, W. Zheng, Y. Chen, and S. Feng, Materials Science and Engineering: B 150, 121 (2008).

27 S. F. Matar, A. Houari, and M. A. Belkhir, Physical Review B 75, 245109 (2007).

28 L. Peters, Semiconductor International (2001).

Chapter 3 Quantitative Evaluation of Cobalt Disilicide/Si interfacial roughness

Abstract

The formation of smooth, conformal cobalt disilicide ($CoSi_2$) without facets or voids is critical for microelectronic device reliability owing to the ultra-shallow contact areas. We fabricated $CoSi_2$ from CVD Co_xN films on Si or SOI substrates by in-situ rapid thermal annealing (RTA) at 700°C. We adapted and applied a novel approach of backside sample preparation to reveal the $CoSi_2$/Si interface for quantitatively evaluation of the interfacial roughness. We produced the $CoSi_2$ on SOI substrates and employed mechanical polishing, anisotropic TMAH wet etching, HF etching, and isotropic XeF_2 dry etching to remove the substrate and expose the $CoSi_2$/Si interface. This method offers a robust and reliable procedure for quantitative assessment of the $CoSi_2$/Si interfacial roughness. Also this provides the analytical support for advanced fabrication process development.

3.1 Introduction

Metal silicides have been widely used as self-aligned contacts in silicon-based microelectronic devices for the past decades[1]. Among various metal silicides, $CoSi_2$ is considered as an attractive contact material because of its low resisitivity (10-20 μΩ·cm), no line-width dependence on the narrow Si line, and its superior chemical and thermal stability[2]. As the size of contact in the transistors becomes smaller and the junction depth becomes shallower, a thin, uniform $CoSi_2$ layer is essential for ultra-shallow junctions. Otherwise, cobalt silicide spikes[3] will cause severe junction leakage and lead to device failure. However, the complicated nature of $CoSi_2$ growth mechanism can result in a problematic, rough $CoSi_2$/Si interface[4 5]. The complex kinetics results from several concurrent mechanisms: nucleation, diffusion and perhaps interface reaction[6]. Many efforts have been focused on the formation of a smooth $CoSi_2$ interface with Si by optimizing

fabrication process. For example, Ti capping layer was introduced to reduce the detrimental impacts of ambient contamination[7]. Hence, the quantitative evaluation of the $CoSi_2$/Si interfacial roughness is crucial for the fabrication process optimization.

$CoSi_2$ is typically fabricated by annealing sputtered Co film on active source, drain and gate regions[2]. However, the conventional sputtering process results in poor step coverage and induces high ion damage in the active regions, making it undesirable for complex 3D architecture in the modern transistor. Alternatively, the chemical vapor deposition (CVD) is capable of producing conformal cobalt-containing thin films without ion-induced damage[8].

In this chapter, we used CVD method which has demonstrated to produce smooth, uniform, highly conformal Co_xN[8]. We successfully converted the Co_xN on Si substrates into $CoSi_2$ by in-situ rapid thermal annealing (RTA) at 700°C. We adapted and modified a backside etching SIMS sample preparation approach[9] to remove the backside of the sample and reveal the $CoSi_2$/Si interface. We applied both wet-etching and dry etching to remove the SOI (silicon on insulator) substrate below the $CoSi_2$. As far as we know, it is the first quantitative evaluation of the silicide/Si interfacial roughness, which offered critical insights for future process optimization.

3.2 Formation of Cobalt Disilicide from CVD Cobalt Nitride

Cobalt nitride films on Si and SOI substrates were prepared by CVD method using bis(N-tert-butyl-N'-ethyl-propionamidinato)cobalt(II) and a mixture of 20 sccm NH_3 and 40 sccm H_2 at 200°C. The details of this process have been described elsewhere[8]. Those Si and SOI substrates were first treated by UV-ozone and then cleaned by HF before the deposition. After cleaning, the substrates were immediately transported into the reactor chamber to

suppress oxidation of the substrates. As Co is unable to react with SiO_2[7], the cobalt silicide formation might be slowed down or even blocked by interfacial native oxide. Therefore, a clean substrate without native oxide is critical to obtain a uniform, smooth $CoSi_2$ films.

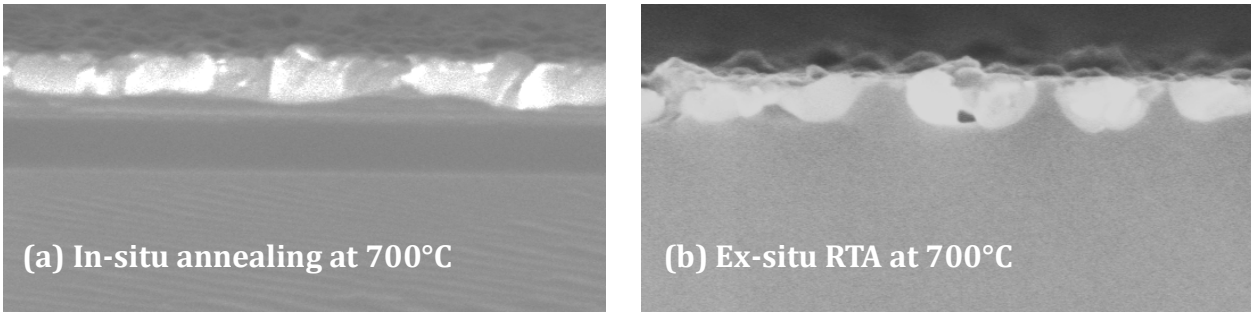

Figure 3.1 $CoSi_2$ formed by annealing Co_xN/Si (a) in-situ in the tube furnace at 700°C in N_2 at 1 Torr for 30sec (Temperature ramp rate: 0.6°C/sec). And $CoSi_2$ formed by (b) (b) ex-situ annealing in the RTA (rapid thermal annealing) tool at 700°C in N_2 (Temperature ramp rate: 100°C/sec).

The as-deposited Co_xN films were treated by in-situ RTA at elevated temperatures from 500°C to 700°C for 30sec in purified N_2. Those gases used in the deposition and annealing processes have been purified by gas purifiers (Entegris Gatekeeper) to control the ambient impurity below 1 ppb of all contaminants including O_2, CO, CO_2, and H_2O. This is because the $CoSi_2$ formation process is highly sensitive to traces of impurities like O_2 and moisture in the annealing ambient[10]. As a result, excellent control of ambient impurities is essential for smooth $CoSi_2$ formation[7]. Indeed, attempts to form $CoSi_2$ from Co_xN by ex-situ RTA were unsuccessful owing to the sample contamination during the exposure to the air and the annealing ambient (the RTA tool does not use purified gas for annealing). Figure 3.1 compared the continuous $CoSi_2$ formed by in-situ annealing in tube furnace with the discontinuous $CoSi_2$ containing voids formed by ex-situ rapid thermal annealing at the same temperature of 700°C. Those impurities caused complication in the silicidation processes and formed discontinuous $CoSi_2$ with many voids. Previous study also showed

the annealing impurity contributed to voids formation during silicidation[11]. Therefore, we employed in-situ annealing in our study to produce consistent, continuous $CoSi_2$ films.

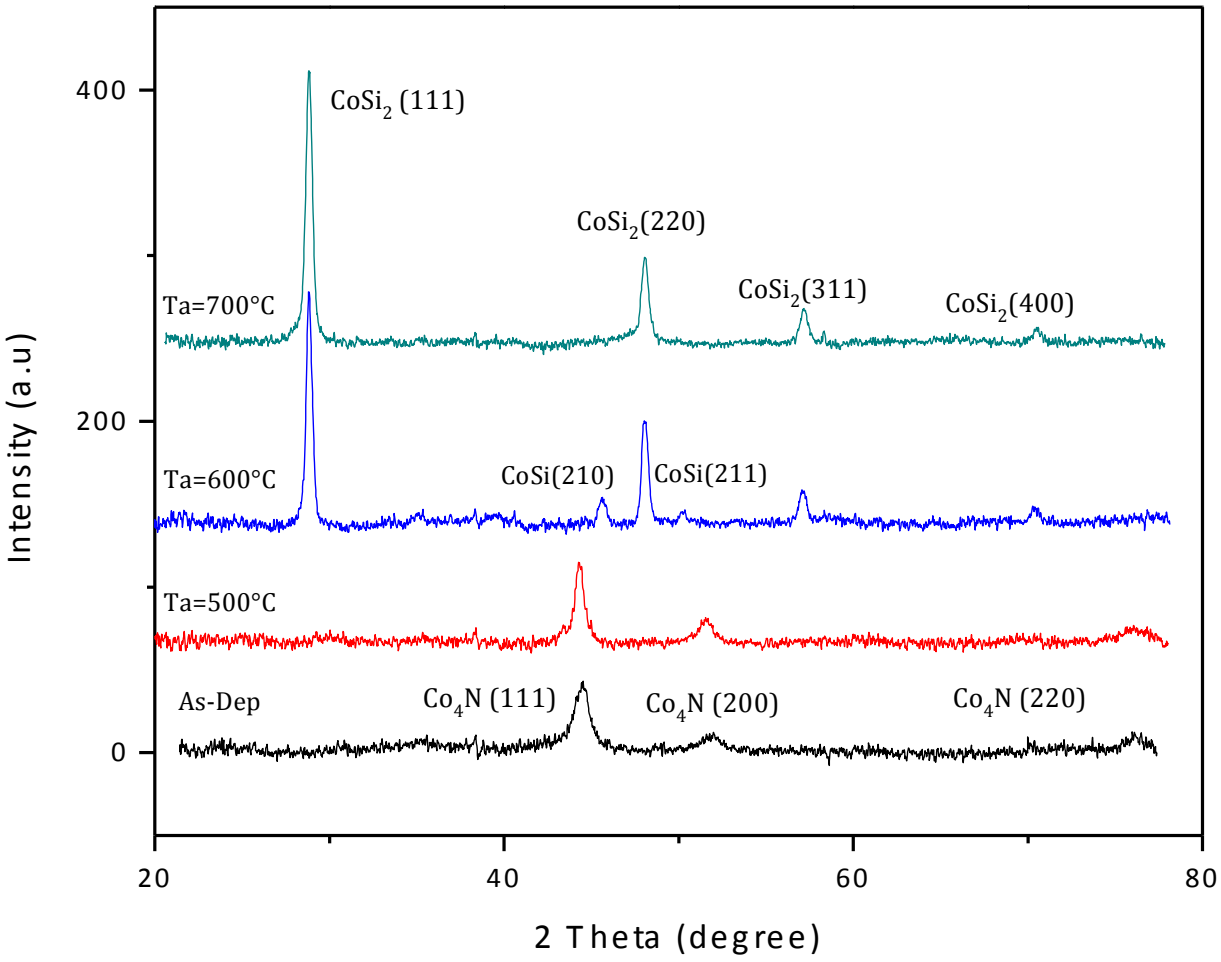

Figure 3.2. The XRD spectra of as-deposited Co_xN/Si(100) and the films after in-situ annealing in N_2 ambient (1 Torr) at various temperatures (T_a = 500°C, 600°C, 700°C) for 30 sec.

We used X-ray diffraction (XRD, Bruker D8) to study cobalt silicidation process by annealing Co_xN/Si(100) structure in-situ at 500°C, 600°C and 700°C in N_2 for 30 sec as shown in Figure 3.2. XRD measurements were carried out by using D8 diffractometer and 2-Dimensional detector. The as-deposited Co_xN showed face-cubic-centered (fcc) phase, as indicated by the previous study[8]. The Co_xN remained stable as fcc phase after RTA in 500°C.

After RTA at 600°C, $CoSi_2$ with (111) and (220) orientations dominated in the resulting films while CoSi (210) and (211) components simultaneously occurred. This suggests polycrystalline $CoSi_2$ startes to appear together with CoSi after annealing at 600°C. Meanwhile, the intensity of $CoSi_2$ (111) peak is greater than of other $CoSi_2$, CoSi peaks, indicating the film is textured. The CoSi completely transformed to $CoSi_2$ upon RTA at 700°C, forming a textured $CoSi_2$ with a (111) preferred orientation on the Si (100) substrate. The cubic $CoSi_2$ and CoSi phases were formed directly from cubic CoN_x films without intermediate Co-rich phases, such as tetragonal Co_2Si or orthorhombic Co_3Si at low temperatures. In a conventional Co silicide process, Co-rich phase silicide such as Co_2Si or CoSi generally formed at a low temperature ranging between 400 and 500°C[1]. These results indicate that because of retardation of the Co-Si reaction, the conversion of Co_xN to $CoSi_2$ does not involve the transformation into Co-rich phases at elevated temperatures. This finding agrees with the study on $CoSi_2$ formation processes by annealing the $Co/CoN_x/Si$ structure[12]. Additionally, $CoSi_2$ grown by the reaction of Co_xN on Si(100) produced polycrystalline $CoSi_2$ films as expected. Although $CoSi_2$ (cubic CaF_2 structure with a=5.36Å) and Si(cubic diamond structure with a=5.43Å) have small lattice mismatch of only 1.2% and similar crystallographic structure, it has been proved challenging to form epitaxial $CoSi_2$ on Si substrates. Bulle-Lieuwma et al.[13] explained the possible reason for the polycrystalline nature of $CoSi_2$ on Si (100). They suggested that the competition between different epitaxial orientations with similar matching resulted in the growth of polycrystalline $CoSi_2$.

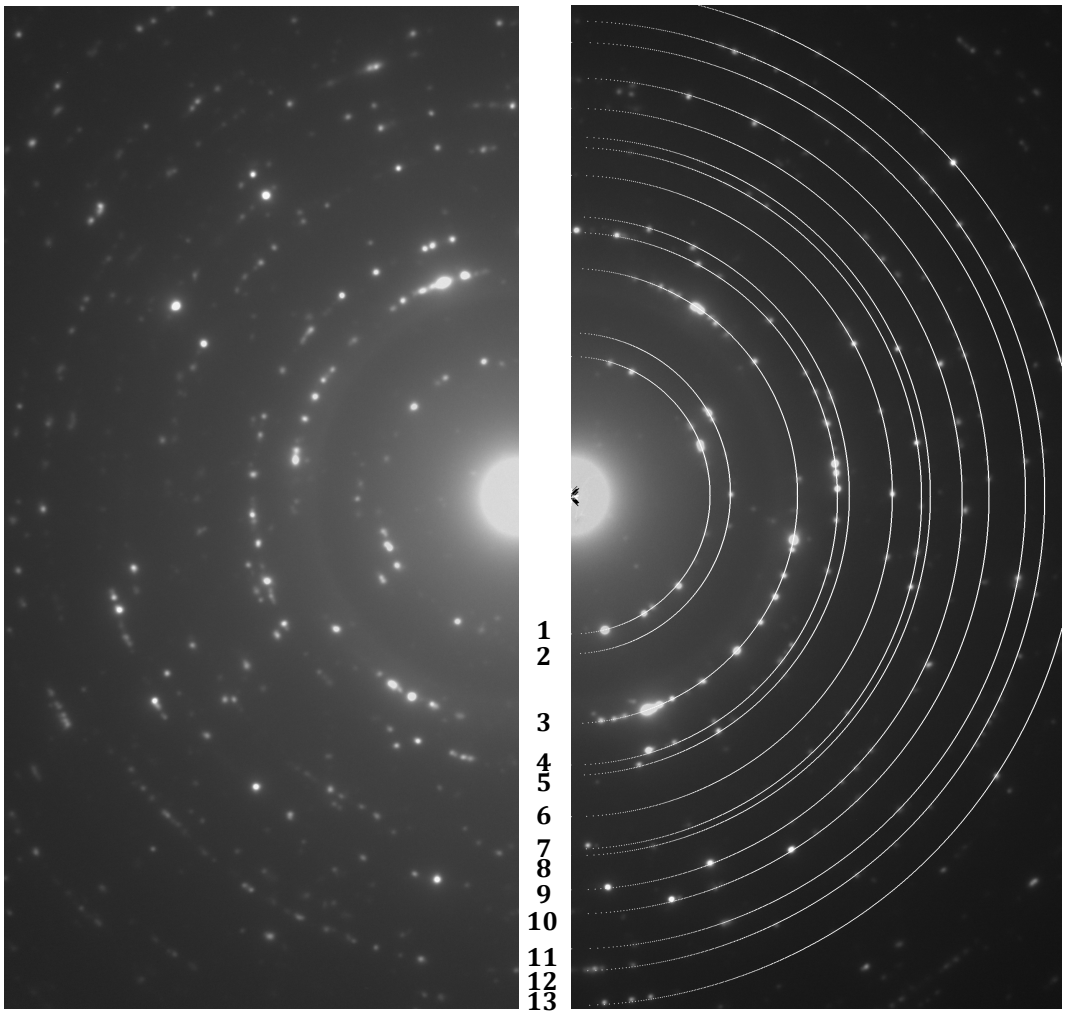

Figure 3.3. The electron diffraction (ED) images of $CoSi_2$ formed by *in-situ* annealing Co_xN/Si(100) in N_2 at 700°C for 30 sec. The diffraction rings #1~#13 corresponds to (111), (200), (220), (311), (222), (400), (331), (420), (422), (511), (440), (531), (620) crystalline planes of $CoSi_2$.

The Figure 3.3 shows the electron diffraction (ED) images of $CoSi_2$ from transmission electron microscopy (TEM; JEOL 2100 TEM system). ED result showed that the films are polycrystalline cubic cobalt disilicide. The speckled pattern of the diffraction rings indicated that the specimen have relatively larger grain sizes. The pattern showed part of the ring is more intense compared to the rest, indicating a textured film. This result agreed with the XRD result.

The resistivity of Co_xN and $CoSi_2$ thin films could be obtained by the measurements of the thickness and sheet resistance. A four point probe was applied to measure the sheet resistance. The unreacted cobalt nitrides (if any) on top of the formed $CoSi_2$ were removed by a heated dilute sulfuric acid solution at 50°C before the measurements. The scanning electron microscope (SEM) was carried out to measure the physical thicknesses. The as deposited 30 nm Co_xN film on Si (100) substrate would generate 110 nm $CoSi_2$ by in-situ annealing at 700°C. The thin film resistivity decreased from 140μΩ·cm to 20 μΩ·cm due to the formation of conductive $CoSi_2$. $CoSi_2$ with 20 μΩ·cm is closed to reported resistivity value of $CoSi_2$, i.e. 16~20 μΩ·cm[1].

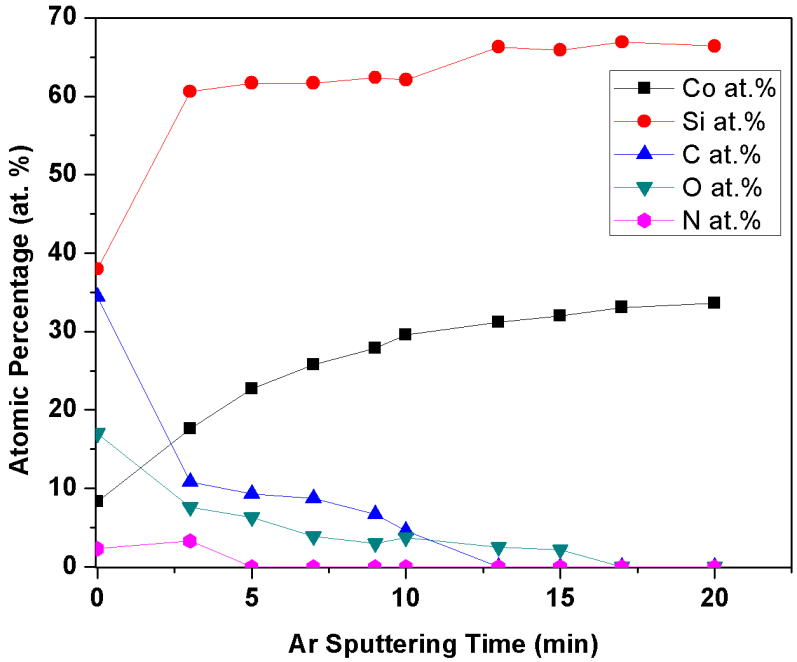

Figure 3.4. XPS depth-profile study of $CoSi_2$ formed by annealing Co_xN/Si (100) at 700°C

We studied the composition of $CoSi_2$ formed by annealing Co_xN on Si (100) substrate at 700°C by X-ray photoelectron spectroscopy (XPS) depth-profile. Figure 3.4 shows the XPS

depth spectra of the elemental atomic ratio determined from Co 3p, Si 2s, C 1s, O 1s and N 1s peaks. In the view of XPS depth spectra, N is initially detected. The trace N content on the surface can be attributed to the small amount of unreacted Co_xN left on the surface. C, O existed in the film because $CoSi_2$ was oxidized during the air exposure. We calculated the Co:Si ratio to be around 1:2 inside the film. This result confirmed that we obtained the $CoSi_2$ of expected stoichiometry upon annealing the Co_xN/Si at 700°C.

3.3 Formation of Cobalt Disilicide from CVD Cobalt Nitride

The $CoSi_2$/Si interfacial roughness is an important factor that affects device performance. We highlight here the backside sample preparation procedure to examine the $CoSi_2$/Si interfacial roughness by atomic force microscopy (AFM, Asylum MFP-3D AFM). The initial backside sample preparation was first proposed for SIMS sample preparation[9]. We adapted this method to remove the substrate and reveal the layer of interest, $CoSi_2$ layer. The $CoSi_2$ sample was prepared by in-situ annealing Co_xN/SOI at 700°C. We selected SOI instead of Si (100) as the substrates owing to its built-in etch-stop layer (e.g. buried oxide of an SOI wafer). The buried oxide in SOI allowed selective removal of remaining Si substrate and elaborate sample preparation[9]. We employed a combination of mechanic polishing, wet etching, and dry etching to reveal the $CoSi_2$/Si interface. Wet etching of Si-substrate is commonly performed using heated TMAH (tetramethylammonium hydroxide) or KOH solutions[14]. The wet etching is fast and easy to perform. However, the wet etching of thick and roughly polished remaining Si inadvertently leads to the formation of <111> faceted Si-pyramids. This formation of faceted Si-pyramids is caused by the highly anisotropic etch rates, with etch rates of <111> crystallographic orientation being 2-3 orders of magnitude lower than those of other major crystallographic orientations[14]. Therefore, wet etching

cannot be used in high-precision polishing step and an etch-stop layer is crucial for eliminating the impacts of this coarse etching step. Alternatively, the Si dry etching using XeF_2 gas exhibits essentially isotropic etch rates regardless of crystallographic orientations[14]. And XeF_2 dry etching has been proved to be highly selective towards $CoSi_2$. XeF_2 dry etching process is applied to remove remained thin Si on top of $CoSi_2$.

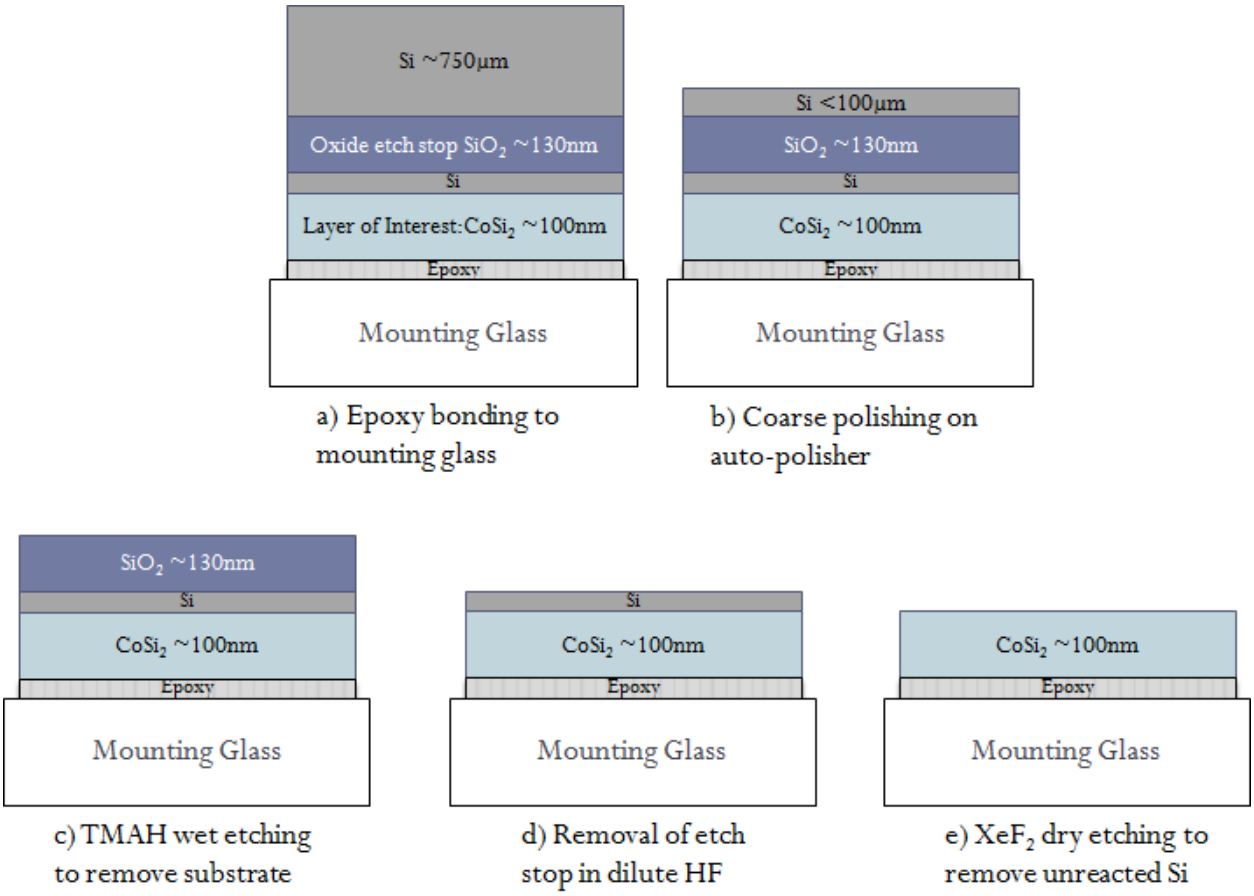

Figure 3.5. Schematic representation of consecutive steps in backside sample preparation procedure to reveal $CoSi_2$/Si interface: Sample is prepared by annealing Co_xN on SOI substrate at 700°C to form $CoSi_2$ on SOI. (a) Sample is invert and fixed on a support glass substrate of approximately same size. (b) Sample after grinding the backside substrate with SiC sand paper (600 -1200 grit) to reduce substrate thickness down to below 100 µm. (c) Sample after TMAH wet etching to selectively remove the residual silicon substrate. (d) Sample after a dilute HF etching to remove the exposed buried oxide. (e) Sample after dry XeF_2 etching to selectively remove the residual unreacted silicon, leaving the $CoSi_2$ surface ready for AFM measurements.

The backside sample preparation included 5 steps to reveal the $CoSi_2$/Si interface. The procedure is shown in Figure 3.5.

First, the sample was bonded upside down to a glass slide of similar size for mechanical support. Epoxy Bond 110 (Ted Pella Inc.) is used for bonding the two. Thin epoxy glue was carefully applied in between and degassed, then cured at 125°C for 10mins to obtain a homogenous glue film with good adhesion.

Second, the bonded sample stack was mounted onto a specimen mount – a cylindrical Pyrex stub (Gatan Inc.) using a low-melting-point wax (such as Crystalbond 509, Ted Pella Inc.). The stub was heated on a hot plate at 130°C~160°C to melt a tiny granule of wax for mounting the sample stack to be ground flat. Then a metal ring (Gatan Inc.) was used to hold the stub flat on the polishing sand paper. Rough thinning of the specimen was performed with a polisher (Allied High Tech Products Inc.) until a thickness of 100 μm or less was achieved. The Si substrate was coarsely polished by SiC sand papers of 600 grit and 1200 grit sequentially. The polished specimen was detached from the mounting stub by melting the wax on a hot plate and dissolving the remaining wax in acetone.

Third, the remaining Si substrate was removed by a heated TMAH (25 wt %) bath at 85°C. TMAH etching is highly selective towards the thermal oxide. Thus when no more bubbles were formed in the etching solution, it indicated the bulk Si had been completely removed.

Fourth, the sample was immersed in 10:1 buffered HF solution to remove the SiO_2 buried in the SOI.

In the final step, the residual Si was removed by dry etching with XeF_2 gas. This was performed in a home-built XeF_2 etching tool. Exposed Si would be quickly etched by alternating exposure to XeF_2 and subsequent pumping down of gaseous reaction products. Si will react with XeF_2 to form gaseous Xe and SiF_4. XeF_2 etching has been used to selectively remove Si because of its high selectivity of silicon versus photoresist, SiO_2, silicon nitride, Al, Cr, and TiN[14]. We experimentally determined the etch rates of $CoSi_2$ to be 200 times slower than of Si by XeF_2, thus XeF_2 etching can selectively remove the residual Si. As a result of the excellent selectivity towards $CoSi_2$, the etching process is highly robust and tolerant towards some over-etch. This final step leaves a smooth $CoSi_2$ surface, exposes the $CoSi_2$/Si interface to be examined by AFM. The interfacial roughness study is valuable for optimizing cobalt silicide process.

We successfully revealed the $CoSi_2$/Si interface and examined its roughness by AFM. The $CoSi_2$ formed at 700°C showed that the interfacial roughness was around 8% of the film thickness (see Figure 3.6), and the surface roughness was around 11% of the film thickness. On the other hand, when Co_xN/SOI was annealed at 600°C in N_2, the majority of the resulting film was $CoSi_2$, with a small amount of CoSi. The interfacial roughness of the resulting film $CoSi_x$/Si was determined to be around 11% of the film thickness, with its surface roughness around 11% of the total thickness. As summarized in Table 3.1, the surface roughness of $CoSi_x$/Si did not change much, while the $CoSi_x$/Si interfacial roughness is reduced after complete conversion of CoSi to $CoSi_2$ at 700°C. This is because $CoSi_2$ (cubic, lattice constant a= 5.36 Å) and Si (cubic, a= 5.54 Å) have a smaller lattice mismatch compared with CoSi (cubic, a= 4.45 Å) and Si.

Table 3.1. Summary of surface and interfacial roughness of $CoSi_x$/Si formed after *in-situ* RTA at 600°C, 700°C.

Si	Interfacial roughness percentage	Surface roughness percentage
CoxN/SOI after *in-situ* RTA@ 700°C	8.30%	11.10%
CoxN/SOI after *in-situ* RTA@ 600°C	11%	11.20%

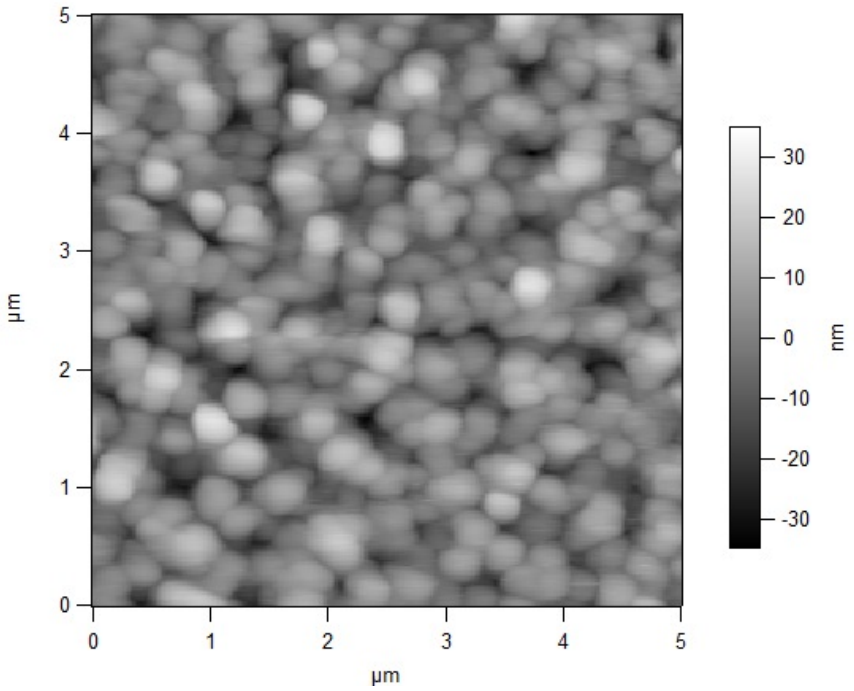

Figure 3.6. Measurement of $CoSi_2$/Si interfacial roughness by AFM. $CoSi_2$ is produced by annealing CVD Co_xN film at 700°C in N_2.

3.4 Conclusions

In conclusion, we successfully evaluated the $CoSi_2$/Si interfacial roughness quantitatively by using backside sample preparation procedure. We obtained the stoichiometric cobalt disilicide by *in-situ* rapid thermal annealing CVD-Co_xN at 700°C in N_2. The retardation of silicidation temperature is because the nitrogen inside the film slows down the cobalt and

silicon diffusion. The backside sample preparation utilized the combination of mechanical polishing, wet etching and dry etching to expose the $CoSi_2$/Si interface for AFM measurements. This approach provides a robust and reliable procedure for quantitative interfacial roughness assessment that offers important insights for cobalt silicide process development.

3.5 References

1 S.-L. Zhang and M. Östling, Critical Reviews in Solid State and Materials Sciences **28**, 1 (2003).

2 K. Maex, Materials Science and Engineering: R: Reports **11**, vii (1993).

3 J. Y. Dai, Z. R. Guo, S. F. Tee, C. L. Tay, E. Er, and S. Redkar, Applied Physics Letters **78**, 3091 (2001).

4 M. Tsuchiaki, C. Hongo, A. Takashima, and K. Ohuchi, Japanese Journal of Applied Physics **41**, 2437 (2002).

5 K. Kim, K. Lee, S. Han, W. Jeong, and H. Jeon, Journal of The Electrochemical Society **154**, H177 (2007).

6 F. M. d'Heurle and C. S. Petersson, Thin Solid Films **128**, 283 (1985).

7 K. Maex, A. Lauwers, P. Besser, E. Kondoh, M. de Potter, and A. Steegen, Electron Devices, IEEE Transactions on **46**, 1545 (1999).

8 H. B. Bhandari, J. Yang, H. Kim, Y. Lin, R. G. Gordon, Q. M. Wang, J.-S. M. Lehn, H. Li, and D. Shenai, ECS Journal of Solid State Science and Technology **1**, N79 (2012).

9 M. J. P. Hopstaken, C. Cabral, D. Pfeiffer, C. Molella, and P. Ronsheim, AIP Conference Proceedings **1173**, 94 (2009).

10 H. Li, G. Vereecke, K. Maex, and L. Froyen, Journal of The Electrochemical Society **148**, G344 (2001).

11 N.-S. Kim, C. Han-Seob, N.-K. Sung, R. Hyuk-Hyun, K.-S. Youn, and L. Won-Gyu, Journal of Vacuum Science & Technology A: Vacuum, Surfaces, and Films **20**, 1171 (2002).

12 S. I. Kim, S. R. Lee, J. H. Park, and B. T. Ahn, Journal of The Electrochemical Society **153**, G506 (2006).

13 Bulle, x, C. W. T. Lieuwma, A. H. van Ommen, J. Hornstra, and C. N. A. M. Aussems, Journal of Applied Physics **71**, 2211 (1992).

14 G. T. A. Kovacs, N. I. Maluf, and K. E. Petersen, Proceedings of the IEEE **86**, 1536 (1998).

Chapter 4 CVD Growth of Smooth, Highly Conformal Cobalt and Cobalt Nitride Thin Films by Direct Liquid Evaporation (DLE)-Chemical Vapor Deposition

Abstract

By a direct-liquid-evaporation chemical vapor deposition (DLE-CVD) method, we successfully deposited smooth low-resistance cobalt (Co) and cobalt nitride (Co_xN) thin films with excellent conformality at low temperatures down to 200 °C. In the DLE process, a cobalt amidinate precursor solution, bis(*N,N'*-diisopropylacetamidinato)cobalt(II) dissolved in tetradecane, was vaporized as it flowed smoothly, without boiling, inside heated tubing. This DLE process avoids creating unwanted particles that are made when droplets from a nebulizer evaporate in a conventional direct liquid (DLI) process. The vapor then mixed with ammonia (NH_3) and hydrogen (H_2) co-reactants and flowed over substrates in a tubular CVD reactor. The combination of NH_3 and H_2 resulted in a smooth highly conductive metallic cobalt thin film, while the hexagonal Co_3N phase was obtained when using NH_3 as the only co-reactant. DLE-CVD is a high-throughput process for high-quality Co, Co_xN films with excellent step coverage. This process demonstrated highly conformal Co and Co_xN films formation in trenches with 60:1 and 45:1 aspect ratio respectively. The good conformality is crucial towards realizing possible applications, such as in 3D contacts and interconnects in microelectronics.

4.1 Introduction

Thin films of cobalt (Co) and cobalt nitride (Co_xN) have attracted considerable attention for their applications in giant magnetoresistance (GMR) devices[1] [2] [3], spintronics[4] and microelectronics technology[5] [6]. For example, Co[5], Co_xN[7], or Co-based alloy[8] [9] have proven to be an effective adhesion layer in copper interconnect as they demonstrated enhanced adhesion between copper and barrier layers. Co has also been used as a wetting layer to induce void-free filling of narrow copper lines by reflow of non-conformal PVD copper for

sub-20nm nanostructures[10]. $CoSi_2$, fabricated by the reaction of Co with silicon, is a useful material for contacts due to its superior thermal and chemical stability[11 12].

Cobalt and cobalt nitride have been previously deposited by various means, including physically vapor deposition (PVD)[2 4], chemical vapor deposition (CVD) and atomic layer deposition (ALD) methods. As microelectronics and magnetic-storage devices continue to shrink in dimensions[13], highly conformal metal deposition is required for further downsizing and for the construction of ultra large scale integration (ULSI) with three dimensional structures. In these applications, the poor step coverage of PVD methods in deep contact holes caused severe limitations, while CVD and ALD are favored as they are able to produce high-quality and conformal thin films.

By thermal ALD with using bis(*N,N'*-diisopropylacetamidinato)cobalt(II) ($Co(^{i}Pr\text{-}MeAMD)_2$) precursor and H_2[5] or NH_3[14] co-reactants, successful deposition of high quality cobalt films have been realized at temperatures between 260°C and 350°C. The films exhibited resistivity ranging from 46 to 200 μΩ cm and excellent step coverage[5], coating holes with 40:1 aspect ratio conformally.

However, the growth rate of the ALD-Co is less than 1Å/min, which is too slow for many practical applications. In contrast, direct liquid injection (DLI)-CVD processes provide a much faster growth rate. It has the advantage of effective prevention of precursors' early decomposition as compared to the traditional bubbler delivery since the precursor solution is typically stored at room temperature[15]. Furthermore, this technique can be applied to a wide range of precursors, even those having low vapor pressure and/or limited thermal stability. DLI-CVD can deliver high vapor concentration of precursors that are hard to

achieve by conventional bubbler delivery, which is favorable for growing highly conformal films with high growth rates. DLI-CVD has been employed to deposit Ni[16 17 18], Co[18], cobalt oxide[19], Ag[18 20], Ru[21], Cu[18 22] and metal oxides (high-k)[23]. The DLI-CVD method typically employs a nebulizer to break up the liquid solution into tiny droplets, which then generate vapor when the droplets contact a hot carrier gas[18]. However this method is limited because it also produces small particles made up of non-volatile residues in the precursor after most of the precursor has evaporated. These particles can be carried along with the vapor into the deposition region, where they can contaminate substrates. Particles are a serious problem in microelectronics, where they can cause defects. Particles can also accumulate in the very narrow openings of a nebulizer and block the liquid flow. Blockage of a vaporizer can also arise if the solvent evaporates more quickly than a solid precursor.

Here we use a direct-liquid-evaporation (DLE) CVD method to avoid these particle and blockage problems during Co and Co_xN deposition. DLE vaporizes the precursor solution by flowing the liquid along the heated tubing coil inside the oven[24]. It takes advantage of the faster heat transfer from a heated solid tube to flowing liquid than the slower heat transfer from heated carrier gas to liquid droplets. In case of any non-volatile residue left by DLE, the residue tends to adhere to the bottom inside the tube, where it will remain instead of being carried into the reactor. And the inexpensive tubing coil could be cleaned or replaced before the residue builds up over a long period of time. Because the opening in the DLE tubing is much larger than the tiny nozzles in a DLI nebulizer, the tubing does not become clogged or blocked. Our DLE systems have demonstrated steady, reproducible performance over years without any need to replace the tubing coils.

For Co CVD/ALD processes, the choice of suitable cobalt precursor is crucial to obtain high-quality cobalt or cobalt nitride films. Inorganic cobalt precursors, such as cobalt halides, have low volatility and require high decomposition temperatures, which renders them unsuitable for CVD. Therefore, cobalt thin films deposition is typically carried out using various metalorganic precursors. Co can be deposited from thermal decomposition of $Co_2(CO)_8$ at substrate temperature ranging from 50°C to 200°C. However there are undesirable but kinetically favorable reaction pathways that compete with the deposition of pure Co, including polymerization of the precursor and formation of unstable $HCo(CO)_4$[25]. Co deposition from $CoCp_2$ [11,26 27 28] or $Co(acac)_2$[12, 29] typically requires relatively high reaction temperature above 250°C using H_2 or alcohol as reducing agent.

In this chapter, we chose $Co(^iPr\text{-}MeAMD)_2$ as the Co precursor because this cobalt amidinate has the potential of forming highly conformal cobalt and cobalt nitride films. We investigated the impact of different processing parameters and found the optimal conditions for producing highly-conformal, high-quality Co and Co_xN films by DLE-CVD. We successfully deposited highly conductive, pure metallic cobalt films using a mixture of NH_3 and H_2. The as-deposited Co film has excellent step coverage in trenches with 60:1 aspect ratio. On the other hand, using NH_3 as the only co-reactant in the deposition, we demonstrated the formation of hexagonal Co_xN conformally coating 45:1 aspect ratio trenches. The highly conformal Co and Co_xN films are promising materials for applications in next-generation microelectronic devices.

4.2 Experimental Section

The cobalt precursor is bis(N,N'-diisopropylacetamidinato)cobalt(II), $Co(^{i}Pr\text{-}MeAMD)_2$ (Dow Chemical Company). The synthesis of this cobalt amidinate has been reported previously[30 31]. The cobalt precursor is a dark green, air-sensitive solid in room temperature, with a melting point of 84°C. This solid precursor has a vapor pressure of ~30mTorr at 40°C[30]. Tetradecane $C_{14}H_{30}$ (olefin free, ≥99.0% (GC), Sigma-Aldrich Co.) was used to dissolve the cobalt precursor. The tetradecane solvent was purified of water and other impurities by distillation from sodium.

The cobalt precursor solution was prepared in a glovebox by dissolving 5 gram of $CoC_{16}H_{34}N_4$ ($Co(^{i}Pr\text{-}MeAMD)_2$) in 50ml tetradecane, forming a 0.38 molal (mol/kg of solvent), 12 wt% solution. The precursor solution was transferred into a glass container inside the glovebox. The solution was kept at room temperature and was pressurized by pure Helium (He) at pressure of 20psi. Helium is chosen as the push gas in order to minimize the dissolved gas in the solution, to prevent the gas bubbles contaminating the liquid flow controller's valve.

The flow of the precursor solution was controlled by Brooks Instrument's Quantim QMBC Coriolis flow controllers at adjustable flow rates up to 20g/hr. The typical cobalt precursor solution flow rate was set at 5g/hr. The flow of precursor solution was mixed with a 100 sccm flow of N_2 gas at room temperature in a tee. This mixture of the liquid solution and gas then flowed down into a coil of stainless steel tubing kept at 180°C in an oven, where the precursor solution vaporized. The vaporization temperature was chosen to be 150°C or above in order to evaporate the solution completely and quickly; 130°C was too low to

fully vaporize the solution. Depositions at 150°C and 180°C showed similar deposition rate, indicating 150°C was sufficient to evaporate the precursor completely. The vaporizing coil consists of two joined stainless-steel tubes (7" long, 1/8" diameter tube that connected to the liquid mass flow controller; 130'' long, 1/4'' diameter tube that connected to the inlet of the reactor chamber). A similar vaporizer design has been described elsewhere[24].

A Brooks Instrument nebulizer was initially used in a DLI process by breaking up the fluid into small micron-sized droplets before contacting a hot carrier gas. This DLI process, however, produced particles on the substrates. Also, the atomizer was susceptible to even slight contamination and easily got clogged in the 0.02" inner diameter tubing used to break up the fluid into droplets. DLI systems made by MKS Instruments and by Horiba were also tested in our laboratory and abandoned because of particle generation and clogging.

The vapor mixture exiting from the DLE vaporizing coil was then mixed with reducing agent NH_3 and/or H_2 just before entering the custom-built tubular hot-wall reactor. The substrates were supported on a stainless steel half-cylinder inserted into the reactor tube. A heating element and a control thermocouple were embedded in the half-cylinder to control the deposition temperature. The substrates were typically held at temperatures of 200~310°C and heated 10~20°C higher than the reactor wall temperature. The deposition pressure was set at 10 Torr. The co-reactant gases flow rates were controlled by mass flow controller (MKS Instruments), and the sum of the NH_3 and H_2 flow rates was typically held at 200 sccm. The ratio of NH_3 and H_2 was tuned to adjust the film composition. Table 4.1 summarized the fabrication conditions of the DLE-CVD Co/Co_xN films.

Table 4.1. Experimental conditions of DLE-CVD of cobalt or cobalt nitride

DLE-CVD parameters	Cobalt/Cobalt Nitride
Solvent	Tetradecane ($C_{14}H_{30}$)
Concentration	0.38 molal / 12 wt%
Co precursor solution reservoir temperature	Room temperature
Co precursor solution flow rate	5 g/hr (5~20 g/hr)
Vaporizing Coils temperature	180°C (150°C)
Carrier Gas N_2 flow rate	100 sccm
Co-Reactant Gas (NH_3 + H_2)	10+190, 20+180, 50+150, 100+100, 150+50, 200+0 sccm
Substrate Temperature	200°C (200~240°C)
Deposition Pressure	10 torr

Thermally oxidized silicon wafers, glassy carbon, and Si_3N_4 membranes (TEM grids from Ted Pella, Inc. 15nm Si_3N_4 membrane with 0.25×0.25mm aperture on 200μm Si.) were used as substrates. The substrates were treated by UV/ozone cleaner (Samco model UV-1, wavelengths = 185 nm and 254 nm) for 5 minutes at room temperature to remove organic contaminants.

The sheet resistance of the as-deposited films on silicon oxide was measured by a four-point probe station (Veeco Instruments; Model FPP-5000 or Miller Design & Equipment, Model FPP-5000). The mass of cobalt deposited was evaluated by Rutherford backscattering spectroscopy (RBS). The physical thickness of the film was measured by Field Emission Scanning Electron Microscope (FESEM; Zeiss FESEM Ultra Plus) or X-ray reflectometry (XRR). The relative amount of cobalt deposited was measured by the X-ray fluorescence (XRF). The crystalline phases were evaluated by transmission electron microscopy (TEM; JEOL 2100 TEM system). Depth profiling using X-ray photoelectron

spectroscopy (XPS; ESCA Model SSX-110) was used to study the elemental composition. The surface roughness of the films was evaluated by atomic force microscopy (AFM; Asylum MFP-3D AFM system).

4.3 Results and Discussion

4.3.1 Direct-Liquid-Evaporation Chemical Vapor Deposition (DLE-CVD) of Cobalt Nitride and Cobalt Metal

Previously, thermal ALD using $Co(iPr\text{-}AMD)_2$ and H_2 or NH_3 as a co-reactant was reported by several groups[5, 6, 14]. However, the growth temperature is relatively high (above 300°C), and the growth rate is slow (<0.5Å/cycle). In this paper, we show the CVD of either metallic cobalt or cobalt nitride at a low temperature of 200°C.

When using NH_3 as the only co-reactant, the films contain substantial amounts of nitrogen. RBS measurements determined the stoichiometry of the as-deposited cobalt nitride films to be around 3:1, as shown in Figure 4.1. The XPS depth-profile in Figure 4.2 also showed significant N in the cobalt nitride films. These films consist primarily of the Co_3N phase, as shown by TEM. Figure 4.5 shows the electron diffraction (ED) images from TEM of a Co_xN film deposited on an amorphous Si_3N_4 membrane. TEM result showed that the films are polycrystalline cobalt nitride with a hexagonal phase.

When using H_2 as the only co-reactant for the DLE-CVD cobalt deposition, the growth rate is very slow (<<0.5nm/min) at 300°C or lower. The cobalt film deposited at 310°C contains significant amount of carbon inside the film, ~30 at% C as determined by the XPS depth-profile. The carbon could be attributed to thermal decomposition of the cobalt precursor at 310°C.

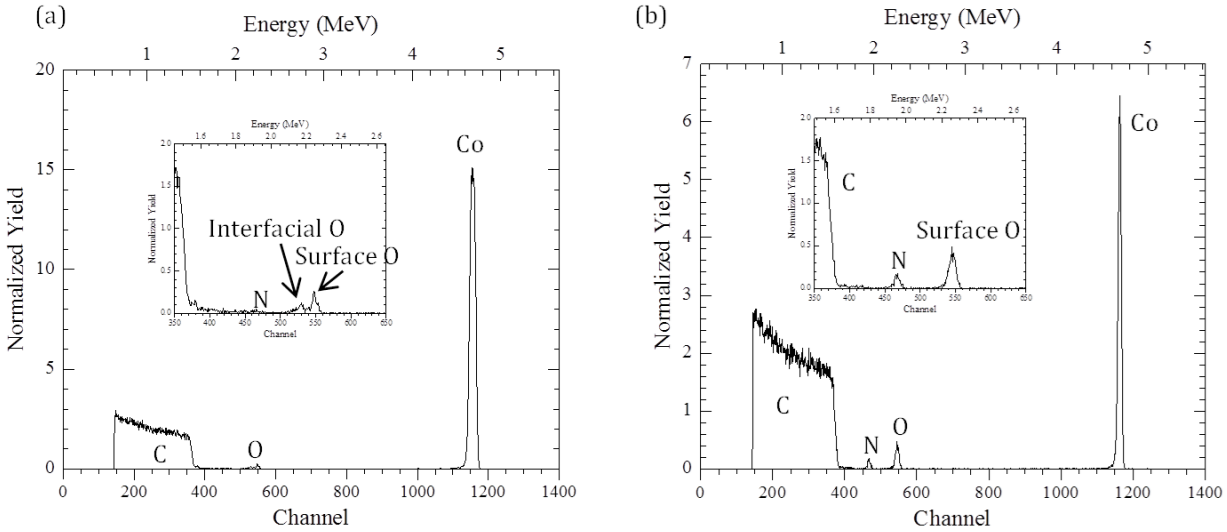

Figure 4.1. RBS spectra of (a) DLE-CVD Co films and (b) Co_3N film deposited at 200°C on a glass carbon substrate.

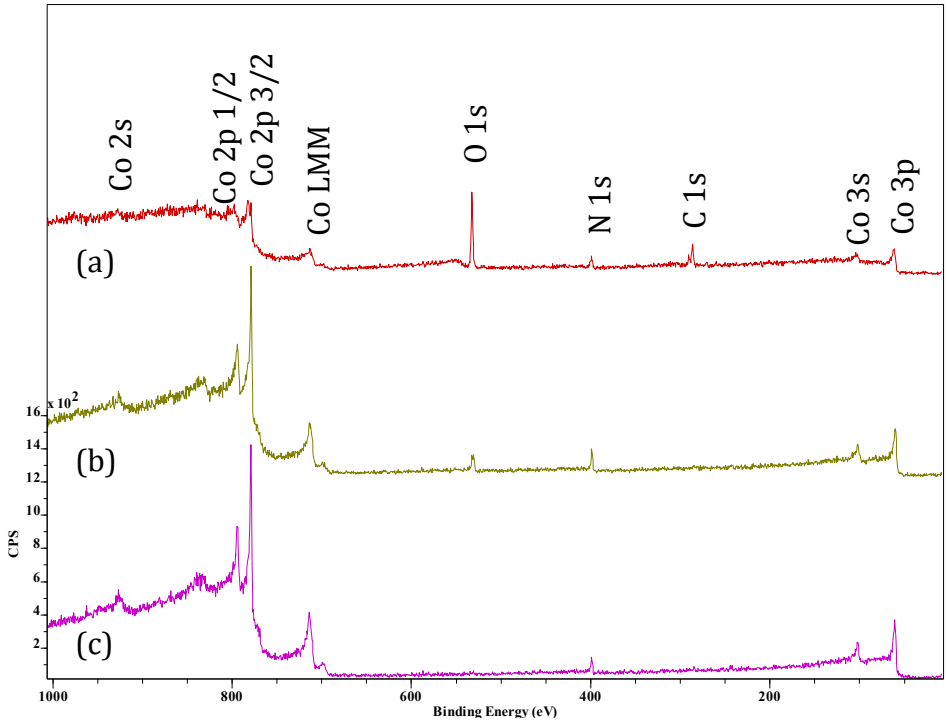

Figure 4.2. XPS survey of (a) DLE-CVD Co_3N deposited at 200°C, (b) after 1-min Ar sputtering, (c) after 5-min Ar sputtering.

When H_2 is used as a co-reactant along with NH_3 in the process, neither carbon nor nitrogen is incorporated in the film. Previous studies[8] showed post-deposition annealing in a H_2 atmosphere can eliminate nitrogen from cobalt nitride films. For the films deposited using both NH_3 and H_2, the RBS and XPS depth-profile studies revealed no C, N, O impurities inside the film regardless of the feed ratio of the two co-reactants. As shown in Figure 4.3, the XPS analysis of the cobalt film deposited from a mixture of H_2 and NH_3 shows no N 1s peak after Ar sputtering for 1 min, indicating the N content in the film is below the detection limit. The RBS result in Figure 4.1 also confirmed the conclusion above, with N content below the noise level. The existence of carbon and oxygen on the surface is due to inherent surface oxidation of the films upon exposure to air. Significant oxygen contamination at the surface is not surprising as the Co films will be oxidized upon exposure to the atmosphere[26].

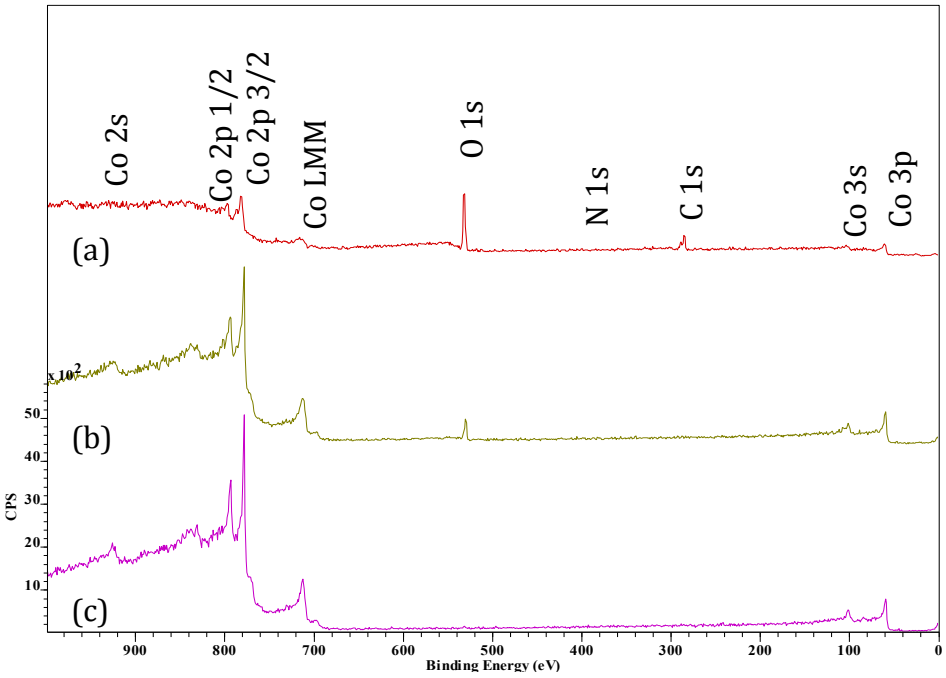

Figure 4.3. XPS survey of (a) DLE-CVD Co deposited at 200°C, (b) after 1-min Ar sputtering, (c) after 4-min Ar sputtering.

When NH_3 is used in addition to H_2 in the process, it significantly promotes the cobalt growth at a low temperature of 200°C. Shimogaki[8] and Gordon[32] calculated the activation energy of different reactive pathways using cobalt amidinate precursor with and without NH_3, and found that NH_3 was effective to speed up the deposition. Our experiments agreed with this result. With 10 sccm NH_3 and 190 sccm H_2 (i.e. 5% of the reducing agent is NH_3), the growth rate at 200°C reached ~3nm/min. In contrast, no film is deposited when no NH_3 is used. This suggests that NH_3 adsorbed on the substrate surface encourage the chemisorption of the cobalt amidinate precursor by reaction with NH bonds on the surface. As shown in Table 4.2, the deposition rate varied with different co-reactants combinations. Deposition at 10 torr and 200°C, with 100 sccm NH_3 and 100 sccm H_2 produced the cobalt film growth with best uniformity, with a relative low growth rate of around 1nm/min, as determined by XRR (see Figure 4.4).

Table 4.2. The crystalline phase of Co, Co_xN thin films deposited at 200°C by a varied ratio of NH_3/H_2 as co-reactants , and their corresponding electrical resistivity, deposition rate and the step coverage

NH_3 (sccm)	H_2 (sccm)	Phase	Resistivity (μΩ·cm)	Deposition Rate (nm/min)	aspect ratio of hole patterns with 100% step coverage
20	180	fcc-Co	~50	~2	~10:1
50	150	fcc & hcp-Co	~50	~2	~20:1
100	100	fcc & hcp-Co	~25	~1	~50:1
150	50	fcc & hcp-Co	~100	~2	~20:1
200	0	hcp-Co_3N	~160	~1	~45:1

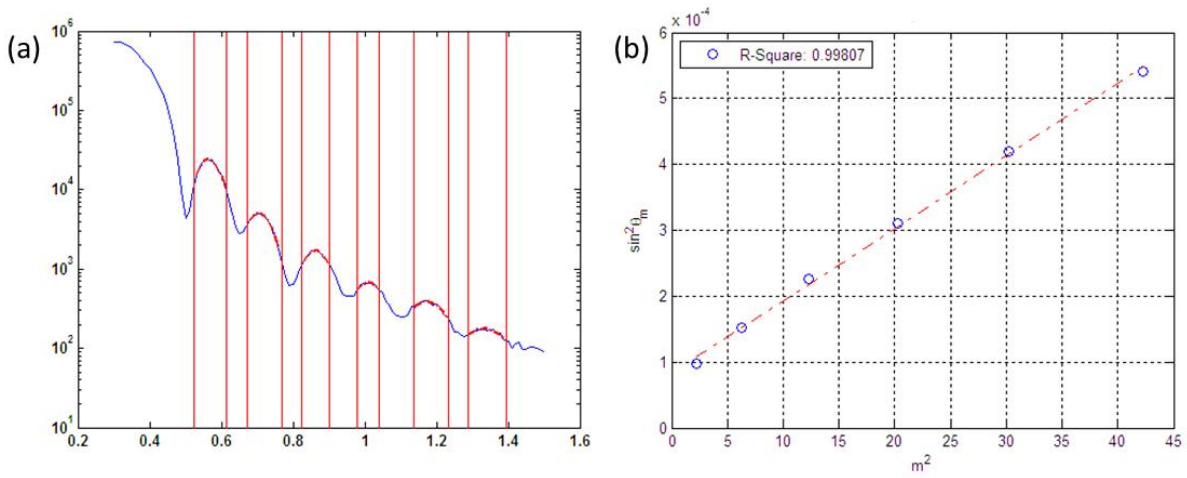

Figure 4.4. (a) XRR experimental curve and (b) fitted simulation line of a DLE-CVD Co film deposited on thermal oxide, thickness is calculated to be 23nm.

The crystalline phases of the as-deposited thin films evolved as the NH_3 concentration increased in the co-reactant. When 20 sccm NH_3 and 180 sccm H_2 served as co-reactants, the diffraction peaks correspond to the cubic Co phase (111), (200), (220), and (311) peaks as shown in Figure 4.5 (a). The ED showed that with gradual increase in NH_3 concentration amount, the crystalline phase of the film evolved from purely face-cubic-center (fcc) β-Co to a mixed fcc β-Co and hexagonal-close-packed (hcp) α-Co phase. As NH_3 ratio increases, smaller amounts of diffraction peaks corresponding to hexagonal Co phase start to appear, with major diffraction peaks corresponding to cubic Co phase. The hcp α-Co (100), (101), and (102) gradually becomes more evident along with the dominant fcc Co peaks as shown in Figure 4.5 (b) (c). Although hcp Co is a stable crystalline phase at temperatures up to about 450°C, metastable fcc Co is also commonly observed in Co films deposited at lower temperatures as has been reported by another group[33].

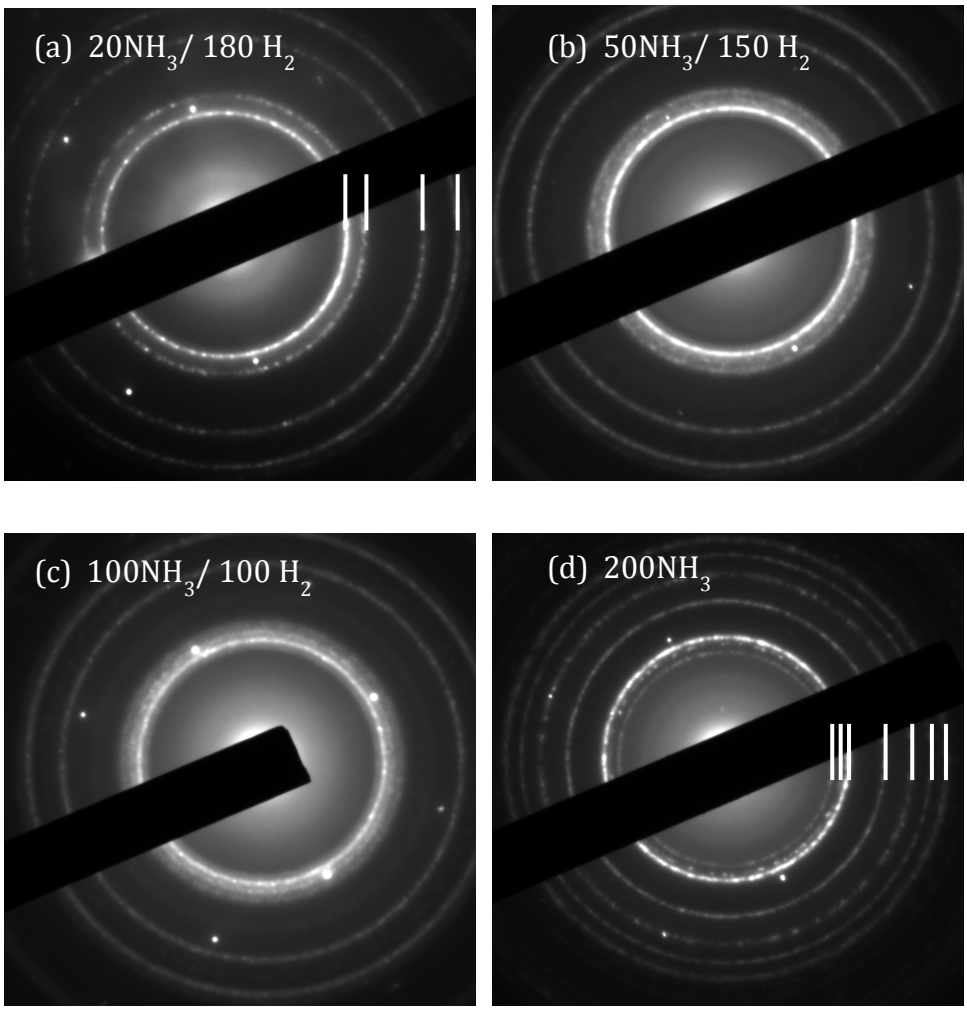

Figure 4.5. ED images of DLE-CVD CoN_x deposited with varied amount of NH_3, H_2 as co-reactant on thermal oxide. DLE-CVD Co deposited (a) with NH_3/H_2=20/180 sccm, (b) with NH_3/H_2=50/150 sccm, (c) with NH_3/H_2=100/100 sccm, (d) Co_3N deposited with 200 sccm NH_3.

The densities of as-deposited Co and Co_xN films were determined by combining the XRR thickness and the RBS areal density. For Co films deposited with low concentration of NH_3 and high concentration of H_2, the density was around 8.6 g/cm^3, close to the bulk Co density is 8.9 g/cm^3. The Co_xN film deposited with 200 sccm NH_3 showed a lower density of

5.5 g/cm^3. The deposited Co_xN has a relatively low density compared to calculated Co_3N density, 7.9g/cm^3 (see hcp Co_3N PDF Card No. 06-0691).

The resistivity of Co/ Co_xN films was affected by the deposition condition, in particular, the feed ratio of co-reactants, listed in Table 4.2. Cobalt films deposited with 100 sccm NH_3 and 100 sccm H_2 showed the lowest resistivity. The as-deposited 45nm-Co films had a resistivity as low as ~28 μΩ·cm, whereas the cobalt crystal bulk resistivity is around 6.2 μΩ·cm. The 15nm-Co_xN had a higher resistivity of ~160 μΩ·cm, which is similar with reported CVD-Co_xN[7] value of 180 μΩ·cm.

The surface morphologies of Co and Co_xN films using different co-reactants combinations were examined by SEM, as shown in Figure 4.6. The grain size of Co deposited using 10 sccm NH_3 and 190 sccm H_2 is largest among all the different growth conditions. As the ammonia flow rate increases from 10sccm to 20 sccm, the grain sizes become smaller. The grain size is smallest when NH_3 and H_2 are both 100 sccm, and the film is smoother as revealed by the AFM studies. The AFM images (Figure 4.7) showed the rms roughness value (~4.8 nm) was ~15% of total film thickness (~33nm) of as-deposited Co using 10 sccm NH_3. When NH_3 flow increases to 100 sccm, the rms roughness (~0.7 nm) of as-deposited Co was ~5% of total film thickness (Figure 4.7). When NH_3 further increases to 200sccm, the film deposited without any H_2 has relatively larger grain sizes (Figure 4.6) and higher roughness. The rms roughness value(~3.4nm) of Co_xN was ~15% of the total thickness.

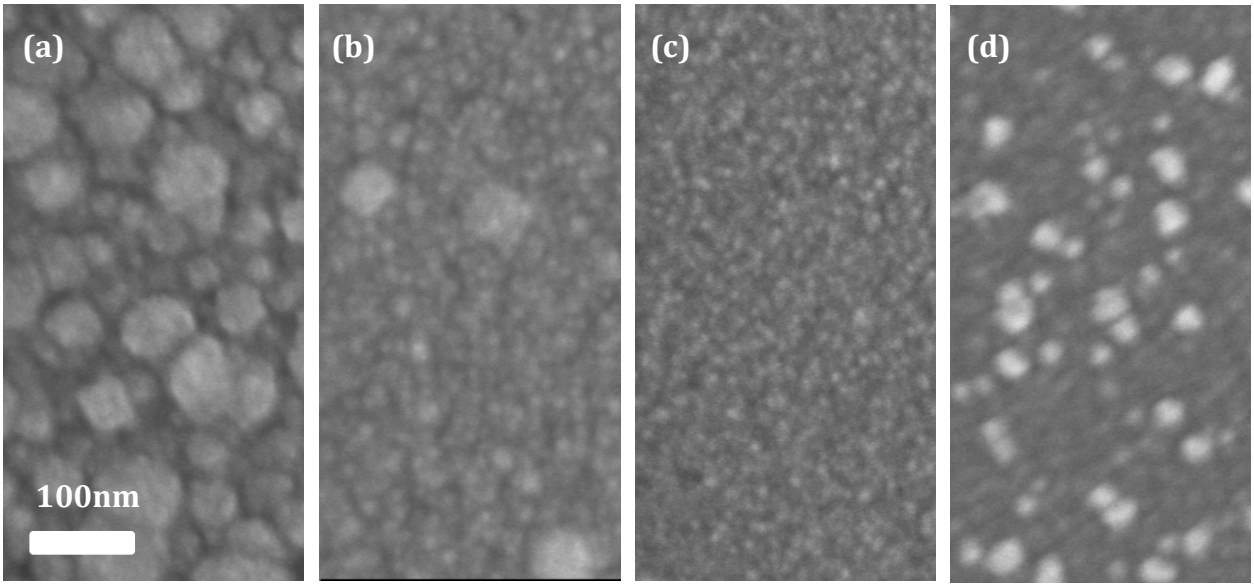

Figure 4.6. Plane-view FESEM images for the as-deposited Co film at 200°C with NH_3/H_2= (a) 10+190, (b) 20+180, (c) 100+100 sccm, and Co_3N film using (d) 200 sccm NH_3

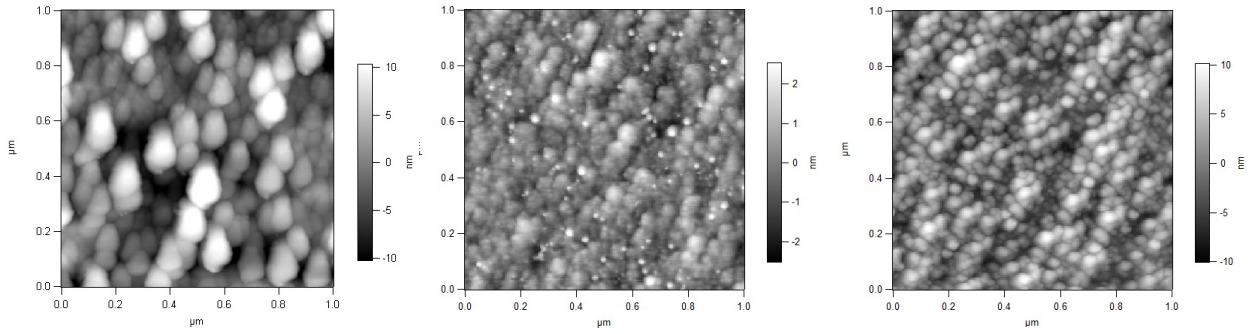

Figure 4.7. AFM images of DLE-CVD CoN_x deposited with varied amount of NH_3, H_2 as co-reactant on thermal oxide (a) 33nm-Co deposited using 10 sccm NH_3 and 190 sccm H_2 (rms roughness = 4.8nm); (b) 15nm Co deposited using 100 sccm NH_3 and 100 sccm H_2 (rms roughness = 0.7 nm); (c) 22nm Co_3N deposited with 200 sccm NH_3 (rms roughness = 3.4 nm).

4.3.2 Growth Rate

Impact of the Delivery Rate

The delivery rate of cobalt precursor solution has been changed to find out the deposition rate is saturated or not. Cobalt films are deposited at 200°C with the conditions of NH_3/H_2 = 100/100 sccm, at 10 torr on thermal oxide for 10 mins. The cobalt precursor solution was delivered at rates from 5 g/hr to 20 g/hr. Figure 4.8 (a) showed the deposition rate of DLE-CVD as a function of cobalt precursor solution delivery rate. In addition, we measured the sheet resistance of 10 different locations across the first 6" of the substrate holder. The plot in Figure 4.8 (b) showed the median of the 10 sheet resistance and the standard error versus the precursor solution delivery rate. When the precursor is delivered at 5g/hr, the film's sheet resistance is slightly higher than that of the film deposited with the delivery rate of 10~20 g/hr. The deposition rate is almost saturated at the precursor solution delivery rate of 5g/hr. The increased cobalt precursor delivery did not transfer to higher cobalt growth rate.

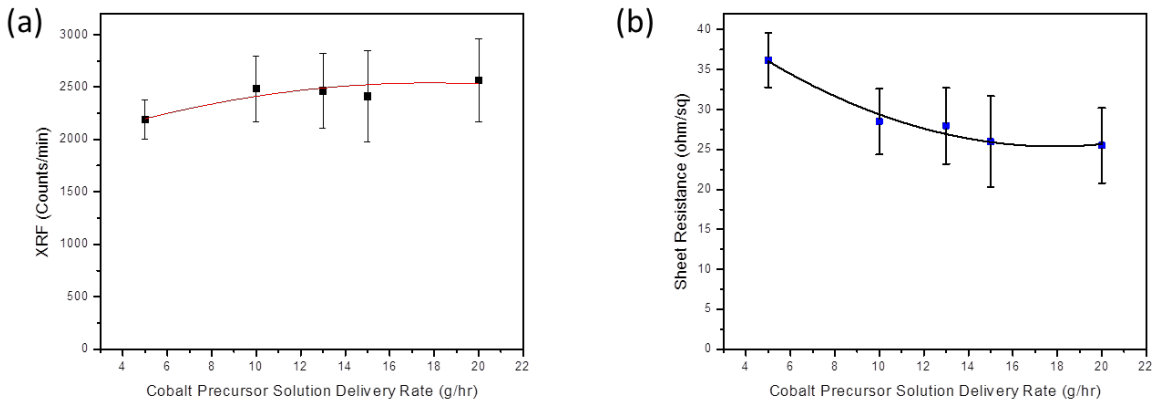

Figure 4.8. (a) The deposition rate (measured by XRF counts per minute) and (b) the sheet resistance of DLE-CVD Co films as a function of the cobalt precursor solution delivery rate.

The step coverages for different growth conditions were examined by depositing CVD Co/ Co_xN films on a silicon substrate with high aspect ratio features (provided by Tokyo Electron). Then the substrate was hand cleaved to study the cross-section of the holes. The feed ratio of NH_3 and H_2 in the co-reactant gases was found to be an important factor affecting the growth rate and the step coverage. The cobalt film grown with 100 sccm NH_3 and 100 sccm H_2 showed high conformality. The cross-sectional SEM images in Figure 4.9 (a) showed cobalt films deposited conformally on feature with the aspect ratio ~48:1 (170nm diameter and 8μm depth). The cobalt thicknesses at the top, side wall and bottom of the feature are almost the same as 18nm, resulting in a 100% step coverage. Similarly, Co_xN showed excellent step coverage, covering ~45:1 aspect ratio features uniformly, as shown in Figure 4.9 (b). The growth rate of the Co and Co_xN films under these conditions is around 1nm/min. However, when the flow rate of NH_3 is 10sccm, 20sccm, 50sccm, 150sccm, and the total flow rates of NH_3 and H_2 maintain as 200 sccm, the films growth rate becomes higher, but the films have less thickness uniformity along the substrate holder, leading to poorer step coverage. On the other hand, higher partial pressure of cobalt precursor can improve the step coverage. Thus a higher flow rate of cobalt precursor solution will enhance the step coverage. The film deposited using 12.5g/hr cobalt precursor delivery rate instead of 5g/hr, 100 sccm NH_3, 100 sccm H_2 at 200°C, 10 torr showed ~100% step coverage on a hole pattern with 60:1 aspect ratio (147nm in diameter, 8.8μm in depth). These results demonstrate the capability of achieving excellent step coverage using DLE-CVD method.

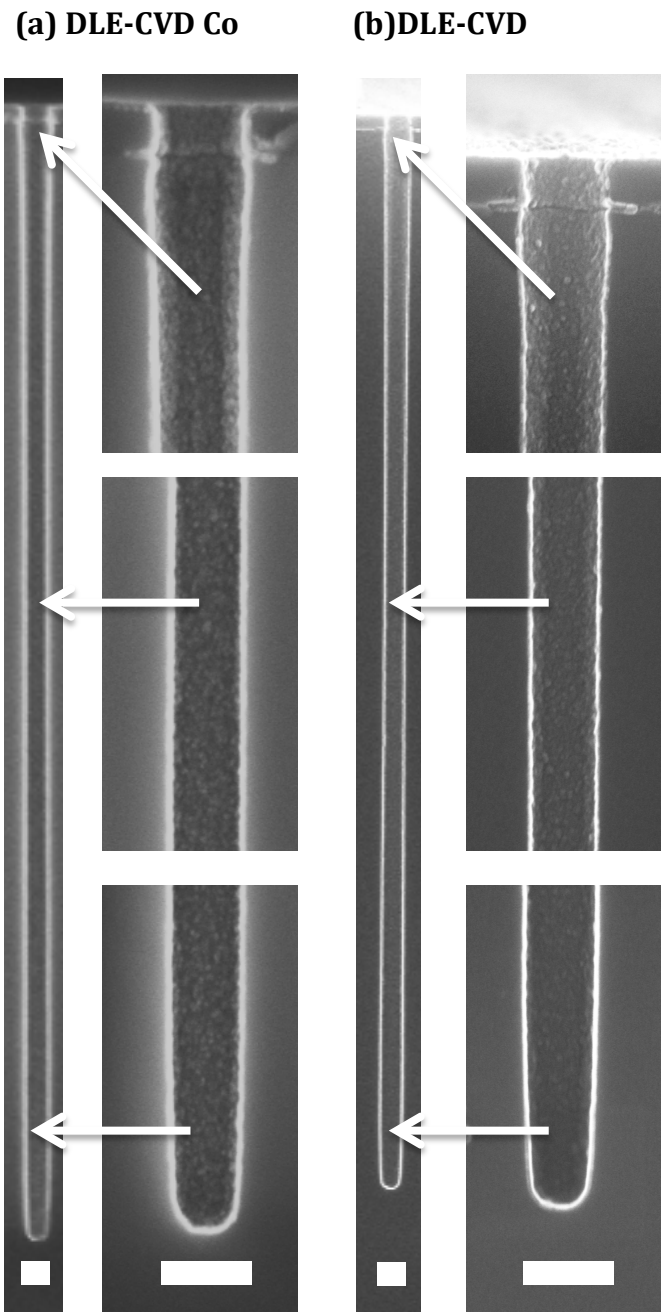

Figure 4.9. Cross-sectional SEM images of DLE-CVD (a) Co film and (b) Co_3N film deposited at 200°C on nanosized hole pattern. (a) ~18nm Co deposited with 100sccm NH_3 and 100sccm H_2 uniformly coating holes with 48:1 aspect ratio (170nm diameter and 8.2μm depth); (b) ~10nm Co_3N deposited with 200sccm NH_3 uniformly coating holes with 45:1 aspect ratio (170nm diameter and 7.6μm depth). The white scale bar corresponds to 200nm.

DLE-Co deposited using higher precursor solution delivery rate showed excellent step coverage due to the increase in the partial vapor pressure of cobalt precursor. For example, DLE-CVD Co deposited using 12.5g/hr demonstrated conformal coating inside trenches with an aspect ratio of 60:1 (see Figure 4.10).

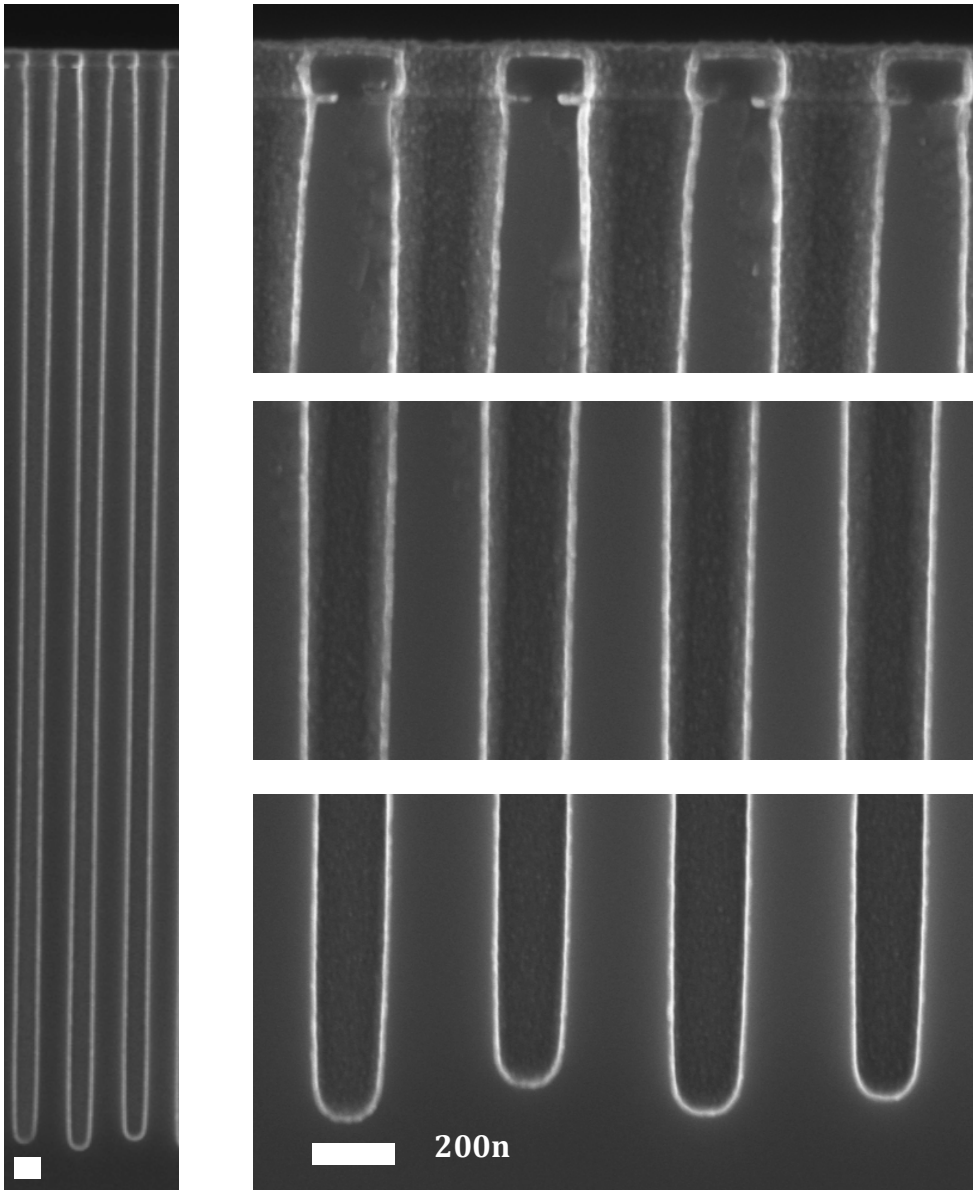

Figure 4.10. Cross-sectional SEM images of DLE-CVD Co film deposited at 200°C using 12.5g/hr cobalt precursor delivery rate on nanosized hole pattern. ~15nm Co deposited using 100sccm NH_3 and 100sccm H_2 uniformly coated hole patterns with 60:1 aspect ratio (147nm diameter and 8.8μm depth).

Temperature-Dependence of Growth Rate

Cobalt films were deposited at various temperatures of 200°C, 220°C, 240°C with NH_3/H_2 = 100/100 sccm, at 10 torr on thermal oxide. The growth rate increases as the deposition temperature rises. The amount of cobalt deposited is determined by XRF. An Arrhenius plot of the natural logarithm of the deposition rate and the reciprocal of temperature gives a straight line, the slope of which implies the activation energy of 57kJ/mol (see Figure 4.11). This experimental activation energy is relative low compared to cobalt films deposited using other cobalt sources. For example, the reported values of activation energy for using $CoCp(CO)_2$ [34] cobalt acetylacetonates ($Co(acac)_2$)[12], $CoNO(CO)_3$[33, 35], and bis(N-tert-butyl-N'-ethyl-propionamidinato)cobalt(II)[8] are 68 kJ/mol, 70kJ/ mol, 160 kJ/mol and 12 kJ/mol respectively.

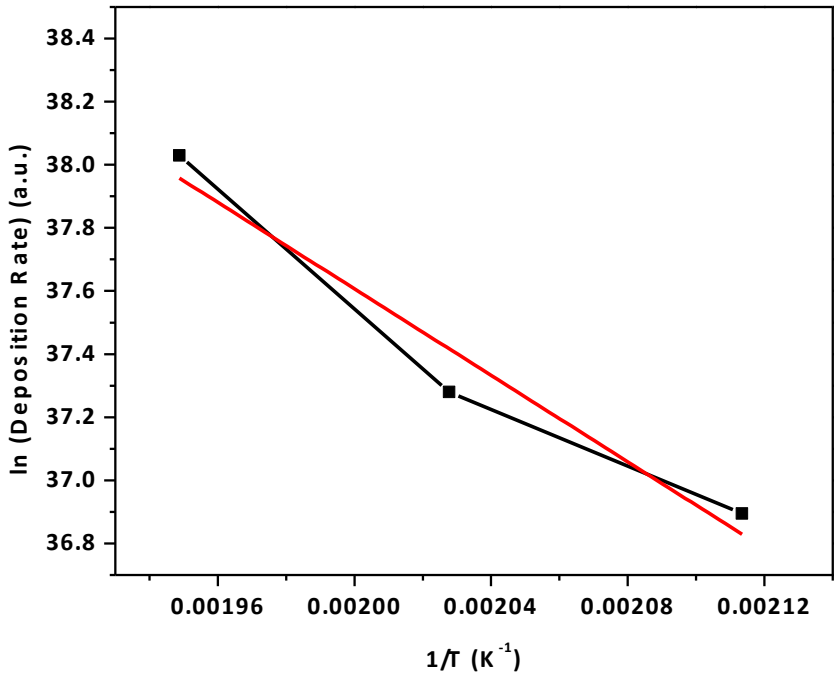

Figure 4.11. Arrhenius plot showing the natural logarithm of the DLE-CVD Co deposition rate at 200~240°C and the reciprocal of temperature. (The red line is the linear fitting based on the experimental data).

4.4 Conclusions

We used direct-liquid-evaporation chemical vapor deposition (DLE-CVD) processes to produce smooth cobalt and cobalt nitride films with excellent step coverage at a low temperature of 200°C. Co and Co_xN films were deposited by the reduction of bis(N,N'-diisopropylacetamidinato)cobalt(II) using a mixture of NH_3 and H_2. The use of ammonia in addition to H_2 promotes the cobalt growth at the temperature of 200°C. DLE-CVD Co and Co_xN films have much higher growth rates compared to those fabricated by atomic layer deposition (ALD) processes. 45nm-Co films showed cubic phase structure, with a low resistivity of ~28 μΩ·cm, uniformly coating trenches with 60:1 aspect ratio. As-deposited Co_xN showed hexagonal phase, covering trenches with 45:1 aspect ratio with uniform thickness. These results suggest DLE-CVD method is valuable for high-throughput Co and Co_xN deposition at low temperature for nanostructure fabrication.

4.5 References

1 S. S. P. Parkin, N. More, and K. P. Roche, Physical Review Letters 64, 2304 (1990).

2 A. E. Berkowitz, J. R. Mitchell, M. J. Carey, A. P. Young, S. Zhang, F. E. Spada, F. T. Parker, A. Hutten, and G. Thomas, Physical Review Letters 68, 3745 (1992).

3 C. T. Black, C. B. Murray, R. L. Sandstrom, and S. Sun, Science 290, 1131 (2000).

4 D. Chiba, S. Fukami, K. Shimamura, N. Ishiwata, K. Kobayashi, and T. Ono, Nat Mater 10, 853 (2011).

5 B. S. Lim, A. Rahtu, and R. G. Gordon, Nat Mater 2, 749 (2003).

6 Z. Li, R. G. Gordon, D. B. Farmer, Y. Lin, and J. Vlassak, Electrochemical and Solid-State Letters 8, G182 (2005).

7 H. B. Bhandari, J. Yang, H. Kim, Y. Lin, R. G. Gordon, Q. M. Wang, J.-S. M. Lehn, H. Li, and D. Shenai, ECS Journal of Solid State Science and Technology 1, N79 (2012).

8 H. Shimizu, Y. Suzuki, T. Nogami, N. Tajima, T. Momose, Y. Kobayashi, and Y. Shimogaki, ECS Journal of Solid State Science and Technology 2, P311 (2013).

9 H. Shimizu, A. Kumamoto, K. Shima, Y. Kobayashi, T. Momose, T. Nogami, and Y. Shimogaki, ECS Journal of Solid State Science and Technology 2, P471 (2013).

10 Y. Kokaze, S. Kodaira, Y. Endo, J. Hamaguchi, M. Harada, S. Kumamoto, Y. Sakamoto, and Y. Higuchi, Japanese Journal of Applied Physics 52, 05FA01.

11 G. J. M. Dormans, G. J. B. M. Meekes, and E. G. J. Staring, Journal of Crystal Growth 114, 364 (1991).

12 P. A. Premkumar, N. Bahlawane, and K. Kohse-Höinghaus, Chemical Vapor Deposition 13, 219 (2007).

13 (2012).

14 H.-B.-R. Lee, W.-H. Kim, J. W. Lee, J.-M. Kim, K. Heo, I. C. Hwang, Y. Park, S. Hong, and H. Kim, Journal of The Electrochemical Society 157, D10 (2010).

15 C. J. Anthony and R. C. Paul, Journal of Physics D: Applied Physics 36, R80 (2003).

16 Z. Li, R. G. Gordon, V. Pallem, H. Li, and D. V. Shenai, Chemistry of Materials 22, 3060 (2010).

17 Z. Li, R. G. Gordon, H. Li, D. V. Shenai, and C. Lavoie, Journal of The Electrochemical Society 157, H679 (2010).

18 N. Bahlawane, P. Antony Premkumar, K. Onwuka, K. Rott, G. Reiss, and K. Kohse-Höinghaus, Surface and Coatings Technology 201, 8914 (2007).

19 L. M. Apátiga and V. M. Castaño, Thin Solid Films 496, 576 (2006).

20 L. Gao, P. Härter, C. Linsmeier, J. Gstöttner, R. Emling, and D. Schmitt-Landsiedel, Materials Science in Semiconductor Processing 7, 331 (2004).

21 S. K. Dey, J. Goswami, A. Das, W. Cao, M. Floyd, and R. Carpenter, Journal of Applied Physics 94, 774 (2003).

22 D. Bollmann, R. Merkel, and A. Klumpp, Microelectronic Engineering 37–38, 105 (1997).

23 C. Dubourdieu, et al., Materials Science and Engineering: B 118, 105 (2005).

24 Z. G. Xiao, Review of Scientific Instruments 74, 3879 (2003).

25 J. Lee, et al., Journal of The Electrochemical Society 153, G539 (2006).

26 E. T. Hunde and J. J. Watkins, Chemistry of Materials 16, 498 (2004).

27 H.-B.-R. Lee and H. Kim, Electrochemical and Solid-State Letters 9, G323 (2006).

28 H. Shimizu, K. Sakoda, T. Momose, M. Koshi, and Y. Shimogaki, Journal of Vacuum Science & Technology A: Vacuum, Surfaces, and Films 30, 01A144 (2012).

29 P. A. Premkumar, A. Turchanin, and N. Bahlawane, Chemistry of Materials 19, 6206 (2007).

30 Z. Li, D. K. Lee, M. Coulter, L. N. J. Rodriguez, and R. G. Gordon, Dalton Transactions 0, 2592 (2008).

31 B. S. Lim, A. Rahtu, J.-S. Park, and R. G. Gordon, Inorganic Chemistry 42, 7951 (2003).

32 J. Wu, J. Li, C. Zhou, X. Lei, T. Gaffney, J. A. T. Norman, Z. Li, R. Gordon, and H. Cheng, Organometallics 26, 2803 (2007).

33 P. A. Lane, P. E.Oliver, P. J. Wright, C. L. Reeves, A. D. Pitt, and B. Cockayne, Chemical Vapor Deposition 4, 183 (1998).

34 M. F. Chioncel and P. W. Haycock, Chemical Vapor Deposition 11, 235 (2005).

35 A. R. Ivanova, G. Nuesca, X. Chen, C. Goldberg, A. E. Kaloyeros, B. Arkles, and J. J. Sullivan, Journal of The Electrochemical Society 146, 2139 (1999).

Chapter 5 Three-dimensional Atom Probe Investigation of Cobalt Nitride Thin Films

Abstract

In the world of microscopy imaging, atom probe microscopy (APM) occupies the high-spatial-resolution (sub-0.3 nm) and high analytical sensitivity (1 ppm) end of the spectrum. It is highly complementary to electron tomography and is applicable to a wide range of materials. The APM has been applied to study the DLE-CVD cobalt nitride thin films. Specimen preparation is emphasized as the key to success with modern atom probes. Atom probe specimens of cobalt nitride are prepared by direct coating the pre-sharpened microtips using DLE-CVD. We explored different analytical conditions and figured out the optimal analytical conditions for APM analysis of the cobalt nitride thin film. We studied the 3D compositional distribution of Co and N atoms inside the film and evaluated the concentration of C, O impurities by APM.

5.1 Introduction

The continuous down-scaling of devices has enabled the advancement of microelectronics industries over the past few decades. With characteristic length in logic and memory devices below 100nm, it is important to understand the structural and compositional information of materials at the subnanometer scale. Transmission electron microscopy (TEM) and secondary ion mass spectrometry (SIMS) are the two conventional techniques for structural and compositional characterization. However, both techniques are not capable of 3-D characterization at the subnanometer scale. This unmet need for microscopy capabilities has created an opportunity for another technique, atom probe microscopy (APM), to fill the gap.

The APM produces 3-D compositional images at the atomic scale with very high (1 atomic parts per million (ppm)) analytical sensitivity.[1-8] It controllably extracts atoms (ions) from

a needle-shaped specimen with a very high electric field applied to the surface. The extracted ions are projected onto a position-sensitive detector for recording their location. Time-of-flight measurements on the ions provide their isotopic identity as a mass-to-charge ratio of the ion. Because the 3-D position and chemical identity of atoms in a volume containing potentially hundreds of millions of atoms are collected, many types of information may be gleaned. Elemental concentration may be determined simply by the counting of atoms. Concentration profiles may be obtained in any direction. Isoconcentration surfaces can be set to delineate and measure interfaces. Interatomic distribution functions can be determined for studying ordering, dopant interactions, cluster formation, and early stages of precipitation. Therefore, we are interested to apply APM technique to study the useful electronic material in microelectronics, cobalt nitride and obtain its structural and compositional information at sub-nanometer scale in 3D.

5.2 Specimen Preparation

As with many experimental techniques, specimen preparation for atom probe microscopy is the key to the success. To attain the field strengths required for field evaporation in atom probe, the feature of interest must be positioned near the apex of a sharp needle-shaped tip. With the high speed of data analysis available in today's atom probe, the specimen preparation is an essential, and often challenging, part of the experiment.

5.2.1 Specimen Geometry Requirements

The essential geometry requirements of an atom probe specimen are as follows:[8]

1. *A sharp needle-shaped specimen with the specimen apex radius between 50 and 150 nm, the semi-angle (or named as half shank angle) less than 10°.*

   The specimen needs to be in the shape of a sharp tip to generate an intense field for field evaporation.

2. *A smooth surface with no protrusions, grooves or cracks.*

3. *A circular cross section.*

   Because the data reconstruction is based on the assumption of a hemispherical cap, any deviation from this shape such as surface protrusions, or asymmetrical cross section, will cause artifacts in the reconstructed data.

4. *The feature of interest must be positioned within approximately 100 nm of the specimen apex to ensure that it is included in the acquired datasets.*

5. *Sufficient specimen length and tip clearance to prevent shielding from the support structure and an absence of "secondary tips", or sharp protrusions in the vicinity of the tips.*

   Generally any sharp features should be ~100 μm away from the tip. Otherwise, if those sharp features are sharp enough to emit ions by field evaporation simultaneously, it will interfere the data collection from the main specimen.

6. *Specimen needs to be robust enough mechanically to allow for significant evaporation to occur.*

   Specimen fracture will occur when there is a weak link, such as a weak transverse interface or layer or a surface notch. The specimen fracture will terminate the data collection and stop the experiment.

7. *The specimen is self-supporting.*

8. *For voltage-pulsed atom probe, the electrical resistance to the apex of about 10^2 Ω or less.[2] For the typical geometry, the specimen resistance is dominated by the last 10 μm or so. Assume the material is uniform, this indicates the specimen resistivity of less than ~ 0.05 Ω·cm.*

The small specimen size enables the high electric field (~ 10 – 50 $V \cdot nm^{-1}$) necessary for field evaporation. Because the needle-shaped specimen is the primary optic of the microscope, specimen preparation forms a critical step in a successful APM analysis.

5.2.2 Deposition-Based Specimen Preparation

Conventionally, the needle-shaped specimens are formed by electropolishing. The electropolishing methods have been reviewed elsewhere.[8] Electropolishing has been the main method used to fabricate these needles from metal wires, whiskers, or blanks cuts (typically 0.25 ×0.25× 10 mm^3) from bulk materials. However, this method cannot be directly applied to APM specimen preparation from thin films.

Chemical vapor deposition has the capability of conformally coating the complex 3D structures. Therefore, the APM investigation of thin films deposited by CVD can take the advantage of the commercial electropolished metal wires. Instead of fabricating a needle-shaped specimen from the thin film sample, thin films by CVD can directly coated the sharp metal wires uniformly and be ready to examine under the APM. However, the quality of the commercial electropolished metal wires is not consistent. Evaluation of the initial shape of the metal wires is an important step before determining the thickness of thin film coating.

Alternatively, CVD thin films can directly deposited onto commercial pre-sharpened microtips (PSMs) coupons. PSMs are an ordered collection of tall (~ 100 μm) Si posts formed on a Si coupon with standard microelectromechanical systems (MEMS) techniques. The local electrode atom probe enables the field evaporation exclusively from a single needle-shaped specimen located among a field of similar needle-shaped specimen. Figure 5.1 illustrated the images of PSMs before any coating and PSMs coated with a thin layer of cobalt nitride.

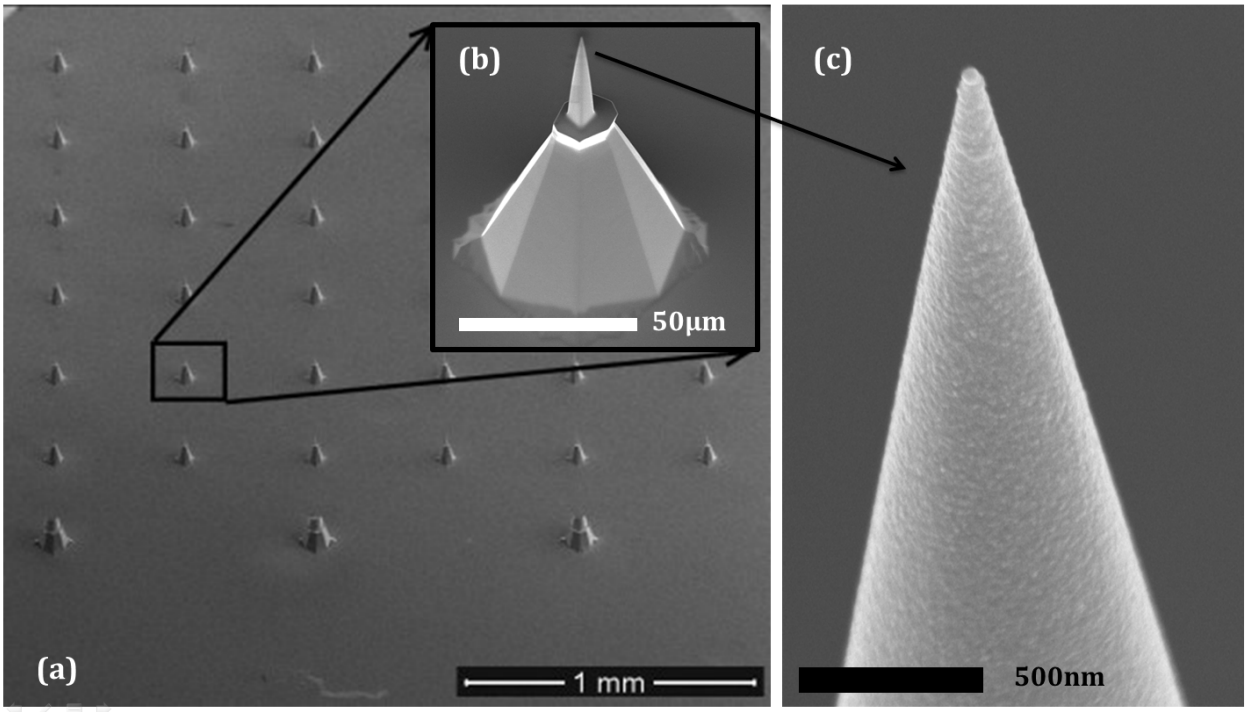

Figure 5.1. SEM images of (a) 36 pre-sharpened microtips (PSMs) specimen coupon (tapering to a sharp point less than 50 nm in diameter); height 100 μm ± 20 μm on a 3mm × 7 mm (± 0.2 mm) silicon coupon, doped to less than 0.1 ohm·cm resistivity. (b) Close-up view of one pre-sharpened Si microtip, (c) PSM coated with ~20 nm DLE-CVD cobalt nitride film.

These microtip arrays in PSMs enable the rapid preparation of a large number of nearly identical atom probe samples by providing a consistent platform for thin film coatings. The

apex of the specimen contains the coating, which is the feature of interest. The main advantages of microtip preparation are small material volume required, parallel processing of large numbers, uniformity of shape and position (in regular arrays), easy access to thin films on substrates, and low invasiveness on the specimen. These advantages can be very important when attempting to analyze complex materials structures for the first time. There is sometimes a learning curve to be overcome for complex materials, and the more uniform and numerous the tips the easier it is to obtain quality data. This method of using microtips is very useful when exploring different experimental conditions for analyzing thin film materials for the first time. In the next section, we assessed the impact of various experimental conditions for APM measurements on DLE-CVD cobalt nitride films and figured out the optimal conditions that offer a large dataset with good quality.

Specimen preparation by directly depositing on the PSMs or electropolished wires has the advantage of being a quick and easy method that does not require the use of expensive apparatus. However, this method is not applicable for preparing site-specific specimens. Another drawback includes the fact that the curved interfaces deposited on the surface of the tip may vary from the real materials that they are intended to simulate.

Here in this chapter, because the thin film deposited is uniform, this deposition-based method is effective and efficient in this case.

5.2.3 Focused Ion Beam (FIB)-Based Specimen Preparation

FIB-based specimen preparation methods offer the ability to fabricate atom probe specimen from a significantly wider range of materials and alternative specimen geometries than traditional electropolishing methods. This wide range of materials

includes multilayer and surface films, semiconductor devices, carbon filaments and whiskers, ceramics, and oxides including magnetite. Lift-out or coupon extraction methods have been used for site-specific specimen preparation for features such as grain boundries, interphase interfaces, low volume fraction or inhomogeneously distributed phases, coarse precipitates, as well as ion-implanted and subsurface regions. Additionally, the FIB may be used as a final step for electropolished specimen to correct artifacts and ensure a circular cross section with a smooth surface.

Generally, the FIB-based methods require a two-stage process. In the first stage, a post or a blank is fabricated or extracted from the region of interest. The blank is mounted on a support post with Pt or W deposition. The post or the blank is then sharpened into the atom probe needle-shaped specimen by annular milling technique in which the outer and inner diameters of a circular mask and the milling current are decreased progressively. Figure 5.2 illustrated and described the FIB-based site-specific specimen preparation in the case of a FinFET.

One of the major concerns of the FIB-based technique is the damage caused to the specimen by the ion beam. Commercial FIB use gallium liquid-metal ion sources with accelerating voltages between 2 and 30 keV. Both gallium implantation and ion mixing induce damage and artifacts in the specimen. In order to minimize the damage, it is routine

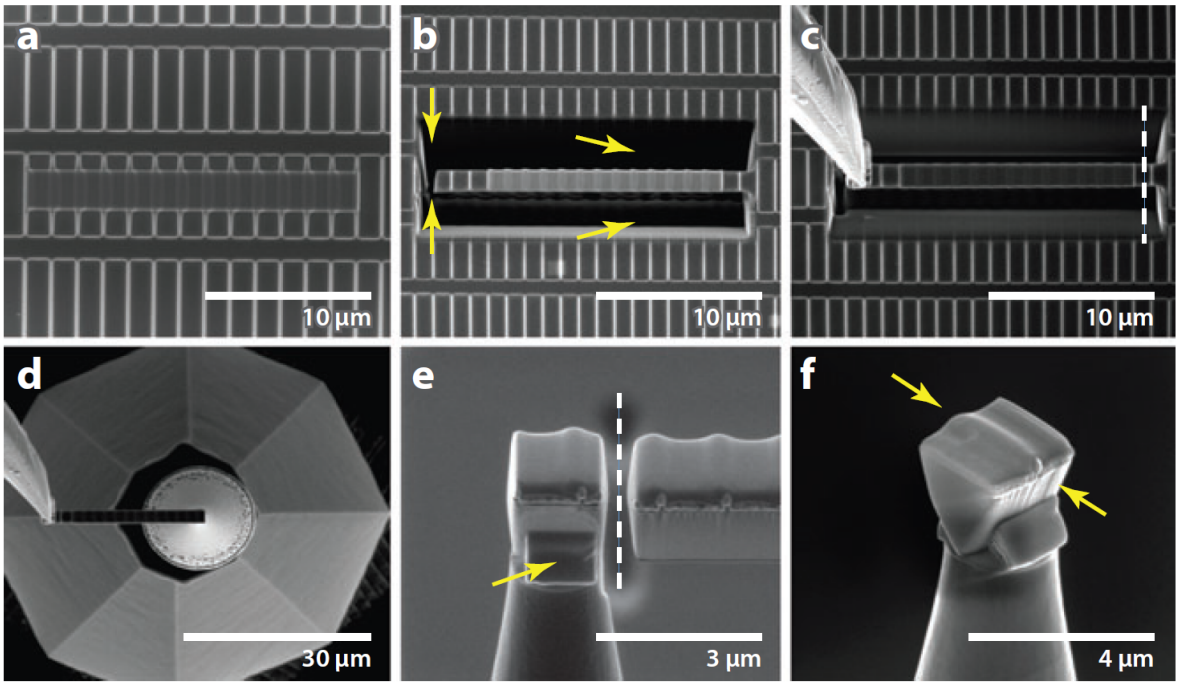

Figure 5.2. The steps involved in a standard focused ion beam (FIB) lift-out procedure. (a) A FIB-deposited protective strip is placed over the region of interest. This protective material is often Pt or W. (b) The material is then removed by ion milling around three sides of the region (*arrows*) as well as underneath to produce a long cantilevered wedge of material. (c) The wedge is removed by using an in situ micromanipulator (*attached to the left end of the wedge*) and then cutting the wedge free from the substrate (*vertical white line*). (d) The micromanipulator is used to position the wedge above the carrier microtip (seen in plan view). (e) The wedge is attached to the carrier-tip surface with FIB-deposited Pt (*arrow*) and then cut free from the carrier tip (*vertical white line*) for transfer to additional microtips. Once propagation of the wedge is complete, the FIB stage is rotated 180◦ so that a second Pt braze can be applied to the opposite wedge-post interface of each mounted post. (f) The final mounted wedge section is then ready for sharpening: The line of the targeted FinFET is clearly visible along the line of the arrows. (Source: APM review by Kelly, 2012[6])

to cap the region of interest with a thin protective Pt or W layer to protect the surface from the electron or ion beam before milling.

We have tried the FIB lift-out and annular milling to fabricate the atom probe specimen from the thin film sample. Ideally, with practice, the time to prepare 2 specimen tips is around 1 hr, which includes the extraction process, or 20 tips in around 4 hr. The ROI

(region of interest) can be located within ~ 5 nm with this method if it can be discerned in FIB. And the top surface of the specimen is typically capped with FIB-deposited Pt/C to protect it from the Ga beam in FIB. However, this FIB-based method has a steep learning curve for operation. And generally, the FIB-based method takes a long time (several hours to days) for sample prep. Figure 5.3 summarized several common issues that came with the FIB-based specimen preparation method. The final shaping of the tip is critical to determine the final tip shape, to correctly position the ROI near the apex of the tip, and to minimize ion damage.

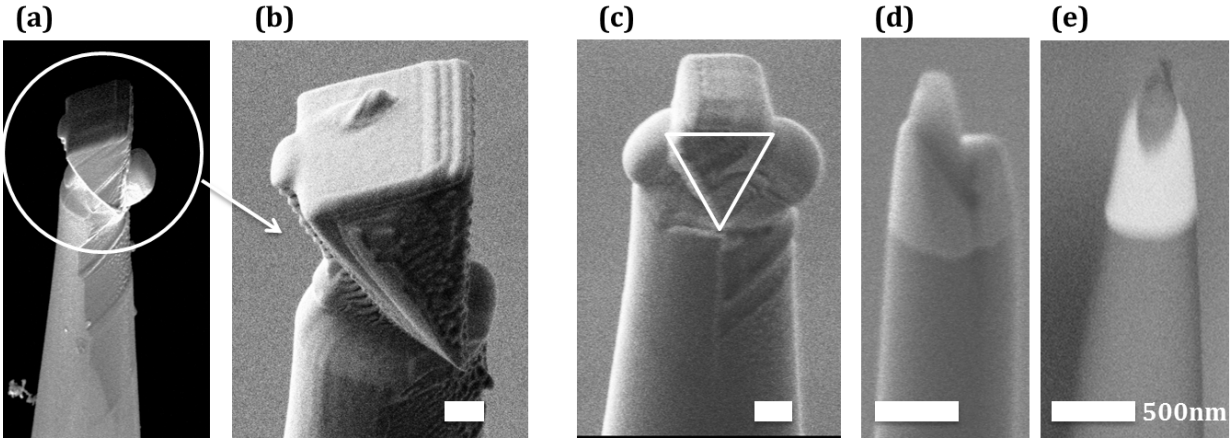

Figure 5.3 Common issues involved in the FIB-based specimen preparation. (a) The wedge is tilted after attaching to the carrier microtip surface. (b) Close-up image of the tilted wedge on the carrier microtip. (c) When the wedge (*the white triangle*) was placed on the carrier microtip, excess FIB-deposited W was applied to attach the wedge. (d) The excess W leads to a "secondary tip" close to the apex of the specimen. (e) The specimen in an ideal sharp-needle shape, but the region of interest is removed during annular milling step.

FIB-based method is great for site-specific specimen preparation and permits to fabricate atom probe specimen from a wide range of materials. However, this method is challenging to operate, and does not offer a large number of nearly identical atom probe samples as the deposition-based method. Thus, to investigate the optimal operating conditions for atom

probe, we prefer the deposition-based method. We will discuss about that in detail in the next section.

5.3 Atom Probe Investigation of Cobalt Nitride Thin Films

Cobalt nitride thin films are deposited by DLE-CVD method using bis(*N,N'*-diisopropylacetamidinato)cobalt(II) and NH_3 at 200°C. DLE-CVD Co_xN has demonstrated excellent conformality, which can be used to coat the PSMs. Experimental details have been described in chapter 4. The atom probe specimens are prepared by depositing ~20 nm cobalt nitride onto the PSMs arrays. As shown in Figure 5.1(c), the Co_xN coated the PSMs uniformly. Those Co_xN coated PSMs are sharp, with tip diameter in the range of 40~80 nm, and the shank angle (semi-angle) 8.0±0.3°. The specimen surface is smooth without any protrusions. The Co_xN coated PSMs have nearly identical structure for atom probe microscopy, therefore it provide a great platform to figure out the optimal conditions for APM.

5.3.1 Selecting the Optimal Analytical Conditions for Atom Probe Microscopy

As introduced in the first chapter, there are two main pulsing mode, HV (high voltage) and laser pulsing. HV-pulsing mode is limited to conductive materials, such as metals. Laser-pulsing is applicable to a wide range of materials, both conductive and non-conductive materials. Since cobalt nitride is conductive, both modes can be applied on Co_xN coated PSMs.

The universal adjustable parameters in APM experiments include the *specimen temperature*, the *detection rate*. The specimen temperature typically held between 20~50K to lower the surface diffusion. APM experiments are generally conducted at a constant

detection rate. The target detection rate is usually set to about a few atoms per 100 or 1,000 pulses on average, often between 0.2% and 5% of an atom per pulse. Changing the target detection rate effectively translates into a change in the electric field at the surface. An increase detection rate corresponds to a greater field. This will impact the atom probe results. For example, specimens maintained at higher electric fields, to generate enough ions per pulse, are more likely to be subjected to fracture. The probability of multiple events has shown to increase with increasing detection rate, probably due to an enhanced probability of correlated field evaporation and field dissociation of molecular ions at higher field. The relative amplitude of the background is generally lower at higher detection rate.

In the *HV-pulsing mode*, the adjustable parameters contain the *pulse fraction*, and the *pulse rate* (or the pulse frequency).

The *pulse fraction* is defined as the ratio between the amplitude of the HV pulses and the DC standing voltage. The pulse fraction needs to be adjusted to avoid the preferential departure or retention of any given species at the surface of the specimen.

As with the *pulse rate*, generally higher pulse rates are desirable for atom probe. However, a higher pulse rate translates into a shorter time detection window, which might not be long enough to detect complex ions. Compound material tends to exhibit field dissociation of large molecular ions, which requires a lower repetition rates must be used.

Table 5.1. summarized the atom probe investigations of Co_xN coated PSMs using HV-pulsing mode. As discussed earlier, higher detection rate and high pulse rate might cause specimen fracture. Also note that the background noise level is relatively high. With an HR instrument, less than 10 ppm/nsec is a good background level. Under 30ppm/nsec is an

Table 5.1. Atom probe results of Co_xN coated PSMs using HV-pulsing mode.

Yield (# of ions collected)	DR (Detection Rate) (%)	Voltage PF (Pulse Fraction) (%)	Voltage PR (Pulse Rate) (Hz)	Multiple event (%)	Background (ppm/nsec)	Fractured or survived
42k	0.5	20	200k	64.0%	20~120	fractured
67k	0.2	20	200k	35.3%	60+ --> 25	fractured
400k	0.2	20	100k	30.7%	120~200	survived
90k	0.2	20	50k	19.0%	60~100	survived

"acceptable" background level. However, it depends on the application. For instance, for GaN, the background has to be high due to the analytical conditions because it's difficult to run. 150ppm/nsec is considered way too high in any configuration. Additionally, the HV-pulsing mode did not generate enough ions for data analysis. This might because the Co_xN coated PSMs were not sharp enough in the beginning, that the voltage required for field evaporation exceeds the maximum voltage that the instrumentation can provide.

A relatively good HV-pulsing atom probe run is operated with 0.2% detection rate, 20% pulse fraction and 100 kHz pulse rate.

In the *laser-pulsing mode*, the adjustable parameters include the laser wavelength, the size of the laser spot and its position along the specimen's shank, the *laser energy*, and the *pulse frequency*. Most of the parameters are set for one instrument. The 3D atom probe (CAMECA, (CAMECA, LEAP 4000X HR) at Harvard operates using 355nm UV laser with 3μm (4σ) spot size. The laser spot's position along the specimen is adjusted to reach the largest detection rate at a certain experimental condition during the experiment. The laser energy and the pulse frequency are usually adjusted to obtain optimal results.

As with *pulse energy*, it should be adjusted to avoid any preferential evaporation. Preferential evaporation will lead to specific loss of the atoms with lower evaporation field.

Generally for laser pulsing, high *pulse frequency* can be problematic. If the time between two pulses is too short to enable the transfer of heat from the specimen surface, the temperature builds up, which leads to a strong degradation of the mass resolution and an increase in the background level, as a higher temperature favors the desorption of residual-gases adsorbed on the surface along with atoms left unstable by the field evaporation of a close neighbor.

Table 5.2. Atom probe results of Co_xN coated PSMs using laser-pulsing mode.

Yield (# of ions collected)	DR (Detection Rate) (%)	Pulse energy (pJ)	Pulse Frequence (Hz)	Multiple event (%)	Background (ppm/nsec)	Fractured or survived
2M	0.15	100	50k	4%	~10	survived
1.6M	0.2	100	100k	6%	10~12	survived
730k	0.2	40	250k	14%	120 ~20	survived

Table 5.2 summarized the atom probe investigations of Co_xN coated PSMs using laser-pulsing mode, which showed that with high pulse frequency, the background level is relatively high.

All the specimens survived in atom probe runs using laser-pulsing mode under various conditions. Observations to date also tend to support the hypothesis that laser pulsing leads to fewer specimen fractures.[2] Laser pulsing also is more gentle on the specimen since the standing field is kept some 10%–20% lower (stress is 20%–40% lower). The stress in a specimen increases with the square of the applied field. Laser-pulsing mode that makes it

possible to run at lower fields in the atom probe can reduce the probability of the specimen fracture.

A relatively good laser-pulsing atom probe run is operated with 0.2% detection rate, 100 pJ laser energy and 50~100 kHz pulse frequency.

Table 5.3. Atom probe results of Co_xN coated PSMs using laser-pulsing mode.

Length of time (hrs)	Yield (# of ions collected)	DR (Detection Rate) (%)	Laser PE (pulse energy) (pJ)	Laser PF (Pulse Frequence) (Hz)
~11hr	6M	0.2%	100	50kHz
~6.5hr	2M+	0.2%	50	50kHz
11.5hr+	10M+ ions	0.2%	50	100kHz
1.5hr	0.5M ions	0.2%	20	100kHz
~12.5hr+	600k+	0.2%	20	25kHz

We further investigated the impact of the laser pulse energy. As shown in Table 5.3, using a low pulse frequency in the range of 25~100 kHz, all the specimen survived and achieved good statistics for data analysis. The difference arises in the acquired mass spectrum. With higher laser energy, it leads to enhanced probability of field evaporation of molecular ions at higher field, which indicates a more complicated mass spectrum. Therefore, low laser pulse energy is favored as it generates a simpler mass spectrum.

5.3.2 Mass Spectrum Analysis

To study the N distribution of Co_xN coated PSMs, the mass spectrum is complicated because of the underlying Si microtip. The mass-to-charge (m/n) ratio of Si overlaps with N. The m/n ratios of Si^{2+} and Si^{1+} are 14, 14.5, 15, 28, 29, and 30 Da. On the other hand, the m/n ratios of N^{1+} and N_2^{1+} are 14, 15, 28, 29, and 30 Da. The difference between the two elements is m/n ratio at 14.5 Da. It is challenging to perform mass spectrum decomposition. decomposition. So for the initial data reconstruction, all the peaks in the position of 14,

14.5, 15, 28, 29, and 30 Da can be assigned as Si atoms. Then from the compositional map, we can observe a high concentration of Si atoms which indicated the location of Si microtip region. To analyze the Co_xN thin film, we can simply clip the region of interest, the thin layer of Co_xN, and reassign those peaks to N atoms. This provides an effective way to create 3D compositional mapping of cobalt nitride coatings.

5.4 3D Compositional Mapping of Cobalt Nitride

The 3D-APM investigation of the cobalt nitride thin film coated PSMs were conducted with a local electrode atom probe in laser mode (CAMECA LEAP 4000X HR). During the measurements, a UV laser was operated with a laser energy of 20pJ at a pulsing frequency of 100 kHz and an evaporation rate of 0.2%. The specimen temperature was cryostatically controlled and kept at around 20K. To guarantee proper statistics, only datasets with more than 500,000 atoms are considered. Compositional and structural information was reconstructed using the IVAS software packages. The 3D-atom maps (Figure 5. 4) graphically propose a uniform distribution of Co and N atoms in the as-deposited film.

Atom probe microscopy not only offers high spatial resolution, but also high analytical sensitivity (as good as 1 appm) over volumes of greater than 10^6 nm^3 (100 nm ×100 nm×100 nm). We examined the concentration of different elements inside the cobalt nitride thin film. Previous compositional study by XPS and RBS in Chapter 4 shows that the cobalt nitride thin film did not contain C and O inside the film. As shown in Table 5.4, the concentration analysis by atom probe confirmed that the number of C and O atoms inside the DLE-CVD cobalt nitride is much less than 1% of all atoms.

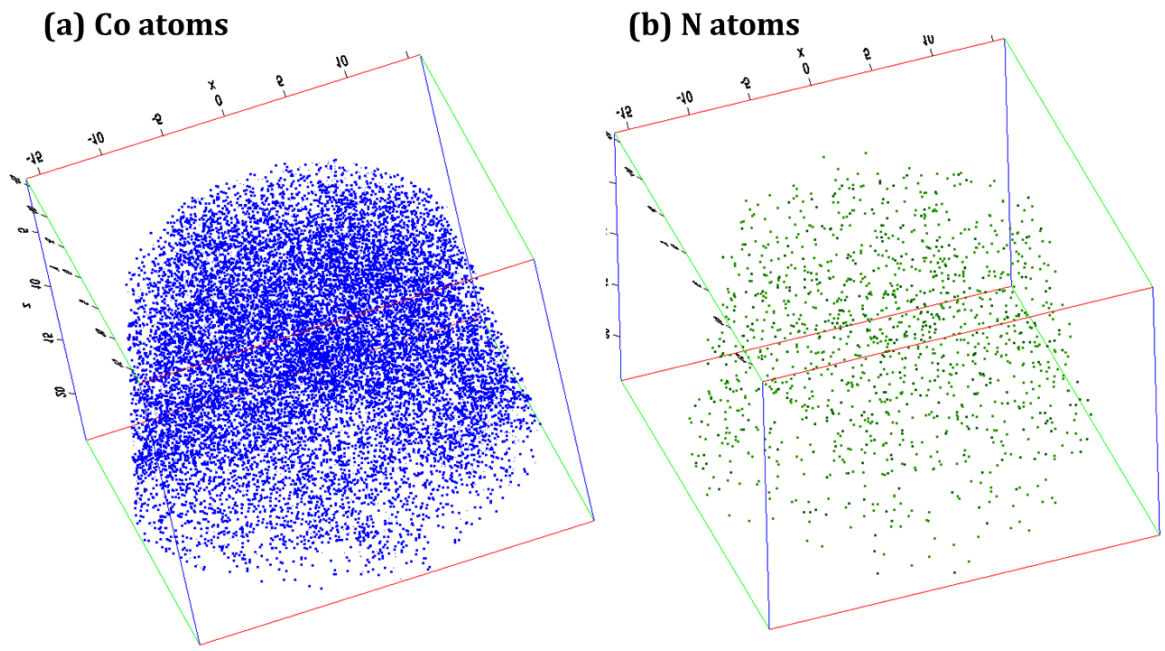

Figure 5.4. Spatial distribution of (a) Co and (b) N atoms in the cobalt nitride thin film. For visualization purpose, only 5% of detected Co, N atoms are illustrated in the reconstructed 3D-atom maps.

Table 5.4. Concentration of various elements inside the cobalt nitride thin films.

Ion Type	Decomposed Fraction
Co	82.2%
N	11.50%
H	5.6%
O	0.4%
C	0.2%

We further examined the spatial distribution of Co and N atoms within a 0.7 nm section (along the z direction, vertical to the microtip coupon plane) of cobalt nitride thin film. This compositional mapping (Figure 5.5) showed that the cobalt nitride thin film have small grains of around 5nm. This is confirmed by the TEM images (Figure 5.6) of DLE-CVD Co_xN deposited on the amorphous Si_xN membrane. From the reconstructed image, it also showed

that N atoms is distributed around Co atom centers, not agglomerated in the grain boundaries. This indicates that DLE-CVD method formed a uniform cobalt nitride thin film.

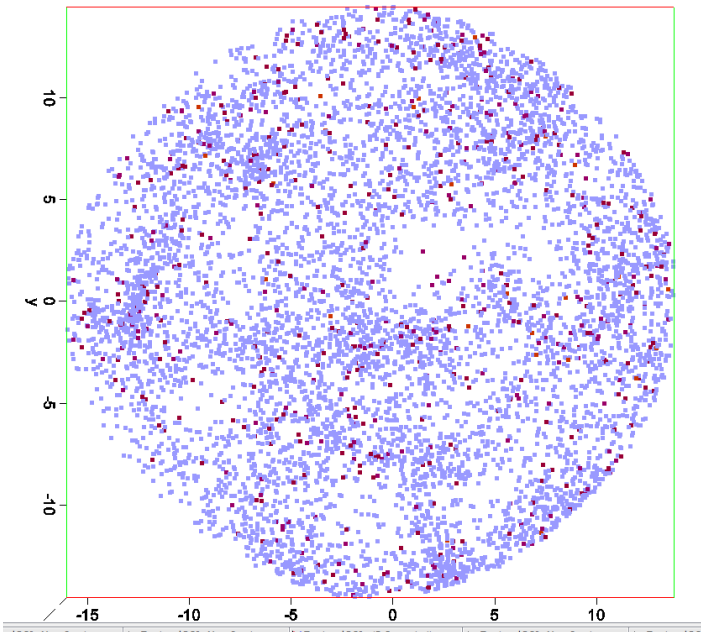

Figure 5.5. Spatial distribution of Co (in purple) and N (in red) atoms within a 0.7 nm section of cobalt nitride thin film. For visualization purpose, only 5% of detected Co, N atoms are illustrated in the reconstructed 3D-atom maps.

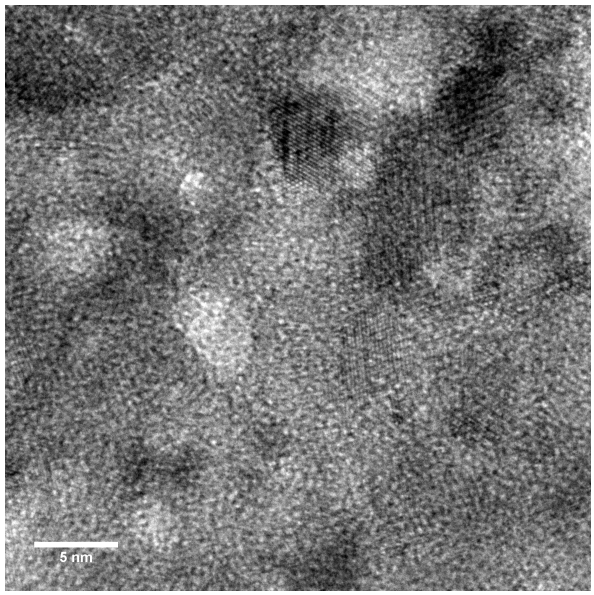

Figure 5.6. TEM image of DLE-CVD Co_xN on amorphous Si_xN membranes.

5.5 Conclusions

This chapter has successfully demonstrated that APM analysis can be effectively applied to the understanding of the microstructure and compositional properties in thin films with applications in microelectronics. The validity of the technique has been proved by the application of APM for cobalt nitride thin films. Various specimen preparation methods have been discussed on their advantages and limitations. And the impact of different analytical parameters in atom probe has been investigated. Using APM, we obtained 3D compositional information of DLE-CVD cobalt nitride thin films.

In conclusion, we believe that atomic-scale characterization using APM, possibly combined with other techniques, provides a unique tool that can be applied both to the design of nanostructured microelectronic applications and to the further understanding of the fundamental physical properties on which their operation relies.

5.6 References

1 T. F. Kelly, D. J. Larson, K. Thompson, R. L. Alvis, J. H. Bunton, J. D. Olson, and B. P. Gorman, Annual Review of Materials Research 37, 681 (2007).

2 T. F. Kelly and M. K. Miller, Review of Scientific Instruments 78, 031101 (2007).

3 D. N. Seidman, Annu. Rev. Mater. Res. 37, 127 (2007).

4 D. N. Seidman and K. Stiller, MRS Bull 34, 717 (2009).

5 B. Gault, M. P. Moody, J. M. Cairney, and S. P. Ringer, Materials Today 15, 378 (2012).

6 T. F. Kelly and D. J. Larson, Annual Review of Materials Research 42, 1 (2012).

7 T. F. Kelly, M. K. Miller, K. Rajan, and S. P. Ringer, Microscopy Today 20, 12 (2012).

8 M. P. Moody and J. M. Cairney, Atom probe microscopy (Springer, 2012).

Appendix

DLE-CVD Cobalt Reactor Operation Guide

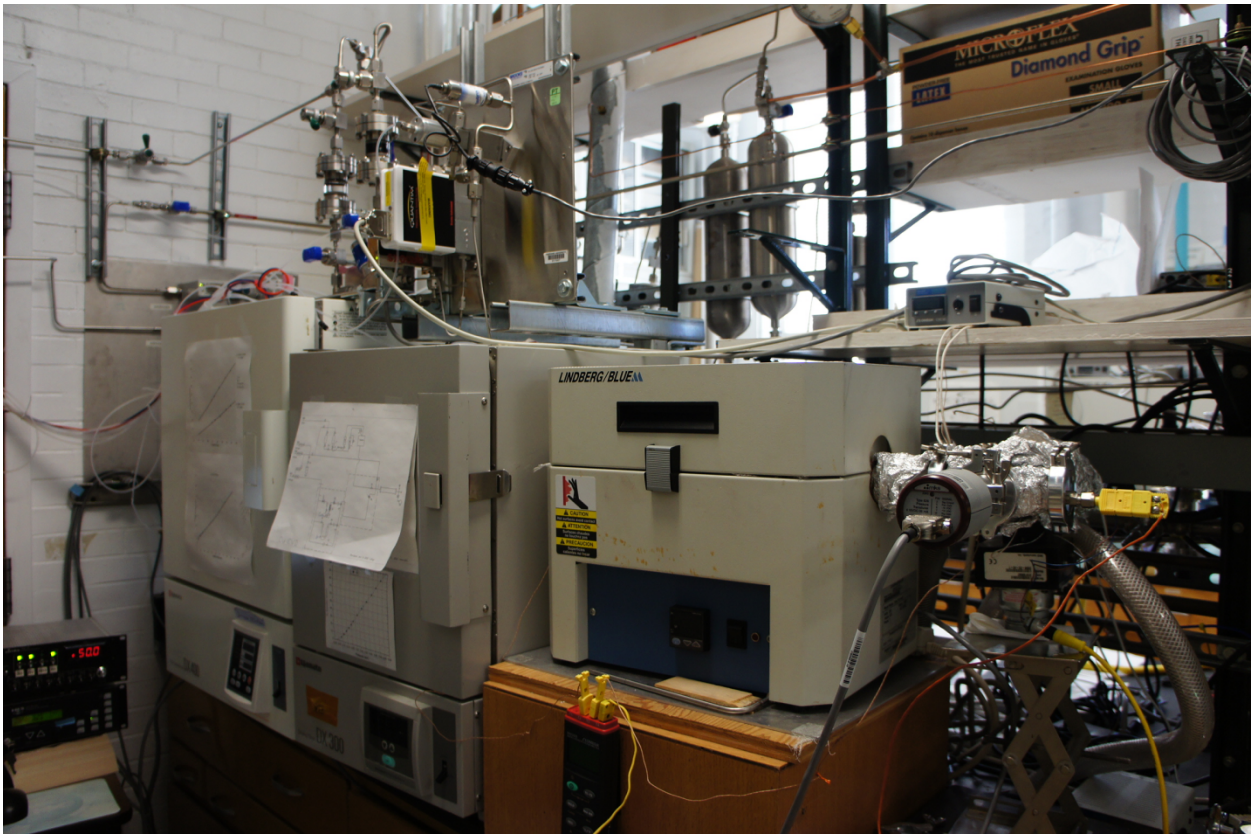

Figure A.1. CVD cobalt reactor system.

This homemade CVD reactor (Figure A.1) is used in the preparation of adhesion layers (Co_xN), barrier layer (WN) and metal layers (Co) for the metallization of advanced microelectronic devices. This reactor is customized to accommodate for both bubbler and direct-liquid-evaporation (DLE) delivery of precursors for CVD processes.

A schematic diagram of the reactor is shown below in Figure A.2.

Both cobalt amidinate (bis(N-tert-butyl-N'-ethyl-propionamidinato)cobalt(II)) and tungsten amidinate (bis(tert-butylimido)bis(dimethylamido)tungsten(VI)) precursors are kept in a bubbler reservoir and delivered by N_2 carrier gas.

The Co amidinate (bis(N,N'-diisopropylacetamidinato)cobalt(II)) precursor is dissolved in tetradecane to form a 0.38 molal solution (by dissolving 5gram precursor in 50 ml solution) and kept in a stainless steel bubbler. The liquid is pressurized by 20 psig **+** (1.4 bar +) Helium and delivered to a Brooks Instrument Quantim QMBC2 coriolis mass flow controller. Helium is chosen as the push gas due to its low solubility. The flow rate of the both pressurized precursor solution and the carrier gas can be tuned by the Brooks 0254 controller. Brooks 0254 is a four-channel power supply, readout, and set point controller. These 4 channels not only control the flow rate of N_2 carrier gas, liquid, but also measure the liquid density and pressure. The precursor solution will inject into the vaporization coils at a controlled rate.

The flow rate of the nitrogen (N_2) carrier gas and the co-reactant gases (H_2, NH_3) are precisely controlled by the mass flow controllers (MFC) #1-4.

The inlet and outlet of the Co, W amidinate precursor bubbler, the outlet of the cobalt precursor solution line, as well as the entrance and exit of the tubings are controlled by ALD valves #2-10 using the LabView program. The rest of ALD valves are currently not being used.

The deposition pressure is controlled by tuning the butterfly valve the butterfly valve to maintain a constant operating pressure. A MKS 626 Baratron® Capacitance Manometer

gauge is used to monitor the pressure. Pressure controller has stored 5 set points: A=1 torr, B =2 torr, C = 3 torr, D=10 torr, E=5 torr.

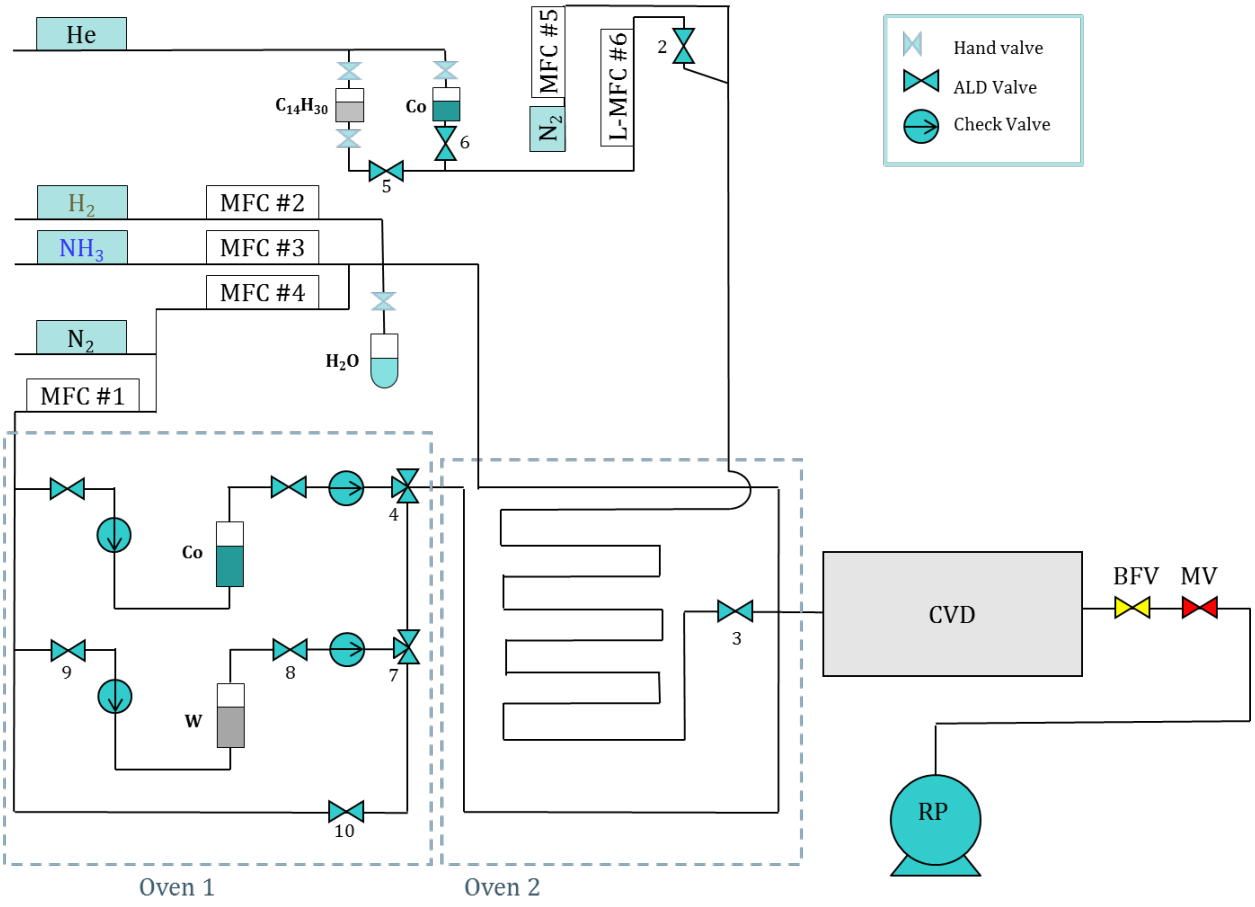

Figure A.2. The schematic diagram of the cobalt reactor

Standby Mode:

When the reactor is not in use, valves #10 and 3 are open to purge the tubings, and MFC 1, 4 and Brooks 0254 gas MFC supply 100 sccm of N_2 each (total 300 sccm N_2). If the H_2 generator is not in standby mode, it is recommended to turn on the H_2 MFC at 100 sccm to avoid H_2 pressure build up in the gas line. All other valves and MFCs should be off.

Temperature Control

Co & W bubbler is placed in oven 1, and tube coils in oven 2 allow the liquid Co precursor to vaporize. In addition to the two ovens, there are additional thermal controllers to control the temperature of the area between oven 2 and the furnace (TC 4), the area near the exit of the furnace (TC 4), the areas immediately before the pump line (TC 1 and 2), and the substrate holder (TC 3), as shown below in Figure A.3.

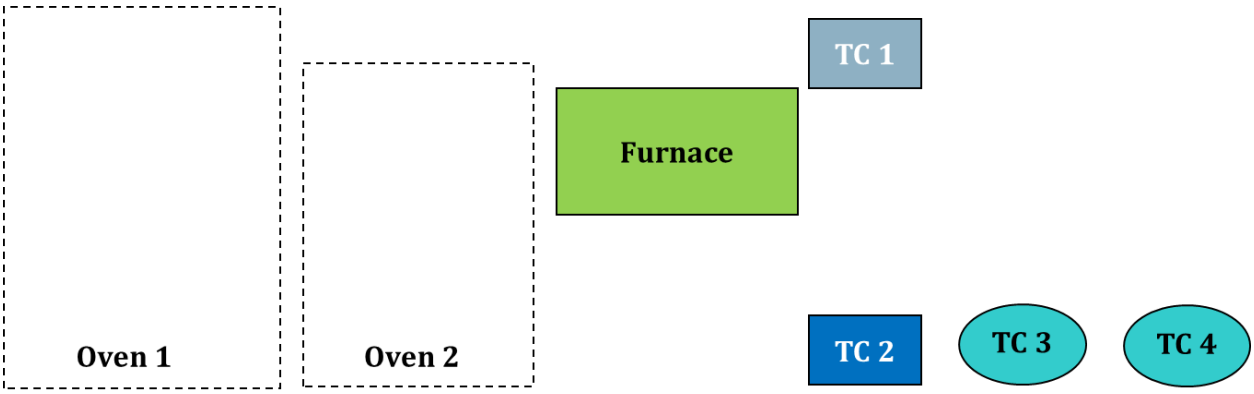

Figure A.3. Location of Temperature Controllers

Table A.1. Temperature controller settings for deposition at 200°C

TCs	Oven 1	Oven 2	Furnace	TC 1	TC 2	TC 3	TC 4
Typical setting	75~85°C	150~180°C	180°C	105°C	100°C	20 V	18 V

Oven 1: heats up Co and W precursor, typically set at 75~85°C

Oven 2: vaporizes the cobalt precursor solution, typically set at 150~180°C

TC 1: (Omega CSC 32k, Compact Benchtop Temperature Controller (TC))

heats up the line between the reactor tube outlet and the butterfly valve, typically set at 105°C

TC 2: (Omega Benchtop TC)

heats up the line between the butterfly valve and the manual valve before the connection to the pump, typically set at 100°C

Furnace: (Lindberg / Blue M Tf55030a-1 Mini-Mite 1100°C Tube Furnace)

heats up the reactor tube wall, typically 20°C lower than the substrate holder temperature. For example, for deposition at 200°C (i.e. substrate holder is heated to 200°C), the furnace temperature is set at 180°C. The furnace is set at 1000°C for RTA (rapid thermal annealing).

TC 3: (Superior Powerstat variable transformers, outlet voltage 0~140V)

supplies constant power to heat up the substrate holder, typically held at 20V for 200°C deposition temperature while the wall is heated to 180°C by the furnace.

TC 4: (Omega Benchtop TC)

heats up the reactor tube inlet and outlet, typically held at 18V, to heat the inlet and outlet to around 135°C

Experimental details of the various thin film deposition methods are outlined in the following section.

Standby Mode

1. Leave ALD valve #3, #10 on
2. Turn on MFC #1 (N_2, 100 sccm), MFC #4 (N_2, 100 sccm), Brooks gas MFC #5 controller (N_2, 100 sccm), (optional: MFC #2 (H_2, 100 sccm) if the H_2 generator is not in standby mode)

CVD-Co_xN, WN Process

Co_xN can be prepared by supplying Co precursor, hydrogen and ammonia. CoxN is an effective adhesion layer between barrier and CVD-Cu seed layer.

WN is a good barrier layer for copper interconnects.

Temperature settings (use WN as an example):

Oven 1 =75°C, Oven 2 = 85°C, Furnace =370°C, TC1, TC2 ~ 100°C, TC2=35V (Deposition temperature ~400°C), TC4 =18V

Heat up time: 1 hour

Operating Procedure

1. Turn off all the MFCs #1, 2, 4, 5
2. Turn off ALD valve #3 (The gas MFC #5 is not a shut-off valve. Therefore pressure will build up even if the MFC is off!)
3. When pressure drops to base pressure, turn off ALD valve #10
4. Turn on ALD valve #7, then #8, #9 to start W precursor flow

5. Slowly increase the N_2 carrier gas flow rate up to 20 sccm (MFC #1) to assist W precursor delivery and turn on MFC #3 to obtain 20 sccm ammonia flow
6. Set Operating Pressure = 1 Torr (set point A)
7. Typical deposition time = 5~30 minutes
8. Upon finish, set pressure controller to OPEN
9. Turn off MFC #2, #3 to terminate nitrogen and ammonia flow
10. Turn off ALD valve #9, then #8, #7 to terminate W precursor flow
11. Turn on ALD valve #10, #3 and MFC #1, #4, #5, (#2 optional) to start purging
12. Turn off all ovens and heaters, allow up to one hour to cool down

DLE-CVD Co & Co_xN Process (Figure A.4.)

Metallic cobalt can be prepared by supplying Co precursor solution, hydrogen and ammonia.

Temperature settings: (as listed in Table A.1)

Heat up time: 1 hour

Operating Procedure

1. Check the Helium gas pressure to be above 20 psi before heating up
2. Heating up the reactor system
3. Turn off all the MFCs #1, 4
4. **For DLE-CVD Co**, Turn on MFCs #2 (H_2, 100 sccm), MFCs #3 (NH_3, 100 sccm) as the co-reactants, MFCs #5 (N_2, 100 sccm) for assisting the liquid delivery;

For DLE-CVD CoN, Turn on MFCs #3 (NH_3, 200 sccm) as the co-reactants, MFCs #5 (N_2, 100 sccm) for assisting the liquid delivery.

5. Set Operating Pressure = 10 Torr (set point D)
6. Make the liquid MFC #6 ready at set-point (typically 5g/hr)
7. Turn on the manual valve below the cobalt precursor solution bubbler
8. Turn on ALD valve #6, #2
9. "Enter" the liquid MFC #6 delivery rate (5 g/hr) to start the liquid flow
10. Watch the real-time liquid MFC delivery rate during deposition !!! (sometimes it requires to tune the Helium pressure to enable the real-time flow rate within a small variation from the setting point)
11. Typical deposition time = 10-30 minutes (deposition rate ~ 1nm/min)
12. Upon finish, turn off the Liquid MFC #6, then the manual valve, ALD valve #6, #2
13. Maintain at the deposition temperature and pressure for 30 mins (especially when the vaporization temperature/ oven 2 = 150°C instead of 180°C to achieve complete vaporization of the precursor solution)
14. Set pressure controller to OPEN
15. Turn off MFC #2, #3 to terminate hydrogen and ammonia flow
16. Turn on ALD valve #10, #3 and MFC #1, #4, #5, (#2 optional) to start purging
17. Turn off all ovens and heaters, allow up to one hour to cool down

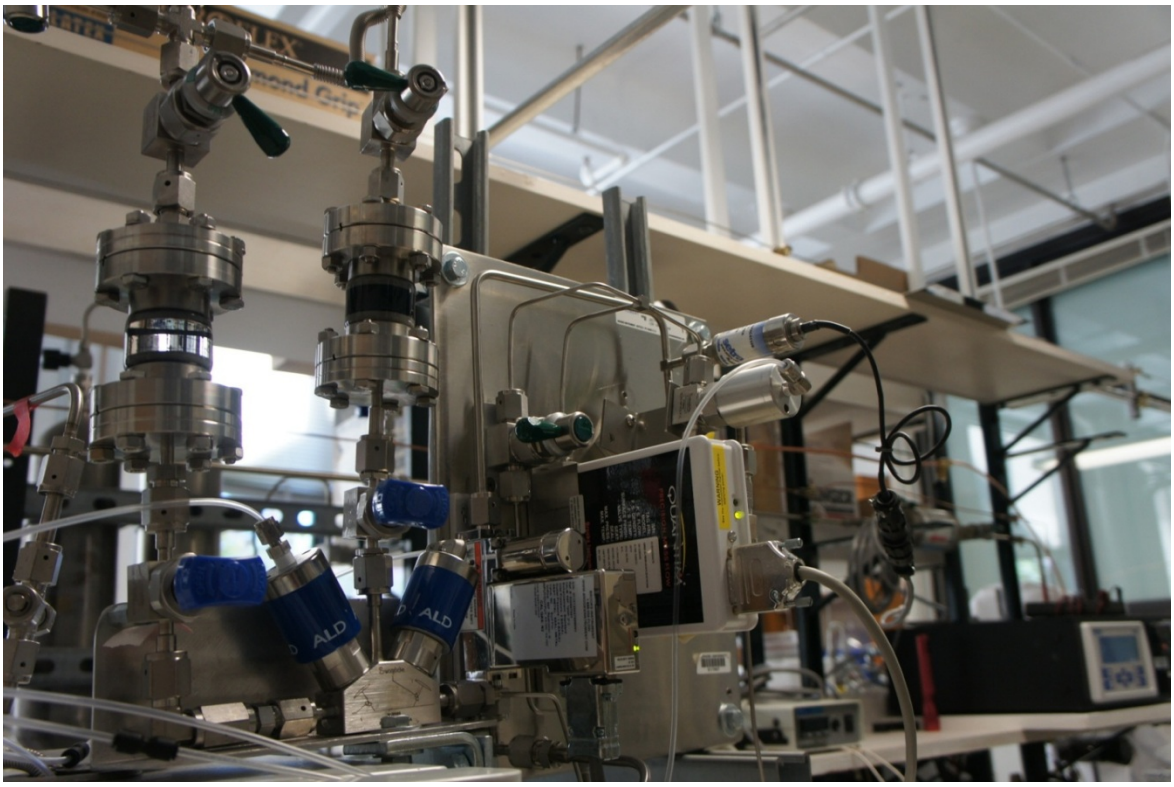

Figure A.4. The DLE-CVD Co Precursor Solution Delivery System

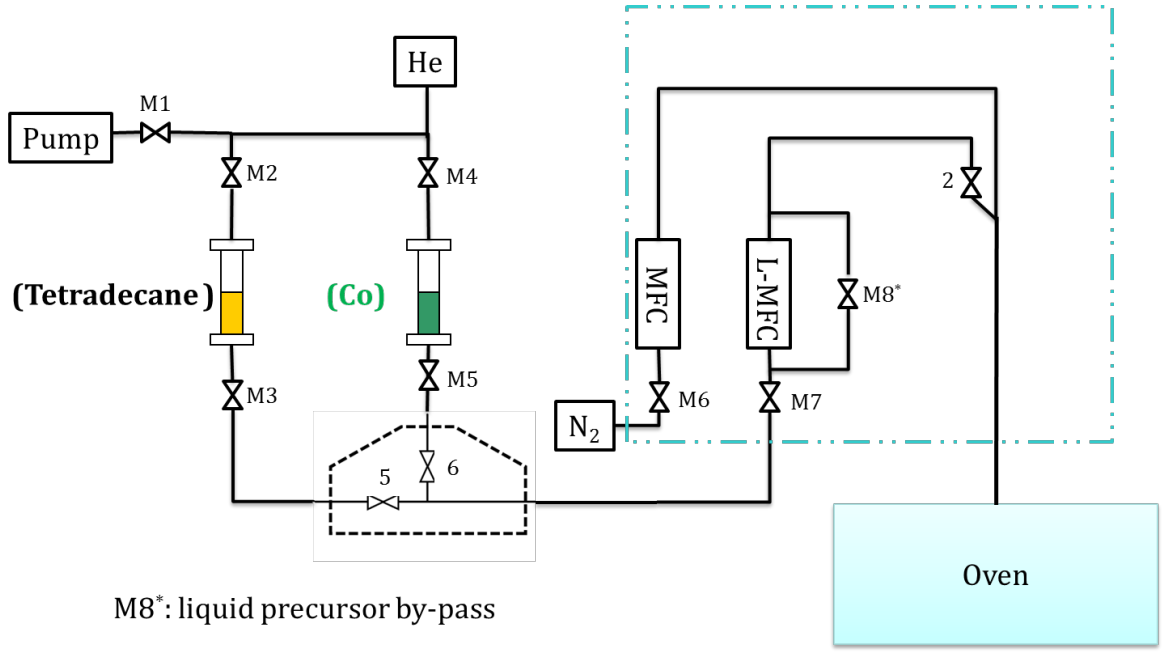

Figure A.5. Schematic Diagram of the DLE-CVD Co Precursor Solution Delivery System

Case I. Load the Bubbler for the first time: (Figure A.5.)

1. ALD valve #5, #6 closed to prevent air exposure of the liquid delivery lines
2. Load the bubbler (with M2, M3, M4, M5 closed) inside the glove box
3. Install the bubbler
4. Pump all the lines upstream and downstream of the bubbler (Open M1, 5, M6, 2 to pump away the air) before operations

Case II. Change the empty Co bubbler

1. Turn on M5, M4, M1 to pump down the pressure of Co bubbler,
2. Make sure M7, M8 and ALD valve #2 is OFF
3. Turn off M5, M4, M1
4. Pressurize the solvent bubbler with high-pressure helium with M2 ON, M3, ALD valve #5 OFF (i.e. the two bubblers are disconnected)
5. Turn off M2, open M3, ALD valve #5, then ALD valve #6 and M5
6. The solvent will enter Co bubbler to dilute the remaining cobalt precursor solution
7. Deplete the diluted precursor solution into heated reactor
8. Disconnect the bubbler
9. Load the bubbler inside the glove box